

Mean-field description of ground-state properties of drip-line nuclei: Pairing and continuum effects

J. Dobaczewski,^{1,2} W. Nazarewicz,¹⁻⁴ and T.R. Werner^{1,5}

¹*Institute of Theoretical Physics, Warsaw University, ul. Hoża 69, 00-681 Warsaw, Poland*

²*Institute for Nuclear Theory, University of Washington,
Seattle, Washington 98195, U.S.A.*

³*Department of Physics & Astronomy, University of Tennessee,
Knoxville, Tennessee 37996, U.S.A.*

⁴*Physics Division, Oak Ridge National Laboratory,
P.O. Box 2008, Oak Ridge, Tennessee 37831, U.S.A.*

⁵*Joint Institute for Heavy-Ion Research, Oak Ridge, Tennessee 37831, USA*

and

J.F. Berger,⁶ C.R. Chinn,⁷ and J. Dechargé⁶

⁶*Centre d'Etudes de Bruyères-le-Châtel, B.P. No. 12, 91680 Bruyères-le-Châtel, France*

⁷*Department of Physics & Astronomy, Vanderbilt University, Nashville, Tennessee 37235, U.S.A.*

Abstract

Ground-state properties of exotic even-even nuclei with extreme neutron-to-proton ratios are described in the framework of the self-consistent mean-field theory with pairing formulated in coordinate space. This theory properly accounts for the influence of the particle continuum, which is particularly important for weakly bound systems. The pairing properties of nuclei far from stability are studied with several interactions emphasizing different aspects, such as the range and density dependence of the effective interaction. Measurable consequences of spatially extended pairing fields are presented, and the sensitivity of the theoretical predictions to model details is discussed.

PACS numbers: 21.10.-k, 21.30.+y, 21.60.Jz

I. INTRODUCTION

One of the most exciting challenges in today's nuclear structure is the physics of exotic nuclei far from the line of β -stability. What makes this subject particularly interesting (and difficult) is the unique combination of weak binding and the proximity of the particle continuum, both implying the large diffuseness of the nuclear surface and extreme spatial dimensions characterizing the outermost nucleons [1–4].

For the weakly bound nuclei the decay channels have to be considered explicitly. Due to the virtual scattering of nucleons from bound orbitals to unbound scattering states, the traditional shell-model technology becomes inappropriate. The proper tool is the continuum shell model [5,6] which correctly accounts for the coupling to resonances; the single-particle basis of the continuum shell model consists of both bound and unbound states. The explicit coupling between bound states and the continuum and the presence of low-lying low- ℓ scattering states invites strong interplay between various aspects of nuclear structure and reaction theory.

Particularly exciting are new phenomena on the neutron-rich side. Because neutrons do not carry an electric charge, the neutron drip line is located very far from the valley of β -stability. Consequently, the neutron drip-line systems (i.e., those close to the neutron drip line) are characterized by unusually large N/Z ratios. The outer zone of these nuclei are expected to constitute essentially a new form of a many-body system: low-density neutron matter (neutron halos and skins).

Except for the lightest nuclei, the bounds of neutron stability are not known experimentally. Theoretically, because of their sensitivity to various theoretical details (e.g., approximations used, parameter values, interactions) predicted drip lines are strongly model-dependent. The placement of the one-neutron drip line, defined by the condition $S_n(Z, N) = B_n(Z, N) - B_n(Z, N - 1) = 0$, is solely determined by the binding energy difference between two neighboring isotopes. Analogously, the vanishing two-neutron separation energy, $S_{2n}(Z, N) = B_n(Z, N) - B_n(Z, N - 2)$, defines the position of the two-neutron drip line. Since experimental masses (binding energies) near the neutron drip lines are unknown, in order to extrapolate far from stability, the large-scale mass calculations are usually used (see, e.g., [7–11]). However, since their techniques and parameters are optimized to reproduce known atomic masses, it is by no means obvious whether the particle number dependence obtained from global calculations at extreme values of N/Z is correct. Apart from strong theoretical and experimental interest in nuclear physics aspects of exotic nuclei, calculations for nuclei far from stability have strong astrophysical implications, especially in the context of the r-process mechanism [12,13].

In previous work [14] several aspects of nuclear structure at the limits of extreme isospin were discussed by means of the macroscopic-microscopic approach. In the present study, ground-state properties of drip-line systems and the sensitivity of predictions to effective forces are investigated by means of the self-consistent Hartree-Fock-Bogoliubov (HFB) approach.

The paper is organized as follows. Section II discusses the effective interactions employed in this study. Since pairing correlations are crucial for the behavior of drip-line systems, particular attention is paid to the particle-particle (p-p, pairing) component of the interaction. After a short review of general properties of effective pairing interactions, with emphasis on

the density dependence, the pairing forces investigated in our work, namely contact forces (delta interaction, density-dependent delta interaction, and Skyrme interaction) and the finite-range Gogny force, are described.

The basic ingredients of the HFB formalism in the coordinate representation (single-quasiparticle orbitals, time-reversal symmetry, canonical states, and various densities) are defined in Sec. III. In contrast to the single-quasiparticle wave functions which often contain a scattering (outgoing) component, canonical states (Sec. IIIB) are always localized, even if they have positive average energy. The interpretation of particle and (especially) pair densities in terms of single-particle and correlation probabilities is given in Sec. IIIC. This interpretation is essential when relating the calculated HFB densities and fields to various experimental observables.

The structure of the HFB equations is analyzed in Sec. IV. Here, various functions entering the equations of motion (i.e., mass parameters and mean field potentials) are introduced for both p-h and p-p channels (Secs. IVA and IVB).

The advantage of using the coordinate-space HFB formalism for weakly bound systems is that in this method the particle continuum is treated properly. This important point is discussed in detail in Sec. V. In particular, the difference between the single-particle Hartree-Fock (HF) spectra and canonical HFB spectra (Sec. VB), the asymptotic properties of the HFB states (Sec. VE) and densities (Sec. VF), and the effect of the pairing coupling to positive-energy states (Sec. VG) are carefully explained.

The robust predictions of the formalism for various experimental observables (pairing gaps and pair transfer amplitudes, masses and separation energies, radii, shell gaps, and shell structure) are reviewed in Sec. VI, where experimental fingerprints of the surface-peaked pairing fields and the quenching of shell effects far from stability are also given. Section VII contains the main conclusions of the paper. The technical details (i.e., the form of a mean-field Gogny Hamiltonian and the discussion of the energy cut-off in the Skyrme model) are collected in the Appendices.

II. EFFECTIVE INTERACTIONS IN THE P-P CHANNEL

The uniqueness of drip-line nuclei for studies of effective interactions is due to the very special role played by the pairing force. This is seen from approximate HFB relations between the Fermi level, λ , pairing gap, Δ , and the particle separation energy, S [15]:

$$S \approx -\lambda - \Delta. \quad (2.1)$$

Since for drip-line nuclei S is very small, $\lambda + \Delta \approx 0$. Consequently, the single-particle field characterized by λ (determined by the p-h component of the effective interaction) and the pairing field Δ (determined by the p-p part of the effective interaction) are equally important. In other words, contrary to the situation encountered close to the line of beta stability, the pairing component can no longer be treated as a *residual* interaction; i.e., a small perturbation important only in the neighborhood of the Fermi surface.

Surprisingly, rather little is known about the basic properties of the p-p force. In most calculations, the pairing Hamiltonian has been approximated by the state-independent seniority pairing force, or schematic multipole pairing interaction [16]. Such oversimplified

forces, usually treated by means of the BCS approximation, perform remarkably well when applied to nuclei in the neighborhood of the stability valley (where, as pointed out above, pairing can be considered as a small correction). As a result, considerable effort was devoted in the past to optimizing the p-h part of the interaction, while leaving the p-p component aside.

Up to now, the microscopic theory of the pairing interaction has only seldom been applied in realistic calculations for finite nuclei (see Ref. [17] for a recent example). A “first-principle” derivation of pairing interaction from the bare NN force using the renormalization procedure (G -matrix technique), still encounters many problems such as, e.g., treatment of core polarization [18,19]. Hence, phenomenological pairing interactions are usually introduced. Two important open questions asked in this context are: (i) the role of finite range, and (ii) the importance of density dependence. Since the realistic effective interactions are believed to have a finite range, the first question seems purely academic. However, the remarkable success of zero-range Skyrme forces suggests that, in many cases, the finite-range effect can be mocked up by an explicit velocity dependence. To what extent this is true for the pairing channel remains to be seen. One obvious advantage of using finite-range forces is the automatic cut-off of high-momentum components; for the zero-range forces this is solved by restricting the pair scattering to a limited energy range and by an appropriate renormalization of the pairing coupling constant (see Appendix B).

The answer to the question on the density dependence is much less clear. Early calculations [20,21] for nuclear matter predicted a very weak 1S_0 pairing at the saturation point ($k_F=1.35\text{ fm}^{-1}$). Consequently, it was concluded that strong pairing correlations in finite nuclei had to be due to interactions at the nuclear surface. This led to the surface delta interaction (SDI) [22], a highly successful residual interaction between valence nucleons. Of course, the SDI is an extreme example of surface interaction. More realistic density-dependent pairing forces are variants of the density-dependent delta interaction (DDDI) introduced in the Migdal theory of finite Fermi systems [23].

Since the effective interactions commonly used in the HF calculations are bound to be density dependent in order to reproduce the compressibility of the infinite nuclear matter [24] (an explicit density dependence is also said to account for three- and higher-body components of the interaction), it seems natural to introduce the density dependence in the p-p channel as well [25].

Interestingly, the presence (absence) of the density dependence in the pairing channel has consequences for the spatial properties of pairing densities and fields. As early recognized [26], the density-independent p-p force gives rise to a pairing field that has a volume character. For instance, the commonly used contact delta interaction,

$$V^\delta(\mathbf{r}, \mathbf{r}') = V_0 \delta(\mathbf{r} - \mathbf{r}'), \quad (2.2)$$

leads to volume pairing. By adding a density-dependent component, the pairing field becomes surface-peaked. A simple modification of force (2.2) is the DDDI [25,27,28]

$$V^{\delta\rho}(\mathbf{r}, \mathbf{r}') = V_0 \delta(\mathbf{r} - \mathbf{r}') \{1 - [\rho(\mathbf{r})/\rho_c]^\gamma\}, \quad (2.3)$$

where $\rho(\mathbf{r})$ is the isoscalar nucleonic density, and V_0, ρ_c and γ are constants. If ρ_c is chosen such that it is close to the saturation density, $\rho_c \approx \rho(\mathbf{r} = 0)$, both the resulting pair density and the pairing potential $\Delta(\mathbf{r})$ (see Secs. III C and IV A) are small in the nuclear interior.

By varying the magnitude of the density-dependent term, the transition from volume pairing [$\rho_c \gg \rho(0)$] to surface pairing can be probed.

What are the experimental arguments in favor of surface pairing? Probably the strongest evidence is the odd-even staggering in differential radii, explained in terms of the direct coupling between the proton density and the neutron pairing tensor [29–32]. Other experimental observables which strongly reflect the spatial character of pairing are the particle widths and energies of deep-hole states [33,34], strongly influenced by the pairing-induced coupling to the particle continuum, and the pair transfer form factors, directly reflecting the shape of the pair density. Because of strong surface effects, the properties of weakly bound nuclei are sensitive to the density dependence of pairing. In particular, the same type of force is used to describe the spatial extension of loosely bound light systems [35–38]. (The measurable fingerprints of surface pairing in neutron-rich systems are further discussed in Sec. VI.) In this context, it is also worth mentioning that the self-consistent model with the DDDI has recently been used to describe the nuclear charge radii [39] and the moments of inertia of superdeformed nuclei [40]. In the latter case, the inclusion of a density dependence in the p-p channel turned out to be crucial for the reproduction of experimental data around ^{194}Hg .

In a series of papers [41–43] the Quasiparticle Lagrangian method (QLM) [44] based on the single-particle Green function approach in the coordinate representation [45] has been applied to the description of nuclear superfluidity. The resulting pairing interaction, based on the Landau-Migdal ansatz [23], has zero-range and contains two-body and three-body components, thus leading to a density-dependent contact force similar to that of Eq. (2.3). (Note that in the approximations of Ref. [41], the *neutron* pairing interaction is proportional to the *proton* density and vice versa.) However, in practical QLM calculations [41–43], a pure density-independent delta force was used.

A better understanding of the density dependence of the nuclear pairing interaction is important for theories of superfluidity in neutron stars. As pointed out in Ref. [46], it is impossible at present to deduce the magnitude of the pairing gaps in neutron stars with sufficient accuracy. Indeed, calculations of 1S_0 pairing gaps in pure neutron matter, or symmetric nuclear matter, based on bare NN interactions [47] suggest a strong dependence on the force used; in general, the singlet- S pairing is very small at the saturation point. On the other hand, nuclear matter calculations with an effective finite-range interaction, namely the Gogny force [48], yield rather large values of the pairing gap at saturation ($\Delta \simeq 0.7 \text{ MeV}$). (For relativistic HFB calculations for symmetric nuclear matter, see Ref. [18]. The pairing properties of the Skyrme force in nuclear matter were investigated in Ref. [49]. See also Ref. [50] for schematic calculations of pairing properties in nuclear matter based on the Green function method with a contact interaction, and Ref. [51] for a semi-classical description of neutron superfluidity in neutron stars using the Gogny force.)

In this study, several self-consistent models based upon the HFB approaches are used. The effective interactions employed, and other model parameters, are briefly discussed below.

The spherical HFB-Skyrme calculations have been carried out in spatial coordinates following the method introduced in Ref. [52] and discussed in detail in Secs. III–V. Several effective Skyrme interactions are investigated. These are: (i) the Skyrme parametrization SkP introduced in Ref. [52] (SkP has exactly the same form in the particle-hole (p-h) and pairing channels); (ii) Skyrme interaction SkP $^\delta$ of Ref. [53] (in the p-h channel, this force is the SkP Skyrme parametrization, while its pairing component is given by delta interaction,

Eq. (2.2); (iii) the Skyrme interaction $\text{SkP}^{\delta\rho}$ of Ref. [53] (in the p-h channel, this force is the SkP Skyrme parametrization, while its pairing component is given by Eq. (2.3); (iv) the force SIII^δ (in the p-h channel, this is the SIII Skyrme parametrization [54]; its pairing component is given by the delta force of Ref. [53]); (v) the force SkM^δ (in the p-h channel, this is the SkM* Skyrme parametrization [55], and its pairing part is given by the delta force with the parameters of Ref. [53]).

Apart from other parameters, the above Skyrme forces differ in their values of the effective mass for symmetric nuclear matter, m^*/m . Namely, m^*/m is 0.76, 0.79, and 1 for SIII, SkM*, and SkP, respectively. All HFB-Skyrme results have been obtained using the pairing phase space as determined in Ref. [52] (see also discussion in Appendix B).

A set of spherical HFB calculations has also been performed using the finite-range density-dependent Gogny interaction D1S of Ref. [56]. In this effective interaction [57] the central part consists of four terms parametrized with finite-range Gaussians (see Appendix A). Spin-orbit and density-dependent terms of zero range are also included as in the Skyrme parametrizations. The pairing field is calculated from the D1S force, i.e., the same interaction is used for a microscopic description for both the mean field and the pairing channels. However, by a specific choice of the exchange contribution, the pairing component of the D1S is density-independent. It is also interesting to note that the pairing component of the D1S is repulsive at short distances and attractive at long ranges [18,58]. For the D1S force, the effective mass for infinite nuclear matter is $m^*/m=0.70$.

The parameters of the D1S interaction were chosen to reproduce certain global properties of a set of spherical nuclei and of nuclear matter [59]. The HFB+Gogny results presented here were obtained by expanding the HFB wave functions in a harmonic oscillator basis containing up to 19 shells.

III. INDEPENDENT-QUASIPARTICLE STATES

The HFB approach is a variational method which uses independent-quasiparticle states as trial wave functions. These states are particularly convenient when used in a variational theory, because, due to the Wick theorem [60], one can easily calculate for them the average values of an arbitrary many-body Hamiltonian. Even if the exact eigenstates of such a Hamiltonian can be rather remote from any one of the independent-quasiparticle states, one can argue [61] that one may obtain in this way fair estimates of at least one-body observables.

An independent-quasiparticle state is defined as a vacuum of quasiparticle operators which are linear combinations of particle creation and annihilation operators. This linear combination is called the Bogoliubov transformation [62–64]. According to the Thouless theorem [65], every independent-quasiparticle state $|\Psi\rangle$, which is not orthogonal to the vacuum state $|0\rangle$, i.e., $\langle 0|\Psi\rangle \neq 0$, can be presented in the form

$$|\Psi\rangle = \exp \left\{ -\frac{1}{2} \sum_{\mu\nu} Z_{\mu\nu}^+ a_\mu^+ a_\nu^+ \right\} |0\rangle, \quad (3.1)$$

where the Thouless matrix Z is antisymmetric, $Z^+ = -Z^*$, and in general complex. The phase of state (3.1) is fixed by the condition $\langle 0|\Psi\rangle=1$; the norm is given by $\langle \Psi|\Psi\rangle=\det(1 + Z^+Z)^{1/2}$. In the following, state $|\Psi\rangle$ will represent the $I^\pi=0^+$ ground state of the even-even system.

We refer to standard textbooks [24] for a discussion of the properties of the Bogoliubov transformation. Here we start our discussion from the trial wave function (3.1) which is parametrized by the matrix elements of Z . This form of the independent-quasiparticle state is very convenient in variational applications because variations with respect to all matrix elements $Z_{\mu\nu} = -Z_{\nu\mu}$ are independent of one another.

Instead of using the matrix representation corresponding to a set of single-particle creation operators a_μ^+ numbered by the discrete index μ , one may use the spatial coordinate representation. This is particularly useful when discussing spatial properties of the variational wave functions and the coupling to the particle continuum. Therefore, in the following, we shall consider the operators creating a particle in the space point \mathbf{r} and having the projection of spin $\sigma = \pm\frac{1}{2}$,

$$a_{\mathbf{r}\sigma}^+ = \sum_{\mu} \psi_{\mu}^*(\mathbf{r}\sigma) a_{\mu}^+, \quad (3.2)$$

where $\psi_{\mu}(\mathbf{r}\sigma)$ is the wave function of the μ -th single-particle state. To simplify the following expressions, we consider only one type of particle. A generalization to systems described by a product of neutron and proton wave functions is straightforward, while that involving the mixing in the isospin degree of freedom is discussed in Ref. [66].

The inverse relation with respect to (3.2) is given by

$$a_{\mu}^+ = \int d^3\mathbf{r} \sum_{\sigma} \psi_{\mu}(\mathbf{r}\sigma) a_{\mathbf{r}\sigma}^+. \quad (3.3)$$

Equations (3.2) and (3.3) assume that the wave functions $\psi_{\mu}(\mathbf{r}\sigma)$ form an orthonormal and complete set. In practical calculations, the basis has to be truncated and the completeness is realized only approximately. The choice of the single-particle wave functions used (size of the set and, in particular, the asymptotic behavior) is of crucial importance to the phenomena discussed in this study.

In coordinate space, the Thouless state (3.1) has the form

$$|\Psi\rangle = \exp \left\{ -\frac{1}{2} \int d^3\mathbf{r} d^3\mathbf{r}' \sum_{\sigma\sigma'} Z^+(\mathbf{r}\sigma, \mathbf{r}'\sigma') a_{\mathbf{r}\sigma}^+ a_{\mathbf{r}'\sigma'}^+ \right\} |0\rangle, \quad (3.4)$$

and is defined by the antisymmetric complex function, $Z^+(\mathbf{r}\sigma, \mathbf{r}'\sigma') = -Z^*(\mathbf{r}\sigma, \mathbf{r}'\sigma')$, of space-spin coordinates. Already, at this point, we see that any variational method employing an attractive effective interaction for a *bound finite system* must lead to functions which are localized in space,

$$\lim_{|\mathbf{r}| \rightarrow \infty} Z(\mathbf{r}\sigma, \mathbf{r}'\sigma') = 0, \quad \text{for any } \mathbf{r}', \sigma', \text{ and } \sigma. \quad (3.5)$$

Recall that in the coordinate space, values of the function $Z(\mathbf{r}\sigma, \mathbf{r}'\sigma')$ at different space-spin points are the variational parameters, and that any arbitrarily small value of this function at large distance, $|\mathbf{r}| \rightarrow \infty$, would create at this point a non-zero probability density. Whether this would be energetically favorable depends upon the number of particles in the system and on the interaction used in the variational method. Apart from exotic phenomena such as halos, and apart from infinite matter such as in the neutron-star crust, we assume that the

attractiveness of the interaction always favors compact, localized probability densities, and hence we require the localization condition (3.5) for the variational parameters $Z(\mathbf{r}\sigma, \mathbf{r}'\sigma')$.

An expansion of the variational function $Z(\mathbf{r}\sigma, \mathbf{r}'\sigma')$ in terms of the single-particle wave functions is a straightforward consequence of transformations (3.2) and (3.3),

$$Z(\mathbf{r}\sigma, \mathbf{r}'\sigma') = \sum_{\mu\nu} \psi_\mu^*(\mathbf{r}\sigma) Z_{\mu\nu} \psi_\nu^*(\mathbf{r}'\sigma'). \quad (3.6)$$

The localization condition, Eq. (3.5), can, therefore, be guaranteed in the most economic way by requiring that *all* single-particle wave functions $\psi_\mu(\mathbf{r}\sigma)$ vanish at large distances. Of course, this is only a matter of convenience and manageability, because any localized function can be expanded in any complete basis. It is, however, obvious that such an expansion converges very slowly if the basis has inappropriate asymptotic properties. For example, one can expect that a plane-wave expansion of $Z(\mathbf{r}\sigma, \mathbf{r}'\sigma')$ would require an infinite number of basis states $\psi_\mu(\mathbf{r}\sigma)$, and in practice, any reduction to a finite basis would lead to serious errors. A discussion pertaining to asymptotic properties of functions in spatial coordinates, and the choice of an appropriate single-particle basis, will be a pivotal point in our study.

A. Time-reversal

The present study is entirely restricted to an analysis of ground-state phenomena, and therefore, we use only time-even variational independent-quasiparticle wave functions. The time-reversal operator can be represented as a product of the spin-flip operator and the complex conjugation; i.e., $\hat{T} = -i\hat{\sigma}_y\hat{K}$ [67]. The explicit time-reversed creation operators then have the form

$$\hat{T}^+ a_{\mathbf{r}\sigma}^+ \hat{T} = -2\sigma a_{\mathbf{r},-\sigma}^+, \quad (3.7a)$$

$$\hat{T}^+ a_\mu^+ \hat{T} = \int d^3\mathbf{r} \sum_\sigma [2\sigma \psi_\mu^*(\mathbf{r}, -\sigma)] a_{\mathbf{r}\sigma}^+. \quad (3.7b)$$

We now suppose that the set of basis states represented by the creation operators a_μ^+ is closed with respect to time reversal, and that the state $\hat{T}^+ a_\mu^+ \hat{T}$ is actually proportional (up to a phase factor $s_{\bar{\mu}} = -s_\mu$, $|s_\mu| = 1$) to another basis state denoted by a bar over the Greek symbol, i.e.,

$$\hat{T}^+ a_\mu^+ \hat{T} = s_{\bar{\mu}} a_{\bar{\mu}}^+, \quad (3.8a)$$

$$s_{\bar{\mu}} \psi_{\bar{\mu}}(\mathbf{r}\sigma) = 2\sigma \psi_\mu^*(\mathbf{r}, -\sigma). \quad (3.8b)$$

In this way, the single-particle basis is assumed to be composed of pairs of time-reversed states denoted by indices μ and $\bar{\mu}$. In what follows, we use the convention that $\bar{\bar{\mu}} \equiv \mu$, and that the sums over either μ or $\bar{\mu}$ are always performed over *all* basis states. The phase factors s_μ depend on relative phases chosen for the μ -th and $\bar{\mu}$ -th states of the basis; it is convenient to keep them unspecified in all theoretical formulae and to make a definite suitable choice of the phase convention only in a specific final application.

B. Canonical basis

A requirement of the time-reversal symmetry of the quasiparticle vacuum (3.1) or (3.4), $\hat{T}|\Psi\rangle=|\Psi\rangle$, leads to the following conditions:

$$Z_{\mu\nu} = s_\mu^* s_\nu^* Z_{\bar{\mu}\bar{\nu}}^*, \quad (3.9a)$$

$$Z(\mathbf{r}\sigma, \mathbf{r}'\sigma') = 4\sigma\sigma' Z^*(\mathbf{r}, -\sigma, \mathbf{r}', -\sigma'). \quad (3.9b)$$

These properties allow the introduction of more suitable forms of $Z_{\mu\nu}$ and $Z(\mathbf{r}\sigma, \mathbf{r}'\sigma')$; namely,

$$\tilde{Z}_{\mu\nu} := s_\mu Z_{\bar{\mu}\nu}, \quad (3.10a)$$

$$\tilde{Z}(\mathbf{r}\sigma, \mathbf{r}'\sigma') := 2\sigma Z(\mathbf{r}, -\sigma, \mathbf{r}'\sigma'). \quad (3.10b)$$

The matrix $\tilde{Z}_{\mu\nu}$ and the function $\tilde{Z}(\mathbf{r}\sigma, \mathbf{r}'\sigma')$ are both time-even and hermitian,

$$\tilde{Z}_{\mu\nu}^* = \tilde{Z}_{\nu\mu}, \quad (3.11a)$$

$$\tilde{Z}^*(\mathbf{r}\sigma, \mathbf{r}'\sigma') = \tilde{Z}(\mathbf{r}'\sigma', \mathbf{r}\sigma), \quad (3.11b)$$

and therefore they can be considered as usual operators in the corresponding Hilbert spaces. In particular, the function $\tilde{Z}^*(\mathbf{r}\sigma, \mathbf{r}'\sigma')$ can be diagonalized by solving the following integral eigenequation:

$$\int d^3\mathbf{r}' \sum_{\sigma'} \tilde{Z}(\mathbf{r}\sigma, \mathbf{r}'\sigma') \check{\psi}_\mu(\mathbf{r}'\sigma') = z_\mu \check{\psi}_\mu(\mathbf{r}\sigma), \quad (3.12)$$

where z_μ are real eigenvalues, $z_\mu = z_{\bar{\mu}}$. The eigenfunctions $\check{\psi}_\mu(\mathbf{r}\sigma)$ form the single-particle basis, usually referred to as the *canonical basis*. Canonical states, together with the eigenvalues z_μ , completely define the quasiparticle vacuum $|\Psi\rangle$. (Here and in the following we use the checked symbols, e.g., $\check{\psi}_\mu$ and \check{a}_μ^+ , to denote objects pertaining to the canonical basis.)

Two important remarks concerning the canonical basis are now in order. First, the localization condition (3.5) directly results in the fact that *all* canonical-basis single-particle wave functions $\check{\psi}_\mu(\mathbf{r}\sigma)$ are localized in space; i.e., vanish at large distances, $|\mathbf{r}| \rightarrow \infty$. Therefore, as discussed previously, a choice of the localized wave functions for the basis states $\psi_\mu(\mathbf{r}\sigma)$ may allow for a rapid convergence in the expansion

$$\check{\psi}_\mu(\mathbf{r}\sigma) = \sum_\nu D_{\nu\mu} \psi_\nu(\mathbf{r}\sigma), \quad (3.13a)$$

$$\check{a}_\mu^+ = \sum_\nu D_{\nu\mu} a_\nu^+. \quad (3.13b)$$

Second, since $\tilde{Z}(\mathbf{r}\sigma, \mathbf{r}'\sigma')$ and $\tilde{Z}_{\mu\nu}$ are related by [cf. Eq. (3.6)]

$$\tilde{Z}(\mathbf{r}\sigma, \mathbf{r}'\sigma') = \sum_{\mu\nu} \psi_\mu(\mathbf{r}\sigma) \tilde{Z}_{\mu\nu} \psi_\nu^*(\mathbf{r}'\sigma'), \quad (3.14)$$

a diagonalization of $\tilde{Z}(\mathbf{r}\sigma, \mathbf{r}'\sigma')$, Eq. (3.12), is equivalent to a diagonalization of $\tilde{Z}_{\mu\nu}$,

$$\sum_{\nu} \tilde{Z}_{\mu\nu} D_{\nu\tau} = z_{\tau} D_{\mu\tau}. \quad (3.15)$$

Therefore, in the canonical basis, the Thouless state (3.1) acquires the well-known separable BCS-like form

$$\begin{aligned} |\Psi\rangle &= \exp \left\{ \frac{1}{2} \sum_{\mu\nu} \tilde{Z}_{\mu\nu} s_{\mu} a_{\bar{\mu}}^{+} a_{\nu}^{+} \right\} |0\rangle \\ &= \exp \left\{ \sum_{\nu>0} z_{\nu} s_{\nu} \check{a}_{\bar{\nu}}^{+} \check{a}_{\nu}^{+} \right\} |0\rangle \\ &= \prod_{\nu>0} \left(1 + z_{\nu} s_{\nu} \check{a}_{\bar{\nu}}^{+} \check{a}_{\nu}^{+} \right) |0\rangle, \end{aligned} \quad (3.16)$$

where the symbol $\nu > 0$ denotes the sum over one-half of the basis states with only one state (either one) of each time-reversed pair $(\nu, \bar{\nu})$ included, and \check{a}_{ν}^{+} is the creation operator in the canonical basis.

C. Density matrices and the correlation probability

According to the Wick theorem [60,24] for the independent-quasiparticle state, Eqs. (3.1) or (3.4), an average value of any operator can be expressed through average values of bifermion operators,

$$\rho(\mathbf{r}\sigma, \mathbf{r}'\sigma') = \langle \Psi | a_{\mathbf{r}'\sigma'}^{+} a_{\mathbf{r}\sigma} | \Psi \rangle, \quad (3.17a)$$

$$\tilde{\rho}(\mathbf{r}\sigma, \mathbf{r}'\sigma') = -2\sigma' \langle \Psi | a_{\mathbf{r}', -\sigma'} a_{\mathbf{r}\sigma} | \Psi \rangle. \quad (3.17b)$$

Functions $\rho(\mathbf{r}\sigma, \mathbf{r}'\sigma')$ and $\tilde{\rho}(\mathbf{r}\sigma, \mathbf{r}'\sigma')$ are called the particle and pairing density matrices, respectively. For a time-reversal invariant state $|\Psi\rangle$, both density matrices are time-even and hermitian:

$$\rho(\mathbf{r}\sigma, \mathbf{r}'\sigma') = 4\sigma\sigma' \rho(\mathbf{r} - \sigma, \mathbf{r}' - \sigma')^*, \quad (3.18a)$$

$$\tilde{\rho}(\mathbf{r}\sigma, \mathbf{r}'\sigma') = 4\sigma\sigma' \tilde{\rho}(\mathbf{r} - \sigma, \mathbf{r}' - \sigma')^*. \quad (3.18b)$$

Therefore, the pairing density matrix $\tilde{\rho}(\mathbf{r}\sigma, \mathbf{r}'\sigma')$ is more convenient to use than the standard pairing tensor $\kappa(\mathbf{r}\sigma, \mathbf{r}'\sigma')$ [24],

$$\kappa(\mathbf{r}\sigma, \mathbf{r}'\sigma') = 2\sigma' \tilde{\rho}(\mathbf{r}\sigma, \mathbf{r}', -\sigma'), \quad (3.19)$$

which is an antisymmetric function of the space-spin arguments.

The formulae expressing $\rho(\mathbf{r}\sigma, \mathbf{r}'\sigma')$ and $\tilde{\rho}(\mathbf{r}\sigma, \mathbf{r}'\sigma')$ in terms of the function $\tilde{Z}(\mathbf{r}\sigma, \mathbf{r}'\sigma')$ can be easily derived from those for the density matrix and the pairing tensor [24], and they read

$$\rho = (1 + \tilde{Z}^2)^{-1} \tilde{Z}^2, \quad (3.20a)$$

$$\tilde{\rho} = (1 + \tilde{Z}^2)^{-1} \tilde{Z}. \quad (3.20b)$$

As a result, the density matrices obey the following relations:

$$\tilde{\rho} \cdot \rho = \rho \cdot \tilde{\rho}, \quad (3.21a)$$

$$\rho \cdot \rho + \tilde{\rho} \cdot \tilde{\rho} = \rho. \quad (3.21b)$$

In the above equations, the matrix multiplications and inversions should be understood in the operator sense; i.e., they involve the integration over space and summation over spin variables. For instance:

$$(\tilde{\rho} \cdot \rho)(\mathbf{r}\sigma, \mathbf{r}'\sigma') = \int d^3\mathbf{r}'' \sum_{\sigma''} \tilde{\rho}(\mathbf{r}\sigma, \mathbf{r}''\sigma'') \rho(\mathbf{r}''\sigma'', \mathbf{r}'\sigma'). \quad (3.22)$$

Local HFB densities, i.e., the density matrices for equal spatial arguments, $\mathbf{r}'=\mathbf{r}$, have very well-defined physical interpretations. To see this, let us assume that $\psi_{\mathbf{x}s}(\mathbf{r}\sigma)$ is a normalized single-particle wave function (wave packet) concentrated in a small volume $V_{\mathbf{x}}$ around the point $\mathbf{r}=\mathbf{x}$ and having the spin $s=\sigma$. The corresponding creation operator

$$a_{\mathbf{x}s}^+ = \int d^3\mathbf{r} \sum_{\sigma} \psi_{\mathbf{x}s}(\mathbf{r}\sigma) a_{\mathbf{r}\sigma}^+, \quad (3.23)$$

together with its hermitian conjugate, define the operator

$$\hat{N}_{\mathbf{x}s} = a_{\mathbf{x}s}^+ a_{\mathbf{x}s}, \quad (3.24)$$

which measures the number of particles in the vicinity of the point \mathbf{x} . Since

$$\hat{N}_{\mathbf{x}s}^2 = \hat{N}_{\mathbf{x}s}, \quad (3.25)$$

$\hat{N}_{\mathbf{x}s}$ can be regarded as a projection operator which projects out the component of the many-body wave function that contains one spin- s fermion in the volume $V_{\mathbf{x}}$. Therefore, its average value gives *the probability to find a particle with spin s in this volume*:

$$\mathcal{P}_1(\mathbf{x}s) = \langle \Psi | \hat{N}_{\mathbf{x}s} | \Psi \rangle = V_{\mathbf{x}} \rho(\mathbf{x}s, \mathbf{x}s). \quad (3.26)$$

In a very similar way, the probability of finding a fermion in $V_{\mathbf{x}}$ having opposite spin can be obtained by considering the time-reversed wave function $2\sigma\psi_{\mathbf{x}s}^*(\mathbf{r}, -\sigma)$, cf. Eq. (3.7b). This gives

$$\mathcal{P}_1(\mathbf{x}, -s) = \langle \Psi | \hat{N}_{\mathbf{x},-s} | \Psi \rangle = V_{\mathbf{x}} \rho(\mathbf{x}, -s, \mathbf{x}, -s). \quad (3.27)$$

Due to time-reversal symmetry, probabilities (3.26) and (3.27) are equal.

We may now ask the question, “What is *the probability of finding a pair of fermions with opposite spin projections* in the volume $V_{\mathbf{x}}$, $\mathcal{P}_2(\mathbf{x})$?”. If one considers two *independent* measurements, where in the first one is found the spin- s fermion, and in another one the spin- $(-s)$ fermion, $\mathcal{P}_2(\mathbf{x})$ is equal to the product of individual probabilities; i.e., $\mathcal{P}_1(\mathbf{x}, s)\mathcal{P}_1(\mathbf{x}, -s)$. On the other hand, if one wants to find in $V_{\mathbf{x}}$ both fermions *simultaneously*, one should project out from $|\Psi\rangle$ a corresponding two-fermion component. In this case, $\mathcal{P}_2(\mathbf{x})$ becomes the expectation value of the product of the projection operators $\hat{N}_{\mathbf{x}s}$ and $\hat{N}_{\mathbf{x},-s}$; i.e., $\mathcal{P}_2(\mathbf{x}) = \langle \Psi | \hat{N}_{\mathbf{x}s} \hat{N}_{\mathbf{x},-s} | \Psi \rangle$. Using the Wick theorem, this average value is

$$\mathcal{P}_2(\mathbf{x}) = V_{\mathbf{x}}^2 \rho(\mathbf{x}s, \mathbf{x}s) \rho(\mathbf{x}, -s, \mathbf{x}, -s) + V_{\mathbf{x}}^2 \tilde{\rho}(\mathbf{x}s, \mathbf{x}s) \tilde{\rho}(\mathbf{x}, -s, \mathbf{x}, -s), \quad (3.28)$$

or in terms of the time-even spin-averaged densities:

$$\mathcal{P}_2(\mathbf{x}) = \frac{1}{4}V_{\mathbf{x}}^2\rho(\mathbf{x})^2 + \frac{1}{4}V_{\mathbf{x}}^2\tilde{\rho}(\mathbf{x})^2, \quad (3.29)$$

for

$$\rho(\mathbf{r}) = \sum_{\sigma} \rho(\mathbf{r}\sigma, \mathbf{r}\sigma), \quad (3.30a)$$

$$\tilde{\rho}(\mathbf{r}) = \sum_{\sigma} \tilde{\rho}(\mathbf{r}\sigma, \mathbf{r}\sigma). \quad (3.30b)$$

Since the first terms in Eqs. (3.28) and (3.29) describe the probability of finding the two fermions in independent measurements, the second terms in these equations should be interpreted as the probability of finding *the correlated pair* at point \mathbf{x} .

The above arguments allow us to give a transparent physical interpretation to the local HFB densities. Namely, as usual, $\rho(\mathbf{r})$ represents the probability density of finding a particle at the given point. On the other hand, $\tilde{\rho}(\mathbf{r})^2$ gives the correlation probability density; i.e., the probability of finding a pair of fermions *in excess* of the probability of finding two uncorrelated fermions.

It is important to note that kinematic conditions (3.21), which result from the fact that $|\Psi\rangle$ is an independent-quasiparticle state, Eq. (3.4), *do not* directly constrain the local values of the particle and pairing density matrices. In particular, there is no obvious kinematic relation between the probability of finding two independent particles at a given point of space, and the probability of finding a correlated pair at the same point. In particular, the first one can be small, while the second can be large (see discussion in Secs. III C 1 and V F). This result means that in such a situation the experiments probing the presence of two particles will always find these two particles as correlated pairs without a “background” characteristic of two independent particles.

Relations (3.20) imply that all three functions: $\tilde{Z}(\mathbf{r}\sigma, \mathbf{r}'\sigma')$, $\rho(\mathbf{r}\sigma, \mathbf{r}'\sigma')$, and $\tilde{\rho}(\mathbf{r}\sigma, \mathbf{r}'\sigma')$ are diagonal in the canonical basis, cf. Eq. (3.12). Using the standard notation for the eigenvalues of ρ and $\tilde{\rho}$, one obtains

$$\int d^3\mathbf{r}' \sum_{\sigma'} \rho(\mathbf{r}\sigma, \mathbf{r}'\sigma') \check{\psi}_{\mu}(\mathbf{r}'\sigma') = v_{\mu}^2 \check{\psi}_{\mu}(\mathbf{r}\sigma), \quad (3.31a)$$

$$\int d^3\mathbf{r}' \sum_{\sigma'} \tilde{\rho}(\mathbf{r}\sigma, \mathbf{r}'\sigma') \check{\psi}_{\mu}(\mathbf{r}'\sigma') = u_{\mu} v_{\mu} \check{\psi}_{\mu}(\mathbf{r}\sigma), \quad (3.31b)$$

where the real factors v_{μ} and u_{μ} are given by

$$v_{\mu} = v_{\bar{\mu}} = \frac{z_{\mu}}{\sqrt{1 + z_{\mu}^2}}, \quad u_{\mu} = u_{\bar{\mu}} = \frac{1}{\sqrt{1 + z_{\mu}^2}}. \quad (3.32)$$

A completeness of the canonical basis leads to standard expressions for the density matrices:

$$\rho(\mathbf{r}\sigma, \mathbf{r}'\sigma') = \sum_{\mu} v_{\mu}^2 \check{\psi}_{\mu}^*(\mathbf{r}\sigma) \check{\psi}_{\mu}(\mathbf{r}'\sigma'), \quad (3.33a)$$

$$\tilde{\rho}(\mathbf{r}\sigma, \mathbf{r}'\sigma') = \sum_{\mu} u_{\mu} v_{\mu} \check{\psi}_{\mu}^*(\mathbf{r}\sigma) \check{\psi}_{\mu}(\mathbf{r}'\sigma'), \quad (3.33b)$$

Equation (3.31a) represents the traditional definition of the canonical states as the eigenstates of the HFB density matrix. It also shows that the canonical states are the *natural states* [68–73] for the density matrix corresponding to the independent-quasiparticle many-body state $|\Psi\rangle$, Eq. (3.17a), and the eigenvalues v_μ^2 are the corresponding natural occupation numbers.

One may now easily repeat the previous analysis of probabilities of finding a particle, or a pair of particles, in the canonical-basis single-particle state $\check{\psi}_\mu(\mathbf{r}\sigma)$. The result, analogous to Eqs. (3.28) and (3.29), is $\mathcal{P}_1(\mu)=v_\mu^2$, and $\mathcal{P}_2(\mu)=u_\mu^2v_\mu^2+v_\mu^4$. In this case, due to the normalization condition $u_\mu^2+v_\mu^2=1$, $\mathcal{P}_1(\mu)=\mathcal{P}_2(\mu)$. This result means that the particles in the canonical states with indices μ and $\bar{\mu}$ are extremely correlated spatially; i.e., the probability of finding the canonical pair, $u_\mu^2v_\mu^2$, is directly dependent on the probability of finding two independent canonical fermions, v_μ^4 . However, as discussed above, a similar direct relation between $\mathcal{P}_1(\mathbf{x})$ and $\mathcal{P}_2(\mathbf{x})$ does not exist. In particular $\mathcal{P}_1(\mathbf{x})\neq\mathcal{P}_2(\mathbf{x})$.

1. Examples of particle and pairing densities

Figures 1 and 2 display the particle and pairing local spherical neutron HFB densities $\rho(r)$ and $\tilde{\rho}(r)$, Eq. (3.30), as functions of the radial coordinate $r=|\mathbf{r}|$. Results are shown for several tin isotopes across the stability valley. For particle densities, the results obtained with the SkP and SkP $^\delta$ interactions are almost indistinguishable. Therefore, Fig. 1 (middle panel) shows results for the SIII $^\delta$ interaction. For pairing densities, compared in Fig. 2 are results for SkP, SkP $^\delta$, and D1S effective interactions.

The particle densities obtained with these three effective interactions are qualitatively very similar. One can see that adding neutrons results in a simultaneous increase of the central neutron density, and of the density in the surface region. The relative magnitude of the two effects is governed by a balance between the volume and the surface asymmetry energies of effective interactions. Since all three forces considered have been fitted in a similar way to bulk nuclear properties, including the isospin dependence, the resulting balance between the volume and the surface isospin effects is similar. Of course, this does not exclude some differences which are seen when a more detailed comparison is carried out.

The pairing densities shown in Fig. 2 reflect different characters of the interactions used in the p-p channel. The contact force (the SkP $^\delta$ results) leads to the pairing densities which are, in general, largest at the origin and decrease towards the surface. (This general trend is slightly modified by shell fluctuations resulting from contributions from orbitals near the Fermi level.) At the surface, the isospin dependence of SkP $^\delta$ is fairly weak. For example, there is very little difference between the pairing densities in ^{150}Sn and ^{172}Sn . These results are characteristic for the volume-type pairing correlations.

A different pattern appears for the SkP results, where the density dependence renders the p-p interaction strongly peaked at the surface. In this case, the pairing densities tend to increase when going from the center of the nucleus towards its surface. Again, the shell fluctuations are superimposed on top of this general behavior. In particular, the central bump in the pairing density in ^{120}Sn is due to a contribution from the $3s_{1/2}$ state. A more pronounced dependence on the neutron excess is seen in the surface region. Especially near the drip line, the pairing density develops a long tail extending towards large distances.

The results obtained for the finite-range interaction D1S exhibit intermediate features between the surface and the volume type of pairing correlations. In particular, in the nuclear interior one observes a fairly large region of relatively constant pairing density. The overall magnitude of the pairing densities is very similar in all three approaches. In particular, it is interesting to see that at the nuclear surface ($r \sim 5$ fm) all three pairing densities in ^{120}Sn are very close to 0.018 fm^{-3} .

IV. HARTREE-FOCK-BOGOLIUBOV EQUATIONS

We begin this section by presenting basic definitions and equations of the HFB approach. The HFB theory is discussed in many textbooks and review articles (see Refs. [74,24], for example), while its aspects pertaining to the coordinate representation have been presented in Ref. [52]. An earlier discussion of the coordinate-representation HFB formalism has been given by Bulgac, whose work is available only in preprint form [33]. Recently, similar methods have also been applied to a description of light nuclei [37,38]. It is also worth mentioning that the Green function approach in the coordinate representation (the Gor'kov method [75]), is formally equivalent to HFB – cf. discussion in Refs. [41,42]. The only difference between the methods lies in the explicit energy dependence of the quasiparticle mass operator, an analog to the p-h single-particle HF Hamiltonian (see below).

A. HFB energy and HFB potentials

The two-body effective Hamiltonian of a nuclear system can be written in the coordinate representation as

$$\begin{aligned} \hat{H} = & \int d^3\mathbf{r} d^3\mathbf{r}' \sum_{\sigma\sigma'} T(\mathbf{r}\sigma, \mathbf{r}'\sigma') a_{\mathbf{r}\sigma}^+ a_{\mathbf{r}'\sigma'} \\ & + \frac{1}{4} \int d^3\mathbf{r}_1 d^3\mathbf{r}_2 d^3\mathbf{r}'_1 d^3\mathbf{r}'_2 \sum_{\sigma_1\sigma_2\sigma'_1\sigma'_2} V(\mathbf{r}_1\sigma_1, \mathbf{r}_2\sigma_2; \mathbf{r}'_1\sigma'_1, \mathbf{r}'_2\sigma'_2) a_{\mathbf{r}_1\sigma_1}^+ a_{\mathbf{r}_2\sigma_2}^+ a_{\mathbf{r}'_2\sigma'_2} a_{\mathbf{r}'_1\sigma'_1}. \end{aligned} \quad (4.1)$$

The first term represents the kinetic energy, while the second one is the two-body interaction. In the following, we assume that $V(\mathbf{r}_1\sigma_1, \mathbf{r}_2\sigma_2; \mathbf{r}'_1\sigma'_1, \mathbf{r}'_2\sigma'_2)$ includes the exchange terms.

The average energy of the Hamiltonian (4.1) in a time-even HFB vacuum (3.4) reads

$$\begin{aligned} E_{\text{HFB}} = & \int d^3\mathbf{r} d^3\mathbf{r}' \sum_{\sigma\sigma'} T(\mathbf{r}\sigma, \mathbf{r}'\sigma') \rho(\mathbf{r}'\sigma', \mathbf{r}\sigma) \\ & + \frac{1}{2} \int d^3\mathbf{r}_1 d^3\mathbf{r}_2 d^3\mathbf{r}'_1 d^3\mathbf{r}'_2 \sum_{\sigma_1\sigma_2\sigma'_1\sigma'_2} V(\mathbf{r}_1\sigma_1, \mathbf{r}_2\sigma_2; \mathbf{r}'_1\sigma'_1, \mathbf{r}'_2\sigma'_2) \rho(\mathbf{r}'_1\sigma'_1, \mathbf{r}_1\sigma_1) \rho(\mathbf{r}'_2\sigma'_2, \mathbf{r}_2\sigma_2) \\ & - \frac{1}{4} \int d^3\mathbf{r}_1 d^3\mathbf{r}_2 d^3\mathbf{r}'_1 d^3\mathbf{r}'_2 \sum_{\sigma_1\sigma_2\sigma'_1\sigma'_2} 4\sigma_1\sigma'_2 V(\mathbf{r}_1, -\sigma_1, \mathbf{r}_2\sigma_2; \mathbf{r}'_1\sigma'_1, \mathbf{r}'_2, -\sigma'_2) \tilde{\rho}(\mathbf{r}_1\sigma_1, \mathbf{r}_2\sigma_2) \tilde{\rho}(\mathbf{r}'_1\sigma'_1, \mathbf{r}'_2\sigma'_2). \end{aligned} \quad (4.2)$$

The last two terms are the interaction energies in the particle-hole (p-h) and in the particle-particle (p-p) channels, respectively. Equivalently, one can define the p-h and p-p single-particle Hamiltonians, $h(\mathbf{r}\sigma, \mathbf{r}'\sigma') = T(\mathbf{r}\sigma, \mathbf{r}'\sigma') + \Gamma(\mathbf{r}\sigma, \mathbf{r}'\sigma')$ and $\tilde{h}(\mathbf{r}\sigma, \mathbf{r}'\sigma')$, respectively:

$$\Gamma(\mathbf{r}\sigma, \mathbf{r}'\sigma') = \int d^3\mathbf{r}_2 d^3\mathbf{r}'_2 \sum_{\sigma_2\sigma'_2} V(\mathbf{r}\sigma, \mathbf{r}_2\sigma_2; \mathbf{r}'\sigma', \mathbf{r}'_2\sigma'_2) \rho(\mathbf{r}'_2\sigma'_2, \mathbf{r}_2\sigma_2), \quad (4.3a)$$

$$\tilde{h}(\mathbf{r}\sigma, \mathbf{r}'\sigma') = \int d^3\mathbf{r}'_1 d^3\mathbf{r}'_2 \sum_{\sigma'_1\sigma'_2} 2\sigma'\sigma'_2 V(\mathbf{r}\sigma, \mathbf{r}', -\sigma'; \mathbf{r}'_1\sigma'_1, \mathbf{r}'_2, -\sigma'_2) \tilde{\rho}(\mathbf{r}'_1\sigma'_1, \mathbf{r}'_2\sigma'_2), \quad (4.3b)$$

which gives the HFB energy in the form:

$$E_{\text{HFB}} = \frac{1}{2} \int d^3\mathbf{r} d^3\mathbf{r}' \sum_{\sigma\sigma'} \left(T(\mathbf{r}\sigma, \mathbf{r}'\sigma') \rho(\mathbf{r}'\sigma', \mathbf{r}\sigma) + h(\mathbf{r}\sigma, \mathbf{r}'\sigma') \rho(\mathbf{r}'\sigma', \mathbf{r}\sigma) + \tilde{h}(\mathbf{r}\sigma, \mathbf{r}'\sigma') \tilde{\rho}(\mathbf{r}'\sigma', \mathbf{r}\sigma) \right). \quad (4.4)$$

Additional terms coming from the density-dependence of the two-body interaction V have been for simplicity omitted in Eqs. (4.3a), (4.3b), and (4.4). The last term in Eq. (4.4),

$$E_{\text{pair}} = \frac{1}{2} \int d^3\mathbf{r} d^3\mathbf{r}' \sum_{\sigma\sigma'} \tilde{h}(\mathbf{r}\sigma, \mathbf{r}'\sigma') \tilde{\rho}(\mathbf{r}'\sigma', \mathbf{r}\sigma), \quad (4.5)$$

represents the pairing energy. We also define the average magnitude of pairing correlations by the formula [52]

$$\langle \Delta \rangle = -\frac{1}{N^\tau} \int d^3\mathbf{r} d^3\mathbf{r}' \sum_{\sigma\sigma'} \tilde{h}(\mathbf{r}\sigma, \mathbf{r}'\sigma') \rho(\mathbf{r}'\sigma', \mathbf{r}\sigma), \quad (4.6)$$

where N^τ is the number of particles (neutrons or protons).

The p-h and p-p mean fields (4.3) have particularly simple forms for the Skyrme interaction [52]. In Appendix A we present the form of the p-h and p-p mean-field Hamiltonians in the case of a local two-body finite-range Gogny interaction.

1. Examples of the p-h and p-p potentials

In this section we aim at comparing the self-consistent potentials obtained with the Skyrme and Gogny forces. Such a comparison cannot be carried out directly, because the corresponding integral kernels $h(\mathbf{r}\sigma, \mathbf{r}'\sigma')$ and $\tilde{h}(\mathbf{r}\sigma, \mathbf{r}'\sigma')$ have different structure. For the Skyrme interaction, they are proportional to $\delta(\mathbf{r}-\mathbf{r}')$ and depend also on the differential operators (linear momenta) [52], while for the Gogny interaction they are sums of terms proportional to $\delta(\mathbf{r}-\mathbf{r}')$ and terms which are functions of \mathbf{r} and \mathbf{r}' (Appendix A).

Therefore, for the purpose of the present comparison we introduce operational prescriptions to calculate the local parts of the integral kernels:

$$U(\mathbf{r}) = \mathcal{LOC} [\Gamma(\mathbf{r}\sigma, \mathbf{r}'\sigma')], \quad (4.7a)$$

$$\tilde{U}(\mathbf{r}) = \mathcal{LOC} [\tilde{h}(\mathbf{r}\sigma, \mathbf{r}'\sigma')]. \quad (4.7b)$$

These formal definitions in practice amount to: (i) disregarding the momentum-dependent terms of the kernels, (ii) considering only terms with $\sigma=\sigma'=1/2$ (which by time reversal symmetry are equal to those with $\sigma=\sigma'=-1/2$), and (iii) taking into account *only* the term proportional to $\delta(\mathbf{r}-\mathbf{r}')$, if such a term is present. The expressions for $U(\mathbf{r})$ and $\tilde{U}(\mathbf{r})$

can be found in Appendix A of Ref. [52] (Skyrme interaction) and in Appendix A (Gogny interaction). In the Skyrme calculations, the contribution of the Coulomb interaction to $\tilde{U}(\mathbf{r})$ has been neglected since it is estimated to be small.

In the case of finite-range local interactions (such as Gogny or Coulomb), the corresponding non-local pairing field $h(\mathbf{r}\sigma, \mathbf{r}'\sigma')$ does not contain the term proportional to $\delta(\mathbf{r}-\mathbf{r}')$ (see Appendix A). Consequently, the local field $\tilde{U}(\mathbf{r})$ cannot be extracted in a meaningful way. For instance, the diagonal (i.e., $\mathbf{r}'=\mathbf{r}$) part of the D1S pairing field is positive; i.e., it is dominated by the short-range repulsive component rather than the long-range attractive part [18,58].

In the spherical case, the potentials $U(\mathbf{r})$ and $\tilde{U}(\mathbf{r})$ depend on only one radial coordinate $r=|\mathbf{r}|$. This facilitates the qualitative comparison between different forces. Figure 3 displays the self-consistent spherical local p-h potentials $U(r)$, Eq. (4.7), for several tin isotopes, calculated with SkP, SIII $^\delta$, and D1S interactions (the results with SkP $^\delta$ are very close to those with SkP). The terms depending on the angular momentum, which result from a reduction to the radial coordinate, are not included. (The general behavior of the self-consistent p-h potentials has already been discussed many times in the literature, e.g. [76–78], and we include these results only for completeness and for a comparison with the corresponding p-p potentials, for which the detailed analysis does not exist.)

Qualitatively, the results for $U(r)$ obtained with different effective forces are quite similar, which reflects the fact that all these interactions correctly describe global nuclear properties. In particular, one sees that with increasing neutron excess the neutron potentials become more shallow in the interior and more wide in the outer region. Interestingly, for each of these three forces there exists a pivoting point at which the potential does not depend on the neutron excess. For the three forces presented, this occurs at $r=5.9, 4.6,$ and 5.4 fm, respectively. The differences in the overall depths of the average potentials reflect the associated effective masses (i.e., the non-local contributions of the two-body interactions).

The analogous results for the p-p potentials $\tilde{U}(r)$ calculated for the SkP and SkP $^\delta$ interactions are shown in Fig. 4. One can see that the different character of pairing interactions is directly reflected in the form of the p-p potentials. Particularly noteworthy is the fact that the density-dependent pairing interaction in SkP yields a very pronounced surface-peaked potential (the behavior of $\tilde{U}(r)$ at large distances is further discussed in Sec. V G). One can easily understand its form by recalling that this potential is equal to the product of the pairing density $\tilde{\rho}(r)$ [Fig. 2] and the function which roughly resembles the behavior of DDDI of Eq. (2.3); i.e., small in the interior and large in the outer region. Of course, values of $\tilde{\rho}(r)$ and $\tilde{U}(r)$ depend on each other by the fact that they both result from a self-consistent solution of the complete HFB equation in which the p-h and p-p channels are coupled together (see Sec. IV C). Similar results were also obtained in Refs. [79] (in the HFB+SkP model) and [80] (in the QLM) for the proton-rich rare-earth nuclei.

Since the p-h channel provides the bulk part of the interaction energy, the particle densities $\rho(r)$ closely follow the pattern of the p-h potentials (i.e., the density is large where the potential is deep). An analogous relation is only partly true for $\tilde{\rho}(r)$ and $\tilde{U}(r)$; i.e., even the dramatic surface character of the SkP p-p potential (Fig. 4) does not result in the pairing density being similarly peaked at the surface. Recall that the contributions to $\tilde{\rho}(r)$ come mainly from a few wave functions near the Fermi surface, and that the form of these wave functions is mainly governed by the p-h channel. Since these wave functions must

have significant components in the interior, the resulting pairing densities cannot exactly fit into the surface-peaked p-p potentials. Nevertheless, a clear tendency towards surface localization is evident in Fig. 2.

In the case of the pure contact interaction (SkP $^\delta$ calculations) the p-p potential is exactly proportional to the pairing density [52] with the proportionality constant $V_0/2$ equal to -80 MeV fm^3 [53]. Therefore, the resulting potential is concentrated at the origin and increases towards the surface. (Early calculations of p-p potentials in the QLM with the density-independent delta interaction can be found in Ref. [43]. The general behavior of $\tilde{U}(r)$, denoted as $\Delta(r)$ therein, is very similar to our SkP $^\delta$ results.)

B. HFB equations in the coordinate representation

The variation of the HFB energy with respect to independent parameters $Z(\mathbf{r}\sigma, \mathbf{r}'\sigma')$ leads to the HFB equation [24,52],

$$\int d^3\mathbf{r}' \sum_{\sigma'} \begin{pmatrix} h(\mathbf{r}\sigma, \mathbf{r}'\sigma') & \tilde{h}(\mathbf{r}\sigma, \mathbf{r}'\sigma') \\ \tilde{h}(\mathbf{r}\sigma, \mathbf{r}'\sigma') & -h(\mathbf{r}\sigma, \mathbf{r}'\sigma') \end{pmatrix} \begin{pmatrix} \phi_1(E, \mathbf{r}'\sigma') \\ \phi_2(E, \mathbf{r}'\sigma') \end{pmatrix} = \begin{pmatrix} E + \lambda & 0 \\ 0 & E - \lambda \end{pmatrix} \begin{pmatrix} \phi_1(E, \mathbf{r}\sigma) \\ \phi_2(E, \mathbf{r}\sigma) \end{pmatrix}, \quad (4.8)$$

where $\phi_1(E, \mathbf{r}\sigma)$ and $\phi_2(E, \mathbf{r}\sigma)$ are upper and lower components of the two-component single-quasiparticle HFB wave function, and λ is the Fermi energy.

Properties of the HFB equation in the spatial coordinates, Eq. (4.8), have been discussed in Ref. [52]. In particular, it has been shown that the spectrum of eigenenergies E is continuous for $|E| > -\lambda$ and discrete for $|E| < -\lambda$. Since for $E > 0$ and $\lambda < 0$ the lower components $\phi_2(E, \mathbf{r}\sigma)$ are localized functions of \mathbf{r} , the density matrices,

$$\rho(\mathbf{r}\sigma, \mathbf{r}'\sigma') = \sum_{0 < E_n < -\lambda} \phi_2(E_n, \mathbf{r}\sigma) \phi_2^*(E_n, \mathbf{r}'\sigma') + \int_{-\lambda}^{\infty} dn(E) \phi_2(E, \mathbf{r}\sigma) \phi_2^*(E, \mathbf{r}'\sigma'), \quad (4.9a)$$

$$\tilde{\rho}(\mathbf{r}\sigma, \mathbf{r}'\sigma') = - \sum_{0 < E_n < -\lambda} \phi_2(E_n, \mathbf{r}\sigma) \phi_1^*(E_n, \mathbf{r}'\sigma') - \int_{-\lambda}^{\infty} dn(E) \phi_2(E, \mathbf{r}\sigma) \phi_1^*(E, \mathbf{r}'\sigma'), \quad (4.9b)$$

are always localized.

For the case of a discretized continuum, Sec. V A, the integral over the energy reduces to a discrete sum [52] but one should still carefully distinguish between contributions coming from the discrete ($E_n < -\lambda$) and discretized ($E_n > -\lambda$) states. The orthogonality relation for the single-quasiparticle HFB wave functions reads

$$\int d^3\mathbf{r} \sum_{\sigma} [\phi_1^*(E_n, \mathbf{r}\sigma) \phi_1(E_{n'}, \mathbf{r}\sigma) + \phi_2^*(E_n, \mathbf{r}\sigma) \phi_2(E_{n'}, \mathbf{r}\sigma)] = \delta_{n,n'}. \quad (4.10)$$

It is seen from Eq. (4.10) that the lower components are not normalized. Their norms,

$$N_n = \int d^3\mathbf{r} \sum_{\sigma} |\phi_2(E_n, \mathbf{r}\sigma)|^2, \quad (4.11)$$

define the total number of particles

$$N = \int d^3\mathbf{r} \rho(\mathbf{r}) = \sum_n N_n. \quad (4.12)$$

In the HFB theory, the localization condition (3.5) discussed in Sec. III is automatically guaranteed for any system with negative Fermi energy λ . This allows studying nuclei which are near the particle drip lines where the Fermi energy approaches zero through negative values.

For the Skyrme interaction, the HFB equation (4.8) is a differential equation in spatial coordinates [52]. If the spherical symmetry is imposed, which is assumed in the following, this equation reads

$$\left[-\frac{d}{dr} \begin{pmatrix} M & \tilde{M} \\ \tilde{M} & -M \end{pmatrix} \frac{d}{dr} + \begin{pmatrix} U - \lambda & \tilde{U} \\ \tilde{U} & -U + \lambda \end{pmatrix} \right] \begin{pmatrix} r\phi_1(E, r) \\ r\phi_2(E, r) \end{pmatrix} = E \begin{pmatrix} r\phi_1(E, r) \\ r\phi_2(E, r) \end{pmatrix}, \quad (4.13)$$

where M and \tilde{M} are p-h and p-p mass parameters, respectively, and U and \tilde{U} are defined in Sec. IV A. Due to the spherical symmetry, Eq. (4.13) is solved separately for each partial wave (j, ℓ) . The potentials include also the centrifugal and spin-orbit terms, and the p-h mass parameter M is expressed in terms of the effective mass m^* ; i.e., $M = \hbar^2/2m^*$, see Ref. [52] for details.

Before discussing the properties of the HFB wave functions, we analyze the structure of the spherical HFB Hamiltonian of Eq. (4.13). Figure 5 shows the behavior of $M(r)$ and $\tilde{M}(r)$, and $U(r)$ and $\tilde{U}(r)$ (central parts only) obtained for neutrons in ^{120}Sn in the HFB+SkP model. The p-h functions, $M(r)$ and $U(r)$, are similar to those obtained in other mean-field theories. $M(r)$ has values close to $\hbar^2/2m \simeq 20 \text{ MeV fm}^2$, which corresponds to the value of the free nucleon mass m . In the nuclear interior, this function has slightly smaller values, because the effective mass m^* is here slightly larger than m . This effect is due to the non-zero isovector effective mass of the Skyrme SkP interaction; recall that for this interaction the nuclear-matter value of the isoscalar effective mass is $m^*=m$. The central potential $U(r)$ has the standard depth of about 40 MeV and disappears around $r=7.5 \text{ fm}$.

The form of the p-p functions, $\tilde{M}(r)$ and $\tilde{U}(r)$, characterizes the pairing properties of the system. One may note that both these functions are essentially peaked at the nuclear surface. In ^{120}Sn they also exhibit central bumps resulting from the fact that in this nucleus the neutron $3s_{1/2}$ orbital is located near the Fermi surface. Values of $\tilde{M}(r)$ are (in the chosen units) an order of magnitude smaller than those of $\tilde{U}(r)$. This should be compared with the results obtained for the p-h channel, where the values of $M(r)$ are only about a factor of 2 smaller than those of $U(r)$. It means that, for the SkP parametrization, the kinetic term in the p-p channel (which simulates the finite-range effects) is relatively less important than the kinetic energy term in the p-h channel.

C. Single-quasiparticle wave functions

This section contains the discussion of HFB wave functions $\phi_1(E, r)$ and $\phi_2(E, r)$ (Sec. IV C 1), canonical-basis wave functions $\tilde{\psi}_\mu(r)$ (Sec. IV C 2), and HF+BCS wave functions (Sec. IV C 3). In the following, the HFB equation (4.13) was solved in the spherical box of the radius $R_{\text{box}}=20 \text{ fm}$ for the $j=1/2$ and $\ell=0$ ($s_{1/2}$) neutron states; i.e., for vanishing centrifugal, Coulomb, and spin-orbit potentials. The calculations were performed for ^{120}Sn .

1. Examples of the single-quasiparticle wave functions

The neutron single-quasiparticle wave functions are presented in Fig. 6. The upper components $r\phi_1(E_n, r)$, and the lower components $r\phi_2(E_n, r)$, are plotted in the left and right columns, respectively. Because a box of a finite radius was used, the particle continuum is discretized. The positive quasiparticle eigenenergies E_n are in increasing order numbered by the index n , and their values are tabulated in the left portion of Table I, together with the norms of the lower components (4.11), $N_n = 4\pi \int r^2 dr |\phi_2(E_n, r)|^2$. Since the lower components define the particle density matrix [Eq. (4.9a)] the numbers $(2j+1)N_n$ (i.e., $2N_n$ for the $j=1/2$ case considered) constitute contributions of a given quasiparticle state to the total number of neutrons (see Eq. (4.12)).

Wave functions in Fig. 6, and the entries in Table I, have been ordered from the bottom to the top not according to the excitation-energy index n , but rather according to numbers of nodes of the *large* component. (The large component is the lower component for hole states and the upper component for particle states – see Fig. 6.) The lower component of the $n=8$ state is large, and it has zero nodes; therefore it is plotted at the bottom of the figure. Next comes the $n=5$ state, whose lower component has one node, and the $n=1$ state with two nodes. Lower components of these three states are larger than their upper components and they contribute almost 2 particles each to the total number of neutrons. Consequently, these quasiparticle states should be associated with the $1s_{1/2}$, $2s_{1/2}$, and $3s_{1/2}$, single-hole states.

For all other calculated $s_{1/2}$ states the upper components are larger than the lower ones, and these states contribute small fractions to the particle number, see Table I. Consequently, these quasiparticle states should be associated with the $s_{1/2}$ single-particle states. The behavior of these wave functions differs in the nuclear interior (i.e., for $r < R$ where $R \sim 7$ fm is the nuclear radius) and outside ($r > R$). Since the wavelength of the upper component is roughly proportional to $1/\sqrt{E_n + \lambda - U(r)}$, the ratio of the corresponding wavelengths behaves as

$$\frac{\lambda_{\text{out}}}{\lambda_{\text{in}}} \approx \sqrt{1 + \frac{|U(0)|}{E_n + \lambda}}, \quad (4.14)$$

where $U(0)$ is the depth of the neutron potential well. For the $s_{1/2}$ neutron states in ^{120}Sn the excitation energy, $E_n + \lambda$, can be found from Table I ($\lambda = -7.94$ MeV), and $U(0) \sim -45$ MeV (see Fig. 5).

The upper component of the $n=2$ state has three nodes. However, for $r > R$ the exterior part of the wave function corresponds to a half-wave; i.e., it represents the lowest-energy discretized continuum state. Since $E_n + \lambda$ is only 0.97 MeV, the wavelength in the nuclear interior is ~ 6.5 times shorter than λ_{out} . The next two wave functions have four and five nodes in their upper components. Compared to the $n=2$ state, they exhibit shorter wavelengths both outside and inside the nucleus (the corresponding excitation energies are larger), and the ratio $\lambda_{\text{out}}/\lambda_{\text{in}}$ decreases according to Eq. (4.14).

The quasiparticle states with $n=2, 3$, and 4 should be associated with the $4s_{1/2}$, $5s_{1/2}$, and $6s_{1/2}$ states in the particle continuum. Of course, the values of their quasiparticle energies strongly depend on the size of the box, because the wavelength of their exterior parts will increase with increasing R_{box} (is roughly proportional to R_{box}).

From the above discussion, one can see that the structure of large components resembles very much that of the HF wave functions. Moreover, the small components are very small compared to the large ones; in order to plot both of them in the same scale (Fig. 6) they have to be multiplied by factors from 10 to 25. Only the lowest quasiparticle state ($n=1$), which corresponds to the $3s_{1/2}$ state near the Fermi surface, has the two components of a similar magnitude. It is to be noted, however, that the detailed structure of small components is decisive for a description of the pairing correlations. Indeed, both components are coupled in the HFB equations by the pairing fields $\tilde{h}(\mathbf{r}\sigma, \mathbf{r}'\sigma')$ or \tilde{U} .

In agreement with general asymptotic properties of the upper and lower components [33,52], one sees in Fig. 6 that the lower components vanish at large distances for all quasiparticle states, regardless of the excitation energy. Consequently, the resulting density matrix is localized. It is interesting to observe (Table I) that the norms of the lower components N_n do not behave monotonically with quasiparticle energy. Namely, N_n is about 0.0002 for $n=2$; then it increases to 0.0019 at $n=6$, and only then it decreases to about 0.0001 at $n=11$. This means that the pairing correlations couple states with very high quasiparticle excitations and short-wavelength upper components; i.e., located high up in the particle continuum. In the considered example, only by going to the energy region of as high as 50 MeV is the pairing coupling to the continuum states exhausted.

Apart from the $n=1$ state which has the quasiparticle energy E smaller than $-\lambda$, for all other quasiparticle states the upper components oscillate at large distances; i.e., these states belong to the HFB continuum. This seems natural for the $4s_{1/2}$, $5s_{1/2}$, and $6s_{1/2}$ states discussed above, but it also holds for the deep-hole states $1s_{1/2}$ and $2s_{1/2}$. This illustrates the physical property of the deep-hole states that once such a state is excited, it is coupled to the particle continuum and acquires some particle width. Of course, before such a hole is created (e.g., one-quasiparticle excitation in the neighboring nucleus) the nucleus (i.e., quasiparticle vacuum) is perfectly particle-bound and the contributions from the deep-hole-like quasiparticle states to the density matrix are localized in space.

2. Examples of the canonical-basis wave functions

By solving the integral eigenequation for the density matrix (3.31a), one obtains the canonical-basis wave functions $\tilde{\psi}_\mu(r)$. Actually, when the HFB equation (4.13) is solved by a discretization method on a spatial mesh, as is done here, the density matrix is represented by a matrix and the integral eigenequation becomes the usual matrix eigenproblem. In the present application to ^{120}Sn , the mesh of equally spaced points with $\Delta r=0.25$ fm was used and then the canonical-basis wave functions were obtained on the same mesh of points. These wave functions are plotted in Fig. 7, while other characteristics of the canonical states are listed on the right-hand side portion of Table I. Here the states are ordered from bottom to top according to their occupation probabilities v_μ^2 .

When μ increases from 1 to 5, the number of nodes of the canonical-basis wave functions increases from zero to four. Therefore, these states represent the $1s_{1/2}$ to $5s_{1/2}$ single-particle states. The first three of them have large occupation probabilities v_μ^2 , negative average values ϵ_μ of the p-h Hamiltonian, and positive pairing gaps Δ_μ [see Eq. (4.22)]. These states have all the characteristics of bound single-particle states, and their wave functions strongly resemble the large components of the $n=8$, 5, and 1 quasiparticle states shown in Fig. 6.

It is interesting to note that the two states $\mu=4$ and 5 follow exactly the same pattern of localized wave functions, despite the *positive* values of ϵ_μ . Therefore, these two states can be understood as the representatives of the positive-energy spectrum in the ground-state of ^{120}Sn . We purposely avoid using the term “particle continuum”, because these orbitals represent discrete and localized eigenstates of the density matrix.

Table I shows that the occupation probabilities of the canonical-basis states with $\mu=4, \dots, 7$ decrease very rapidly. In fact only states with $\mu=4$ and 5 have tangible occupation probabilities; one can say that the remaining orbitals are entirely empty. This feature has to be compared with the sequence of norms of the lower HFB components, N_n , which do not fall down to zero at even a nearly similar pace. This demonstrates that even if the convergence of the HFB eigenproblem requires high quasiparticle energies, the number of physically important single-particle states is very restrained. Unfortunately, as discussed below in Sec. IV D, one cannot obtain the canonical-basis states without actually solving the HFB equations up to high energies. For $\mu=6$ and higher, the occupation probabilities are so small that the numerical procedure used to diagonalize the density matrix returns accidental mixtures of almost degenerate eigenfunctions. This is seen in Fig. 7, where the wave function with $\mu=6$ has six nodes instead of five, expected from the regular sequence. Also the energies ϵ_μ are for these nearly empty states randomly scattered between 40 and 70 MeV, while the pairing gaps Δ_μ are scattered around zero.

3. Examples of the BCS quasiparticle wave functions

The BCS quasiparticle wave functions can be obtained by enforcing the BCS approximation on the HFB equations. This is done by setting the pairing Hamiltonian \tilde{h} to a constant; i.e., by using $\tilde{M}(r)=0$ and $\tilde{U}(r)=-1.232$ MeV. This value of \tilde{U} is equal to minus the HFB average neutron pairing gap, as defined in Eq. (4.6). As seen in Fig. 8, the pattern of large components follows closely that obtained in the HFB method, while the shapes of small components are entirely different. Indeed, since in the BCS approximation lower and upper components are simply proportional, small and large components have the same asymptotic properties. This leads to serious inconsistencies, because the small lower components *are not* localized any more, and introduce an unphysical particle gas in the density matrix, while the small upper components *are* localized and the corresponding deep-hole states have no particle width.

D. HFB equations in the canonical basis

It is seen in Eqs. (4.2) and (4.3) that the two-body interaction enters the p-h and p-p channels in a different way. This is particularly conspicuous when the canonical basis (3.31) is used; i.e.,

$$E_{\text{HFB}} = \sum_{\nu} \check{T}_{\mu\mu} v_{\mu}^2 + \frac{1}{2} \sum_{\mu\nu} \check{F}_{\mu\nu} v_{\mu}^2 v_{\nu}^2 - \frac{1}{4} \sum_{\mu\nu} \check{G}_{\mu\nu} u_{\mu} v_{\mu} u_{\nu} v_{\nu}, \quad (4.15)$$

where

$$\check{F}_{\mu\nu} = \frac{1}{2} (\check{V}_{\mu\nu\mu\nu} + \check{V}_{\mu\bar{\nu}\mu\bar{\nu}}), \quad (4.16a)$$

$$\check{G}_{\mu\nu} = -s_\mu^* s_\nu \check{V}_{\mu\bar{\mu}\nu\bar{\nu}}. \quad (4.16b)$$

The two-body matrix elements in the canonical basis are defined as usual:

$$\check{V}_{\mu\nu\mu'\nu'} = \int d^3\mathbf{r}_1 d^3\mathbf{r}_2 d^3\mathbf{r}'_1 d^3\mathbf{r}'_2 \sum_{\sigma_1\sigma_2\sigma'_1\sigma'_2} V(\mathbf{r}_1\sigma_1, \mathbf{r}_2\sigma_2; \mathbf{r}'_1\sigma'_1, \mathbf{r}'_2\sigma'_2) \check{\psi}_\mu^*(\mathbf{r}_1\sigma_1) \check{\psi}_\nu^*(\mathbf{r}_2\sigma_2) \check{\psi}_{\mu'}(\mathbf{r}'_1\sigma'_1) \check{\psi}_{\nu'}(\mathbf{r}'_2\sigma'_2). \quad (4.17)$$

Since we include in $V(\mathbf{r}_1\sigma_1, \mathbf{r}_2\sigma_2; \mathbf{r}'_1\sigma'_1, \mathbf{r}'_2\sigma'_2)$ the exchange term, the matrix $V_{\mu\nu\mu'\nu'}$ is anti-symmetric in $\mu\nu$ and in $\mu'\nu'$. Due to the hermiticity and the time-reversal symmetry of the interaction, matrices $\check{F}_{\mu\nu}$ and $\check{G}_{\mu\nu}$ obey the following symmetry relations,

$$\check{F}_{\mu\nu} = \check{F}_{\mu\nu}^* = \check{F}_{\nu\mu} = \check{F}_{\mu\bar{\nu}} = \check{F}_{\bar{\mu}\nu}, \quad (4.18a)$$

$$\check{G}_{\mu\nu} = \check{G}_{\mu\nu}^* = \check{G}_{\nu\mu} = \check{G}_{\mu\bar{\nu}} = \check{G}_{\bar{\mu}\nu}. \quad (4.18b)$$

The matrix \check{F} is defined by different matrix elements of the interaction than the matrix \check{G} . Namely, the matrix element $\check{F}_{\mu\nu}$ represents a “diagonal” scattering of pairs of states $\mu\nu \rightarrow \mu\nu$ (or $\mu\bar{\nu} \rightarrow \mu\bar{\nu}$). This type of scattering concerns *all* pairs of states. The resulting contributions to the energy, Eq. (4.15), involve the occupation probabilities of the single-particle states constituting each pair. On the other hand, the matrix elements $\check{G}_{\mu\nu}$ represent a “non-diagonal” scattering of pairs of *time-reversed* states $\nu\bar{\nu} \rightarrow \mu\bar{\mu}$. This scattering concerns only a very special subset of all pairs.

In principle, an effective interaction should describe both channels of interaction at the same time. This is, for example, the case for the Gogny interaction [57] and for the Skyrme SkP interaction [52]. However, the fact that both channels of interaction play a different role in the HFB theory allows the use of different forms of interaction to model the p-h and p-p channels. Such an approach is additionally motivated by the fact that the interaction in the p-h channel, which defines, e.g., the saturation properties, is much better known than the p-p interaction. Moreover, the p-h channel provides a two-orders-of-magnitude larger interaction energy.

Since the canonical-basis wave functions $\check{\psi}(\mathbf{r}\sigma)$ are all localized, it is instructive to consider the HFB equations in this particular basis. They read:

$$(\check{h} - \lambda)_{\mu\nu} \eta_{\mu\nu} + \check{h}_{\mu\nu} \xi_{\mu\nu} = 0, \quad (4.19a)$$

$$(\check{h} - \lambda)_{\mu\nu} \xi_{\mu\nu} - \check{h}_{\mu\nu} \eta_{\mu\nu} = \check{E}_{\mu\nu}, \quad (4.19b)$$

where

$$\eta_{\mu\nu} := u_\mu v_\nu + u_\nu v_\mu, \quad (4.20a)$$

$$\xi_{\mu\nu} := u_\mu u_\nu - v_\nu v_\mu. \quad (4.20b)$$

Equation (4.19a) is equivalent to the variational condition that the HFB energy is minimized, while Eq. (4.19b) defines the energy matrix $\check{E}_{\mu\nu}$. (The matrix $\check{E}_{\mu\nu}$ represents the

HFB Hamiltonian in the canonical basis.) Since for every pair of indices $\mu\nu$ it holds that $(\eta_{\mu\nu})^2 + (\xi_{\mu\nu})^2 = 1$, Eqs. (4.19) can be written as

$$(\check{h} - \lambda)_{\mu\nu} = \check{E}_{\mu\nu} \xi_{\mu\nu}, \quad (4.21a)$$

$$-\check{h}_{\mu\nu} = \check{E}_{\mu\nu} \eta_{\mu\nu}. \quad (4.21b)$$

The occupation probabilities v_μ are solely determined by the diagonal matrix elements of the p-h and p-p Hamiltonians,

$$\epsilon_\mu := \check{h}_{\mu\mu}, \quad (4.22a)$$

$$\Delta_\mu := -\check{h}_{\mu\mu}, \quad (4.22b)$$

and the result is

$$v_\mu = \text{sign}(\Delta_\mu) \sqrt{\frac{1}{2} - \frac{\epsilon_\mu - \lambda}{2E_\mu}}, \quad (4.23a)$$

$$u_\mu = \sqrt{\frac{1}{2} + \frac{\epsilon_\mu - \lambda}{2E_\mu}}, \quad (4.23b)$$

where E_μ are the diagonal matrix elements of the matrix $\check{E}_{\mu\nu}$:

$$E_\mu := \check{E}_{\mu\mu} = \sqrt{(\epsilon_\mu - \lambda)^2 + \Delta_\mu^2}. \quad (4.24)$$

In this representation, the average pairing gap (4.6) is given by the average value of Δ_μ in the occupied states,

$$\langle \Delta \rangle = \frac{\sum_\mu \Delta_\mu v_\mu^2}{\sum_\mu v_\mu^2} = \frac{1}{N^\tau} \sum_\mu \Delta_\mu v_\mu^2. \quad (4.25)$$

Equations (4.23) and (4.24) misleadingly resemble those of the simple BCS theory [24]. However, in the HFB theory, ϵ_μ is not the single-particle energy (i.e., the eigenvalue of h) but the diagonal matrix element of h in the canonical basis. Similarly, Δ_μ does not represent the pairing gap in the state $\check{\psi}_\mu$, and E_μ is not the quasiparticle energy E . However, since these quantities define the occupation probabilities, they play a very important role in an interpretation of the HFB results, and many intuitive, quantitative, and useful features of the BCS theory can be reinterpreted in terms of the canonical representation (cf. Sec. V C).

In particular, the average values of single-particle p-h and p-p Hamiltonians fulfill the following self-consistency equations:

$$\epsilon_\mu = T_{\mu\mu} + \frac{1}{2} \sum_\nu \check{F}_{\mu\nu} \left(1 - \frac{\epsilon_\nu - \lambda}{E_\nu} \right), \quad (4.26a)$$

$$\Delta_\mu = \frac{1}{4} \sum_\nu \check{G}_{\mu\nu} \frac{\Delta_\nu}{E_\nu}. \quad (4.26b)$$

For a given interaction $\check{F}_{\mu\nu}$ and $\check{G}_{\mu\nu}$, Eqs. (4.26) represent a set of nonlinear equations which determine ϵ_μ and Δ_μ . Equations for ϵ_μ (4.26a) and for Δ_μ (4.26b) are coupled by the values

of E_ν (4.24), which depend on both ϵ_μ and Δ_μ . However, it is clear that the interaction in the p-h channel mainly influences the values of ϵ_μ , while that in the p-p channel – Δ_μ .

Unfortunately, Eqs. (4.26) cannot replace the original HFB equations, because they require the knowledge of the canonical basis to determine the $\check{F}_{\mu\nu}$ and $\check{G}_{\mu\nu}$ matrices. The only way to determine the canonical basis is to solve the original HFB equation (4.8), and then to diagonalize the density matrix (4.9a). Moreover, solving Eqs. (4.26) ensures that only the $\mu=\nu$ subset of variational equations (4.19a) is met, the minimum of energy being obtained by solving the whole set (i.e., for all indices μ and ν).

The diagonalization of the energy matrix $\check{E}_{\mu\nu}$ gives the spectrum of HFB eigenenergies, E_n :

$$\sum_\nu \check{E}_{\mu\nu} \mathcal{U}_{n\nu} = E_n \mathcal{U}_{n\mu}. \quad (4.27)$$

The matrix $\mathcal{U}_{n\mu}$ represents the unitary transformation from the canonical to the quasiparticle basis [24]. Its matrix elements provide the link between the quasiparticle energies E_n and the diagonal matrix elements E_μ which define the occupation probabilities, i.e.,

$$E_\mu = \sum_n E_n |\mathcal{U}_{n\mu}|^2. \quad (4.28)$$

V. COUPLING TO THE POSITIVE-ENERGY STATES

For weakly bound nuclei one may expect that the particle continuum influences the ground-state properties in a significant way. As discussed in Sec. IV C 2, the phase space corresponding to positive single-particle energies should not be confused with the continuum of scattering states which asymptotically behave as plane waves, and are significant for genuine scattering phenomena.

A. Boundary conditions

Properties of the continuum scattering states are intuitively well understood in terms of unpaired single-particle orbits. Shown in Fig. 9 are the self-consistent HF+SkP neutron single-particle energies in ^{150}Sn , $\epsilon_{nlj}^{\text{HF}}$, as functions of the radius R_{box} of the spherical box in which the HF equations are solved. It is assumed that the following boundary condition holds for all single-particle wave functions:

$$\psi_\mu(R_{\text{box}}) = 0. \quad (5.1)$$

For bound single-particle states, $\epsilon_{nlj}^{\text{HF}} < 0$, the effect of increasing R_{box} beyond 10 fm is insignificant. As seen in Fig. 9, the energies of the least bound $3p$, $2f$, $1h_{9/2}$, and $1i_{13/2}$ states, which form the $82 \leq N \leq 126$ shell, are independent of R_{box} .

The boundary condition (5.1) leads to a discretization of the continuum by selecting only those states which have a node at $r=R_{\text{box}}$. When R_{box} increases, the density of the low-energy continuum states increases as R_{box}^3 . This effect is very well visible in Fig. 9. Among those states whose energies decrease with R_{box} , one may easily distinguish some quasi-bound

states, which have energies fairly independent of R_{box} . In Fig. 9 these are the high- ℓ states $i_{11/2}$, $j_{13/2}$, $j_{15/2}$, and $k_{15/2}$. However, at some values of R_{box} they are crossed by, and they interact with, the real continuum states (plane waves) of the same quantum numbers, and their precise determination is, in practice, very difficult.

A solution of the HFB equation (4.13) in the spherical box amounts to using the analogous boundary conditions,

$$\phi_1(E, R_{\text{box}}) = \phi_2(E, R_{\text{box}}) = 0, \quad (5.2)$$

for both components of the HFB wave function. As a result, the quasiparticle continuum of states with $|E| > -\lambda$ is discretized and becomes more and more dense with increasing R_{box} . However, as discussed in Sec. IV C, the density matrix depends only on the localized (lower) components of the quasiparticle wave functions and, therefore, is very well stable with increasing R_{box} . By the same token, the properties of the canonical-basis states, which are the eigenstates of the density matrix, are also asymptotically stable. Of course, the bigger the value of R_{box} , the larger is the numerical effort required to solve the HFB equations. Consequently, it is important to optimize the value of R_{box} ; i.e., to use the smallest box sizes which reproduce all interesting physical properties of the system.

Apart from ours, there are also other possible approaches to solving the HFB eigenproblem; in particular: (i) the diagonalization in the large harmonic oscillator basis, and (ii) the two-step diagonalization. Scheme (i) has been used, e.g., in the HFB+Gogny calculations or in the deformed HFB+SkP calculations of Ref. [79]. Its limitations, due to the incorrect asymptotics, are discussed in Sec. V G below. In method (ii) one first solves the HF problem and then diagonalizes the full HFB Hamiltonian in the HF basis. Such a strategy has been suggested in Ref. [42] and recently adopted in Ref. [81].

B. Canonical single-particle spectrum

As discussed in Sec. IV D, quantities which determine the p-h properties of the system are the canonical energies ϵ_μ [Eq. (4.22a)]. The neutron canonical energies in ^{150}Sn are shown in Fig. 10 as functions of the box size R_{box} . In this figure, the single-particle index μ is represented by the spherical quantum numbers $n\ell j$; only the states with occupation probabilities $v_{n\ell j}^2 > 0.0001$ are presented. The canonical states belonging to the shell $82 \leq N \leq 126$ have negative $\epsilon_{n\ell j}$'s, and they are very close to the HF single-particle energies displayed in Fig. 9. They do not depend on the values of R_{box} for $R_{\text{box}} > 10$ fm.

At positive values of $\epsilon_{n\ell j}$, there are several orbitals which do not depend on the box size even at $R_{\text{box}} < 15$ fm. These states correspond to the high- ℓ quasibound states $i_{11/2}$, $j_{13/2}$, $j_{15/2}$, and $k_{15/2}$, already identified in the HF spectrum of Fig. 9. The values of $\epsilon_{n\ell j}$ for these states are only slightly higher than the corresponding values of $\epsilon_{n\ell j}^{\text{HF}}$. However, these quasibound canonical-basis states are not accompanied by the sea of plane-wave scattering states (cf. the $j_{13/2}$, and the $k_{15/2}$ states in Figs. 9 and 10). One can thus say that the canonical-basis states represent the quasibound states well decoupled from the scattering continuum.

Many other canonical-basis states, especially those with low orbital angular momenta ℓ , significantly depend on the box size up to about $R_{\text{box}} = 18$ fm, and then stabilize. Therefore, in all subsequent calculations we use a “safe” value of $R_{\text{box}} = 20$ fm, unless stated otherwise.

Above 20 MeV there appear states with canonical energies fluctuating with R_{box} . These states have very small occupation probabilities close to the limiting value of $v_{n\ell j}^2=0.0001$, and their determination as eigenstates of the density matrix is prone to large numerical uncertainties (see Sec. IV C 2). One should note that the physical observables are calculated directly by using the HFB density matrices, and the above numerical uncertainties do not affect the results obtained within the HFB theory.

As pointed out in Ref. [77], the canonical spectrum presented in Fig. 10 can be used to analyze the shell effects far from stability. In particular, the size of the $N=126$ gap is very small (a 2 MeV gap between the $1i_{13/2}$ and $4s_{1/2}$ states), and hence it cannot yield any pronounced shell effect (seen, e.g., in the behavior of the two-neutron separation energies, Sec. VI C). This shell-gap quenching is not a result of a too small value of the spin-orbit splitting. Indeed, a larger spin-orbit strength would push the $1i_{13/2}$ level down in energy, without affecting the size of the $N=126$ shell gap (several negative-parity states are nearby). The $N=126$ gap, which is equal to about 4 MeV at $R_{\text{box}}=10$ fm, closes up with increasing R_{box} due to the several low- ℓ states whose energies steadily decrease. This effect can be attributed to the pairing-induced coupling with the positive-energy states (see Sec. V G).

In the energy window between 0 and 20 MeV, the density of single-particle canonical energies is fairly uniform and no pronounced shell effects are visible. Since the Fermi energy must stay at negative values, this region of the phase space cannot be reached. However, one may say that the influence of the positive-energy spectrum on the bound states (had we analyzed it in terms of, e.g., the Strutinsky averaging) is characterized by a rather structureless distribution of states. Above 20 MeV, the occupation probabilities rapidly decrease (cf. Table I), and this part of the phase space can safely be disregarded, provided one stays in the canonical basis.

C. Single-quasiparticle spectrum

The eigenvalues of the HFB equation (4.13) (single-quasiparticle energies) carry information on the elementary modes of the system. The lowest single-quasineutron energies $E_{n\ell j}^{\text{HFB}}$ in tin isotopes between $N=50$ and $N=126$ are shown in Fig. 11 (top panel). Apart from the magic shell gaps at $N=50$ and $N=82$, where the single-quasiparticle energies exhibit sudden jumps, they depend rather smoothly on neutron number. For a given orbital $n\ell j$, the minimum of $E_{n\ell j}^{\text{HFB}}$ is attained in the isotope where the corresponding single-particle state is closest to the Fermi energy. Hence, from Fig. 11 one can infer the order of single-particle energies in the beginning of the $50 \leq N \leq 82$ shell as $2d_{5/2}$, $3s_{1/2}$, $2d_{3/2}$, $1g_{7/2}$, and $1h_{11/2}$. Similarly, the predicted order at the bottom of the next major shell is $2f_{7/2}$, $3p_{3/2}$, $3p_{1/2}$, $2f_{5/2}$, $1h_{9/2}$, and $1i_{13/2}$. The order of spherical single-particle states does vary with N . For instance, according to the HFB+SkP calculations of Fig. 11, the $1g_{7/2}$ shell never becomes lowest in energy, as it should have done, had the single-particle energies been N -independent.

Noteworthy is the fact that, due to the strong interaction with the low- ℓ continuum (cf. Sec. V B), the $4s_{1/2}$ excitation becomes lowest at $N>114$. Above the $4s_{1/2}$ state there appear several quasiparticle states with excitation energies rapidly decreasing with N . These orbitals represent the low-energy continuum states. They are very close in energy, exhibit small spin-orbit splitting, and the lowest of them are the low- ℓ states: $4p_{1/2}$, $4p_{3/2}$, $3d_{3/2}$, and $3d_{5/2}$. All these features are characteristic of the continuum states [82]. Still higher in

energy, one may distinguish a similar doublet of the $3f_{5/2}$ and $3f_{7/2}$ states, as well as the $2g_{9/2}$ state which represents a high- ℓ resonance.

The bottom panel of Fig. 11 shows similar results for the BCS-like canonical energies E_μ defined in Eq. (4.24), and denoted here by $E_{n\ell j}^{\text{can}}$. A comparison between $E_{n\ell j}^{\text{HFB}}$ and $E_{n\ell j}^{\text{can}}$ illustrates the fact that the *lowest* elementary excitations of the nucleus are equally well described by both these quantities. Indeed, a general pattern and, in most cases, also the values of $E_{n\ell j}^{\text{HFB}}$ and $E_{n\ell j}^{\text{can}}$ are very similar. The differences mainly concern the $s_{1/2}$ states, and also the low- ℓ states in the continuum, which in the canonical representation appear higher in energy (see Table I for the direct comparison for $s_{1/2}$ states). On the other hand, the position of the high- ℓ $2g_{9/2}$ resonance is almost identical in both representations. Such a similarity supports the supposition (Ref. [77] and Sec. V B) that the canonical single-particle energies, which are the main ingredients of $E_{n\ell j}^{\text{can}}$, constitute a fair representation of single-particle and single-quasiparticle properties of the system.

D. Relation between canonical and single-quasiparticle wave functions

As discussed in Sec. IIIB, the canonical states constitute a basis in which the independent-quasiparticle state $|\Psi\rangle$ has the form of a product of correlated pairs [Eq. (3.16)]. Therefore, these states can be considered as fundamental building blocks describing the pairing correlations in a many-fermion system. On the other hand, the canonical states are determined by a solution of the HFB equation – the single-quasiparticle states.

Since the canonical states constitute an orthonormal ensemble, the lower and upper HFB components can be expanded as

$$\phi_1(E_n, \mathbf{r}\sigma) = \sum_{\mu} \mathcal{A}_{n\mu}^{(1)} \check{\psi}_{\mu}(\mathbf{r}\sigma), \quad (5.3a)$$

$$\phi_2(E_n, \mathbf{r}\sigma) = \sum_{\mu} \mathcal{A}_{n\mu}^{(2)} \check{\psi}_{\mu}(\mathbf{r}\sigma), \quad (5.3b)$$

where

$$\mathcal{A}_{n\mu}^{(i)} \equiv \int d^3\mathbf{r} \sum_{\sigma} \check{\psi}_{\mu}^*(\mathbf{r}\sigma) \phi_i(E_n, \mathbf{r}\sigma) \quad (i = 1, 2) \quad (5.4)$$

are the associated overlaps. In order to find the relation between $\mathcal{A}_{n\mu}^{(1)}$ and $\mathcal{A}_{n\mu}^{(2)}$ one can employ Eqs. (3.31) and (4.9) for the HFB densities. This gives the canonical wave functions expressed as linear combinations of the *lower* HFB components:

$$v_{\mu}^2 \check{\psi}_{\mu}(\mathbf{r}\sigma) = \sum_n \mathcal{A}_{n\mu}^{(2)} \phi_2(E_n, \mathbf{r}\sigma), \quad (5.5a)$$

$$-u_{\mu} v_{\mu} \check{\psi}_{\mu}(\mathbf{r}\sigma) = \sum_n \mathcal{A}_{n\mu}^{(1)} \phi_2(E_n, \mathbf{r}\sigma). \quad (5.5b)$$

One should note that the expansions (5.5) are valid regardless of the fact that the lower components $\phi_2(E_n, \mathbf{r}\sigma)$ *do not constitute* an orthogonal ensemble of wave functions. By multiplying both sides of Eqs. (5.5a) and (5.5b) with $\check{\psi}_{\nu}^*(\mathbf{r}\sigma)$ and taking the scalar product, one arrives at the orthogonality relations:

$$\sum_n \mathcal{A}_{n\mu}^{(2)} \mathcal{A}_{n\nu}^{(2)*} = v_\mu^2 \delta_{\mu\nu}, \quad (5.6a)$$

$$\sum_n \mathcal{A}_{n\mu}^{(1)} \mathcal{A}_{n\nu}^{(2)*} = -u_\mu v_\mu \delta_{\mu\nu}. \quad (5.6b)$$

The above identities express the fact, that both $\mathcal{A}_{n\mu}^{(2)}$ and $\mathcal{A}_{n\mu}^{(1)}$ are related to the transformation matrix $\mathcal{U}_{n\nu}$ defined in Eq. (4.27):

$$\mathcal{A}_{n\mu}^{(2)} = v_\mu \mathcal{U}_{n\mu}, \quad \mathcal{A}_{n\mu}^{(1)} = -u_\mu \mathcal{U}_{n\mu}, \quad (5.7)$$

and Eqs. (5.6) reflect the unitarity of $\mathcal{U}_{n\nu}$. Equations (5.7) can be easily derived by inserting expansions (5.3) into the HFB equation (4.8), and then expressing the matrix $E_{\mu\nu}$ (4.19b) in its eigensystem (4.27).

It is instructive to express the upper HFB component in a form similar to that of Eq. (5.3b):

$$\phi_1(E_n, \mathbf{r}\sigma) = - \sum_\mu \frac{u_\mu}{v_\mu} \mathcal{A}_{n\mu}^{(2)} \check{\psi}_\mu(\mathbf{r}\sigma). \quad (5.8)$$

For $E_n > -\lambda$, the upper component $\phi_1(E_n, \mathbf{r}\sigma)$ is the scattering wave function. It can be formally expanded in the *localized* canonical wave functions according to Eq. (5.8), but the main contribution comes from the particle-like states with very small values of v_μ^2 . Hence, this relation is not too useful in practical applications.

E. Spectral distribution for the canonical-basis wave functions

In order to discuss the importance of the particle continuum on the structure of canonical states, it is interesting to see how a given canonical state is distributed among the single-quasiparticle states. For this, it is convenient to rewrite Eq. (5.5a) in the following way:

$$\check{\psi}_\mu(\mathbf{r}\sigma) = \sum_{0 < E_n < E_{\max}} \frac{\mathcal{S}_{n\mu}}{\sqrt{N_n}} \phi_2(E_n, \mathbf{r}\sigma). \quad (5.9)$$

The spectral amplitudes $\mathcal{S}_{n\mu}$ define the distribution of the canonical states among the single-quasiparticle states. It is important to recall at this point that the sum in Eq. (5.9) represents in fact the discrete ($E_n < -\lambda$) states and the discretized ($E_n > -\lambda$) continuum states, i.e.,

$$\begin{aligned} \check{\psi}_\mu(\mathbf{r}\sigma) = & \sum_{0 < E_n < -\lambda} \frac{\mathcal{S}_{n\mu}}{\sqrt{N_n}} \phi_2(E_n, \mathbf{r}\sigma) + \\ & \int_{-\lambda}^{\infty} dn(E) \frac{\mathcal{S}_{E,\mu}}{\sqrt{N_E}} \phi_2(E, \mathbf{r}\sigma), \end{aligned} \quad (5.10)$$

with the spectral amplitudes $\mathcal{S}_{n\mu}$ and $\mathcal{S}_{E,\mu}$ pertaining to the discrete and continuous HFB spectrum, respectively.

The spectral amplitudes can be expressed in terms of matrices $\mathcal{A}_{n\mu}^{(2)}$ or $\mathcal{U}_{n\mu}$ introduced in Sec. VD:

$$\mathcal{S}_{n\mu} = \frac{\sqrt{N_n}}{v_\mu^2} \mathcal{A}_{n\mu}^{(2)} = \frac{\sqrt{N_n}}{v_\mu} \mathcal{U}_{n\mu}. \quad (5.11)$$

We have included in $\mathcal{S}_{n\mu}$ the norms N_n of the lower components, Eq. (4.11). In this way, the values of spectral amplitudes measure the influence of quasiparticle states irrespective of the overall magnitude of their lower components.

Before discussing the properties of the spectral amplitudes, let us write down the two sum rules:

$$1 = \sum_{\mu} |\mathcal{S}_{n\mu}|^2 \frac{v_{\mu}^2}{N_n} = \sum_n |\mathcal{S}_{n\mu}|^2 \frac{v_{\mu}^2}{N_n}, \quad (5.12)$$

$$1 = \sum_{\mu} |\mathcal{S}_{n\mu}|^2 \frac{v_{\mu}^4}{N_n^2}. \quad (5.13)$$

The first two sum rules, Eq. (5.12), come from the unitarity of $\mathcal{U}_{n\mu}$. The last one, Eq. (5.13), expresses the condition defining the norm of the lower HFB component.

In Fig. 12 are shown the spectral amplitudes for the $s_{1/2}$ canonical states in ^{120}Sn (cf. Secs. IV C 1 and IV C 2). The phases of the single-quasiparticle wave functions have been fixed in such a way that all the amplitudes $\mathcal{S}_{n\mu}$ for $\mu=1$ are positive (some of these amplitudes are too small to be displayed in the figure). This defines the relative phases of the spectral amplitudes for $\mu>1$. Then, the positive and negative amplitudes are in Fig. 12 shown by bars hashed in opposite directions. Results shown in this figure pertain to the same single-quasiparticle and canonical states as those shown in Figs. 6 and 7, respectively, and in Table I.

The lowest panel in Fig. 12 shows that the $1s_{1/2}$ canonical state ($\mu=1$) is composed mainly of two components corresponding to the two deep-hole quasiparticles at $E_8=31.64$ MeV and $E_5=17.60$ MeV. Similarly, the $\mu=2$ and $\mu=3$ canonical states are mixtures of the $E_5=17.60$ MeV and $E_1=1.54$ MeV quasiparticles. For all three of these canonical states, the diagonal amplitudes dominate.

Another pattern appears for the positive-energy canonical states; i.e., for $\mu=4$ and $\mu=5$. These two canonical states contain large components of the hole-like quasiparticles at $E_5=17.60$ MeV and $E_1=1.54$ MeV, but in addition, they also acquire large components of the particle-type quasiparticles belonging to the continuum. These continuum components are centered around 15 and 20 MeV for $\mu=4$ and $\mu=5$, respectively. This illustrates the fact that a correct description of the positive-energy canonical states requires solving the HFB equation to rather high energies. The widths of the corresponding distributions are rather large, which indicates that there is not a single resonance in the particle continuum which would alone describe the high-energy $s_{1/2}$ canonical states. This can be well understood by recalling that the $\ell=0$ resonances have usually very large widths.

For the drip-line nucleus ^{150}Sn , the spectral $s_{1/2}$ amplitudes are shown in Fig. 13. Similarly to the case of ^{120}Sn , the three lowest canonical states for $\mu=1, 2$, and 3 are mainly composed of the three hole-like quasiparticles at $E_9=34.27$, $E_7=22.12$, and $E_3=7.24$ MeV with dominating diagonal amplitudes. On the other hand, the low-lying positive-energy canonical $\mu=4$ state has large and almost equal components coming from the particle-like quasiparticles at $E_1=2.40$, $E_2=4.84$, and $E_4=8.93$ MeV. The following $\mu=5$ canonical state has dominant amplitudes from the hole-like and particle-like quasiparticles at $E_3=7.24$ and 8.93 MeV, respectively. One should note that the $\mu=4$ and $\mu=5$ canonical $s_{1/2}$ states in

^{150}Sn have rather large occupation factors as compared to those in ^{120}Sn . Both of them require including the single-quasiparticle states *at least* up to 10 MeV. The following $\mu=6$ state (not shown in the figure) has the occupation probability of $v_6^2=0.0003$ and the spectral amplitudes extending up to 25 MeV.

The spectral amplitudes for the $f_{7/2}$ states in ^{120}Sn and ^{150}Sn are shown in Figs. 14 and 15, respectively. An interesting situation appears in ^{120}Sn where two quasiparticles, one of the particle type and another one of the hole type, have rather similar single-quasiparticle energies of 17.63 and 18.97 MeV. As a result, the lowest canonical state ($\mu=1$) acquires a substantial particle-type quasiparticle component, while both quasiparticles contribute almost equally to the $\mu=3$ canonical state. In ^{150}Sn , the positive-energy $f_{7/2}$ canonical states ($\mu=3$ and 4) have large amplitudes from the hole-like quasiparticles (contributing almost exclusively to the structure of the negative-energy canonical states with $\mu=1$ ($1f_{7/2}$) and $\mu=2$ ($2f_{7/2}$)), as well as from a wide distribution of several particle-type quasiparticles extending up to 20 MeV.

The spectral amplitudes allow also for a determination of the asymptotic properties of canonical states. (See Ref. [69] for a discussion of the asymptotic properties of natural orbits.) The lower components $\phi_2(E_n, \mathbf{r}\sigma)$ behave asymptotically as $\exp(-r\sqrt{2m(E_n - \lambda)/\hbar^2})$ [33,52]. Therefore, as seen from Eq. (5.10), the asymptotic properties of canonical states are governed by the lowest discrete quasiparticle, provided the corresponding spectral amplitude, $\mathcal{S}_{1\mu}$, is not equal to zero. However, if such a spectral amplitude is non-zero but very small, the corresponding asymptotic behavior will be attained only at very large distances. In practice, the lowest discrete quasiparticle dominates the asymptotic behavior only if the corresponding spectral amplitude has a significantly large value. For the $s_{1/2}$ states in ^{120}Sn (Fig. 12) such a situation occurs for the canonical states with $\mu=2-5$. On the other hand, since the value of $|\mathcal{S}_{1,1}|$ is very small, the asymptotic behavior of the $\mu=1$ canonical state is dominated by the hole-like quasiparticle at $E_5=17.60$ MeV. A similar situation occurs for the $f_{7/2}$ states in ^{120}Sn . Namely, only for the $\mu=2$ canonical state the asymptotic behavior is determined by the lowest discrete quasiparticle.

An entirely different property can occur in drip-line nuclei, where the Fermi energy is close to zero and there may be no quasiparticle excitations in the discrete spectrum between 0 and $-\lambda$. In such a situation, shown in Figs. 13 and 15, the canonical states are represented by superpositions of lower quasiparticle components belonging to the particle continuum. Consequently, it is the integral over the lowest continuum quasiparticle states just above the $E > -\lambda$ threshold that determines the asymptotic properties of the canonical states. In other words, the profile of the level density, $dn(E)/dE$, around $E = -\lambda$ becomes a crucial factor. Good examples of a very strong coupling to the particle continuum are the $\mu=4$ and 5 canonical $s_{1/2}$ and $f_{7/2}$ states in ^{150}Sn , where the quasiparticle strength is distributed in a very wide energy interval ranging from 1.5 to 20 MeV. On the other hand, the two lowest canonical $f_{7/2}$ states in ^{150}Sn can be associated with the two quasiparticle excitations well localized in energy (see Fig. 15) and their asymptotics is governed by the energy of the lowest quasiparticle.

An analysis of the spectral distribution, analogous the one presented above, has recently been performed [73] for the natural orbits in ^{16}O determined within the Green's function method using the NN interaction. This method accounts for a much more general class of correlations as compared to the HFB correlations of the pairing type studied here. However,

the general features of the spectral distributions remain essentially the same. Namely, the low-occupation-number natural orbits are determined mostly through high-energy continuum contributions, and large box sizes (15–20 fm) and large single-particle bases (20 states per ℓj -block) have to be used to stabilize the solutions. This is so even if the studied nucleus (^{16}O) is β -stable, well-bound, and light; one can expect that for drip-line nuclei the aforementioned features can only be more pronounced.

F. Asymptotic properties

In the limit of weak binding, radial dimensions of atomic nuclei increase and it becomes exceedingly important to control the radial asymptotics of many-body wave functions, not only in reaction studies but also in nuclear structure applications. Figure 16 displays the radial dependence of the neutron density $\rho(r)$ in ^{150}Sn calculated with the values of R_{box} between 10 and 30 fm. It is seen that, for every value of R_{box} , $\rho(r)$ follows its asymptotic behavior up to about $R_{\text{box}} - 3$ fm and then falls down to zero as a result of the boundary conditions (5.2). That is, these boundary conditions affect the density only in a narrow spherical layer of the thickness equal to about 3 fm, while inside this layer $\rho(r)$ behaves independently of the value of R_{box} . Analogous results for the pairing density $\tilde{\rho}(r)$ are shown in Fig. 17.

At very large distances the asymptotic behavior of the particle density is governed by the square of the lower component of the single-quasiparticle wave function corresponding to the lowest quasiparticle energy E_{min} . Similarly, the asymptotic behavior of the pairing density $\tilde{\rho}(r)$ is determined by the product of the upper and the lower components of quasiparticle E_{min} . Using the asymptotic properties of the HFB wave functions derived in [33,52], one obtains:

$$\rho(r) \xrightarrow{\text{large } r} \sim \frac{\exp(-\chi r)}{r^2} \quad ; \quad \chi = 2\kappa_2, \quad (5.14a)$$

$$\tilde{\rho}(r) \xrightarrow{\text{large } r} \sim \frac{\exp(-\tilde{\chi} r)}{r^2} \quad ; \quad \tilde{\chi} = \kappa_1 + \kappa_2, \quad (5.14b)$$

where

$$\kappa_1 = \sqrt{\frac{2m(-E_{\text{min}} - \lambda)}{\hbar^2}} \quad , \quad \kappa_2 = \sqrt{\frac{2m(E_{\text{min}} - \lambda)}{\hbar^2}}. \quad (5.15)$$

In the considered example of ^{150}Sn the calculated values are $\lambda = -1.46$ MeV and $E_{\text{min}} = 1.07$ MeV (a $p_{1/2}$ state). Consequently, $\chi \simeq 0.70 \text{ fm}^{-1}$ and $\tilde{\chi} \simeq 0.49 \text{ fm}^{-1}$. In Figs. 16 and 17 the asymptotic dependencies given by Eq. (5.14) are shown as shaded lines. One can see that for $\rho(r)$ the asymptotic regime is reached only at distances as large as 25 fm, which means that the contributions from other quasiparticle states, and/or from the next-to-leading-order terms in the Hankel functions, still influence the particle density at rather large values of r . Interestingly, the pairing density approaches the asymptotic limit already at $r \sim 10$ fm.

A rough estimate of χ and $\tilde{\chi}$ can be obtained by substituting the value of a typical pairing gap ($\Delta = 1$ MeV) for the lowest quasiparticle energy E_{min} . For stable nuclei ($\lambda \simeq -8$ MeV) one obtains $\chi \simeq 1.32 \text{ fm}^{-1}$, while for the one-neutron drip nuclei, defined by a vanishing separation

energy, $S_n \simeq \Delta + \lambda \simeq 0$, the result is $\chi \simeq 0.62 \text{ fm}^{-1}$. This difference illustrates the increase in the spatial extension of the *particle* densities when going towards the neutron drip line. On the other hand, for the *pairing* densities the corresponding numbers are $\tilde{\chi} \simeq 1.24 \text{ fm}^{-1}$ and $\tilde{\chi} = \chi/2 \simeq 0.31 \text{ fm}^{-1}$. Therefore, in stable nuclei both types of densities have rather similar asymptotic behavior, while in drip-line nuclei the pairing densities have much longer tails.

In this context, it is instructive to recall the discussion from Sec. III C regarding the probabilistic interpretation of the HFB densities. The probability $\mathcal{P}_1(x)$ ($\mathcal{P}_2(x)$) of finding a particle or a pair of particles at $r=x$ is proportional to $\rho(x)$ or $\rho^2(x) + \tilde{\rho}^2(x)$, respectively. Consequently, in stable nuclei $\mathcal{P}_2(x)$ decays much faster than $\mathcal{P}_1(x)$ at large distances. This is not true for drip-line nuclei, where the asymptotics of $\mathcal{P}_1(x)$ and $\mathcal{P}_2(x)$ is the same.

As discussed above, static pairing correlations can influence dramatically the asymptotic behavior of density distributions in drip-line nuclei. In addition, a significant modification of the density tails comes from the dynamical coupling to collective modes through the particle continuum. Such a coupling can be treated in terms of the continuum QRPA and has been shown to be very important for light systems [83,84]. An analysis of the asymptotic behavior of the particle density $\rho(r)$ has recently been performed [85] by finding the *exact* solutions for weakly bound two particles interacting through a contact force. In that study, the role of one-particle resonant states on the density asymptotics has been discussed.

G. Pairing coupling to positive-energy states

As illustrated in Sec. V A, the density of the scattering continuum states increases with R_{box} . In the limit of very large values of R_{box} , the set of discretized continuum states can be considered as a fair approximation of the real continuum, and the sums over the positive-energy states can correctly represent integrals over the continuous energy variable. Therefore, we may consider this limit in order to study the dynamical coupling between the bound single-particle states and the positive-energy states. In the language of pairing correlations, one may think of this coupling in terms of a virtual scattering of pairs of fermions from the bound states to positive-energy states, and back. Such a pair scattering gives rise to the additional pairing energy to the ground-state energy.

To illustrate the stability of results with increasing box size, in Fig. 18 we show the neutron p-p potentials $\tilde{U}(r)$ in ^{150}Sn and ^{172}Sn calculated in the HFB+SkP model for several values of R_{box} . In these two nuclei, the values of $\tilde{U}(r)$ do not change when R_{box} is larger than 20 and 22 fm, respectively, but at smaller values of R_{box} , one observes significant variations. A rather unexpected result of this analysis is that the overall magnitude of pairing correlations, represented by the average pairing gap $\langle \Delta \rangle$, *decreases* with increasing R_{box} . This occurs in spite of the fact that the actual density of scattering states dramatically *increases* with increasing R_{box} .

This effect can be understood by noting that the pairing correlations produced by a density-dependent p-p interaction (and hence for the SkP force used here) are concentrated at the nuclear surface; i.e., at a fixed location in space. For small values of R_{box} , the boundary conditions (5.2) have a tendency to push the continuum wave functions towards smaller distances, and into the surface region. This increases the magnitude of pairing correlations. On the other hand, with increasing R_{box} , the scattering states spread out uniformly outside the nucleus and effectively leave the surface region. Hence $\langle \Delta \rangle$ decreases.

As a consequence, with increasing R_{box} the self-consistent attractive pairing potential $\tilde{U}(r)$ decreases in magnitude and significantly spreads out towards large distances.

The importance of allowing the pairing interaction to couple properly to the particle continuum is illustrated in Fig. 19, where the neutron rms radius, the average pairing gap, and the Fermi energy are shown as functions of R_{box} . The two upper plots confirm that a stability of results is attained beyond 20 or 22 fm, while the bottom plot indicates that the pairing coupling to the positive-energy states can be a decisive factor influencing the nuclear binding. Indeed, below $R_{\text{box}} \simeq 20$ fm the nucleus ^{172}Sn is unbound, and it becomes bound only when its ground state is allowed to gain an additional binding from the pairing correlations at large distances. This indicates that, for the surface-type pairing interaction, one has to consider a rather dense particle continuum before the pairing coupling to positive-energy states is exhausted. (For a similar discussion in a schematic model see Ref. [34]. There, it has been pointed out that because of strong coupling to the continuum, λ is significantly lowered in the case of surface pairing as compared to the case of volume pairing.)

Since, for the Gogny interaction, the HFB equations are solved by expansion in the harmonic oscillator basis, one can test the coupling to the positive-energy states by increasing the number N_{sh} of the oscillator shells used in the basis. In practice, calculations must be restricted to $N_{\text{sh}} \leq 20$, which allows one to describe the wave functions up to about $R_{\text{max}} \simeq \sqrt{2N_{\text{sh}}\hbar/m\omega_0}$, where ω_0 is the frequency of the harmonic oscillator [14]. For $N_{\text{sh}}=20$ this corresponds to about $R_{\text{max}}=14$ fm.

Figure 20 compares the asymptotic behavior of the neutron particle densities in three neutron-rich tin isotopes calculated in the spatial coordinates (SkP) or in the harmonic-oscillator basis (D1S). In the former case one obtains a clean region of the asymptotic dependence governed by Eq. (5.14a), which around $r=18$ fm is perturbed by the box boundary conditions (5.2) at $R_{\text{box}}=20$ fm. In the latter case, the region of proper asymptotic behavior becomes perturbed by the $\exp(-m\omega_0 r^2/\hbar)$ dependence characteristic of the harmonic-oscillator-basis wave functions. The ω_0 values, obtained by minimizing the total energy for the $N_{\text{sh}}=17$ basis, are equal to 13.4, 6.6, and 6.3 MeV in ^{132}Sn , ^{150}Sn , and ^{172}Sn , respectively. Due to this, a study of the continuum influence using such a basis can be performed only up to densities of scattering states corresponding to about $R_{\text{box}}=14$ fm in the heavier isotopes and only $R_{\text{box}}=10$ fm in ^{132}Sn , as can be seen in Fig. 9. Let us note, however, that the neutron densities beyond $r=10$ fm are typically smaller than 10^{-4} fm^{-3} , which explains the stability of the HFB calculations with increasing size of the basis.

This is illustrated in Fig. 21 which is analogous to the similar study presented for the SkP interaction in Fig. 19. Here, for each value of N_{sh} and for each nucleus, the value of ω_0 was optimized so as to minimize the total energy. As can be seen, one obtains a nice stability of results by using $N_{\text{sh}}=17$. This test corresponds to testing the coordinate-representation solutions (Fig. 19) in the range of box sizes between $12 \text{ fm} \leq R_{\text{box}} \leq 14 \text{ fm}$. In this rather narrow region, the SkP results are not stable because of the dominant surface-type character of its pairing interaction. Since the p-p Gogny interaction is more of the volume type (Sec. III C 1) it requires much smaller distances to saturate.

H. BCS approximation

When inspecting Fig. 9, it is obvious that by applying the BCS approximation to the state-independent pairing force and by allowing the BCS-type pairing correlations to develop in such a dense spectrum, the result can be disastrous. The seniority force gives rise to the *non-localized pairing field* [52],

$$\tilde{h}_{\text{BCS}}(\mathbf{r}\sigma, \mathbf{r}'\sigma') = -\Delta_{\text{BCS}}\delta(\mathbf{r} - \mathbf{r}')\delta_{\sigma\sigma'}, \quad (5.16)$$

i.e., to a constant pairing gap, identical for all states. The high density of single-particle states in the particle continuum immediately results in an unrealistic increase of BCS pairing correlations [14]. One may, in principle, artificially readjust the pairing strength constant to avoid such an increase, but then the predictive power of the approach is lost and, moreover, the spatial asymptotic properties of the solutions are still going to be incorrect.

To illustrate the latter point, Fig. 22 (top panel) shows the neutron densities in ^{150}Sn calculated for several values of R_{box} within the HF+BCS approximation. In order to avoid the increase of pairing correlations with increasing density of states, the calculations have been performed by fixing the values of the pairing gap. For every box size R_{box} , the value of Δ_{BCS} has been set equal to the average pairing gap $\langle\Delta\rangle$ obtained within the HFB method. The corresponding $\langle\Delta\rangle$ values are quoted in Fig. 18.

It is not too surprising to see that the asymptotic behavior of the density calculated in the HF+BCS+ $\langle\Delta\rangle$ method (top panel) is entirely different than that shown in Fig. 16. Due to a nonzero occupation probability of quasibound states, there appears an unphysical gas of neutrons surrounding the nucleus. In Fig. 22 this gas has a constant density of $\rho \simeq 6 \times 10^{-5} \text{ fm}^{-3}$, independent of R_{box} . This result means that an external pressure would have been necessary to keep the neutrons inside the box. Namely, had the box boundary condition been released, one would have observed a stream of neutrons escaping the nucleus. This is a completely artificial (and unwanted) feature of the BCS approximation, because for a negative value of the Fermi energy, neutrons cannot be emitted.

In the above example the density of the neutron gas at $R_{\text{box}}=25 \text{ fm}$ corresponds to about 4 neutrons uniformly distributed in the sphere of $R=R_{\text{box}}$. Needless to say, by increasing the box radius, the number neutrons in the gas grows at the expense of the number of neutrons constituting the nucleus in the center of the box. Since the total average number of neutrons is conserved, by changing R_{box} one actually performs an unphysical study of *different* nuclei, surrounded by a neutron gas of a fixed density. Another consequence of the presence of a gas of particles is that the rms nuclear radius cannot be calculated in the BCS theory, because the results strongly depend on the box size (see discussion in Refs. [52,11]).

It has been suggested in the literature [86] that the above deficiencies of the BCS approximation can be cured by applying to them the state-dependent-pairing-gap version, where the pairing gap is calculated for every single-particle state using an interaction which is not of the seniority type. (The corresponding BCS equations resemble the canonical-basis relations (4.26).) In such an approach one hopes that the majority of continuum states would neither contribute to the pairing field (e.g., because of their very different spatial character) nor result in the appearance of the unphysical gas. This conjecture is tested in Fig. 22 (middle and bottom panel) where the neutron densities obtained within the state-dependent version of the BCS approximation using the SkP $^{\delta}$ and the SkP interactions are presented.

It is seen that a reduced coupling of some continuum states to the pairing field does indeed decrease the gas density, however, the asymptotic behavior of the density is still incorrect.

In the above plots, the shaded lines represent the asymptotic behavior given by Eq. (5.14a) assuming $E_{\min}=0$, i.e., that of a single-particle state at the Fermi energy. It is seen that a surplus density above this asymptotic limit appears at large distances. However, the deficiencies of the state-dependent BCS approximation, as used for example in Refs. [86,36,87], are certainly less acute than those of the seniority-pairing BCS. For example, in this type of approach one may probably calculate radii of nuclei much nearer to the drip line.

It is clear that the neutron gas appears in the BCS solutions because of the nonzero occupation probabilities of scattering states. Therefore, one may think that excluding the scattering states from the pairing phase space could be a decisive solution to the problem. However, for drip-line nuclei, where the Fermi energy is by definition close to zero, the remaining phase space would then be small, and this would lead to an artificial quenching of pairing correlations. Moreover, even if the density obtained in such method would vanish asymptotically, the corresponding factor χ would not be governed by $\Delta-\lambda\simeq 2\text{ MeV}$, as discussed in Sec. VF, but by the single-particle energy, $\epsilon\simeq 0$, of the highest-energy single-particle state considered in BCS calculations. This again would lead to densities vanishing at much slower pace than it is required by the HFB theory.

VI. PHYSICAL OBSERVABLES FAR FROM STABILITY

In this section discussed are some experimental consequences of the HFB theory, particularly important for weakly bound nuclei.

A. Pairing gaps

Pairing gaps are p-p analogs of single-particle energies. They carry the information about the energies of non-collective excitations, level occupations, odd-even mass differences, and other observables. The average neutron canonical pairing gaps (4.22b) are shown in Figs. 23 (^{120}Sn) and 24 (^{150}Sn) as functions of the canonical single-particle energies (4.22a).

As seen in the middle part of Fig. 23, pairing gaps obtained with the volume-type pairing interaction exhibit very weak configuration dependence. In ^{120}Sn they decrease slightly with ϵ_μ but remain confined between 1.0 and 1.5 MeV. In general, the values of Δ_μ for the $s_{1/2}$ states are slightly larger than for other orbitals, which is again related to the volume character of volume delta interaction.

The results presented in the bottom part of Fig. 23 nicely illustrate the surface character of the SkP pairing interaction. Indeed, here the pairing gaps increase from 0.5 MeV (deep-hole states) to about 1.25–1.5 MeV when the single-particle energies increase towards the Fermi energy, and then they decrease again to about 1.0 MeV for positive single-particle energies. This is related to the fact that orbitals near the Fermi level are concentrated in the surface region.

Still another type of behavior is obtained for the finite range Gogny interaction (top part of Fig. 23). Here, the pairing gaps decrease steadily with single-particle energy. In

^{120}Sn the values of Δ_μ decrease from about 2.5 MeV for deep-hole states to about 0.75 MeV for positive-energy states. (A similar energy dependence of pairing gaps was obtained in the BCS calculations of Ref. [17] with the renormalized Paris potential.) Interestingly, the values obtained for the high- ℓ , $j=\ell-\frac{1}{2}$ orbitals (antiparallel $L-S$ coupling) are significantly larger than those for other orbitals. The different ranges of ϵ_μ values for SkP and D1S in Fig. 23 reflects the different effective masses in both models. A rather low effective mass in D1S, $m^*/m=0.70$, gives rise a reduced level density and a more bound $1s_{1/2}$ ground state as compared with the SkP model ($m^*/m=1$). In fact, due to the non-local exchange contributions to the p-h mean field (Appendix A), the $1s_{1/2}$ state in the Gogny model has the canonical energy lower than the bottom of the local potential well, shown in Fig. 3.

In ^{120}Sn , the HFB+D1S pairing gaps at the Fermi energy are of the order of 1.75 MeV, which slightly overestimates the values corresponding to the odd-even mass staggering in this region. However, one should bear in mind that the pairing gaps at the Fermi energy are rather rough approximations to the odd-even mass difference. A more accurate description can be obtained by performing blocked HFB calculations for odd-mass isotopes. In the vicinity of ^{120}Sn this method yields the odd-even mass staggering of 1.6 MeV [56] for the D1S interaction and of 1.3 MeV [52] for the SkP interaction. Another contribution to the odd-even mass difference comes from the coupling to the low-lying collective modes. Therefore, the D1S parameters have been adjusted [56] to give the pairing gap in tin to be 0.3 MeV larger than the experimental one. On the other hand, such a margin has not been taken into account for the SkP and SkP $^\delta$ forces. Clearly, a detailed comparison of the values of pairing gaps for the interactions discussed in Fig. 23 is delicate. Much more information can actually be derived from the comparison of their dependence on the single-particle energies, which is markedly different.

The general pattern of Δ_μ remains very similar when going to the neutron-rich nucleus ^{150}Sn (Fig. 24). In particular, the magnitude of the average pairing gap in deep-hole states depends strongly on the range and density dependence of pairing interaction.

Figures 25 shows the average neutron pairing gaps (Eqs. (4.6) and (4.25)) for SkP, SIII $^\delta$, and D1S interactions. The large values of $\langle\Delta\rangle$ obtained in HFB+D1S can be explained by: (i) an overall larger magnitude of pairing correlations in tin nuclei, and (ii) strong pairing correlations in deep-hole states which strongly contribute to the average, Eq. (4.25). It is to be noted, however, that despite stronger pairing in D1S, the HFB+D1S pairing gaps vanish at $N=126$ (near the two-neutron drip line), in contrast to the HFB+SkP result. This difference may be traced back to a much larger continuum phase space taken into account in our HFB+SkP calculations (Sec. V G) which are performed in the coordinate representation, and to a larger $N=126$ shell gap (4.2 MeV in ^{168}Sn) obtained with D1S. (The increase of proton pairing gaps when approaching the proton drip line has been calculated previously in Ref. [79] with the HFB+SkP model and explained in a similar way.) The disappearance of the neutron pairing at $N=126$ in the HFB+SIII $^\delta$ model is partly due to the volume character of \tilde{h} (a weaker coupling to the particle continuum) and partly due to a larger $N=126$ shell gap [53].

B. Shell effects

As discussed in Sec. IV A, diffused nucleonic densities and very strong, surface-peaked, pairing fields obtained with the density-dependent pairing interaction are expected to lead to very shallow single-particle potentials in drip-line nuclei. Because of a very diffuse surface (no flat bottom), the resulting single-particle spectrum resembles that of a harmonic oscillator with a spin-orbit term (but with a weakened ℓ^2 term) [77]. Schematically, this effect is illustrated in the left panel of Fig. 26. By comparing with the situation characteristic of stable nuclei (right panel of Fig. 26), new shell structure emerges with a more uniform distribution of normal-parity orbits, and the unique-parity intruder orbit which reverts towards its parent shell. Such a new shell structure, with no pronounced shell gaps, would give rise to different kinds of collective phenomena [14,88].

The effect of the weakening of shell effects in drip-line nuclei, first mentioned in the astrophysical context [89], was further investigated in Refs. [10,77,53]. First analyses of its consequences for the nucleosynthesis have also been performed [13,90]. Microscopically, it can be explained by: (i) the changes in the mean field itself due to weak binding (see above), and (ii) a strong pairing-induced coupling between bound orbitals and the low- ℓ continuum.

C. Separation energies

Weakening of shell effects with neutron number manifests itself in the behavior of two-neutron separation energies. This is illustrated in Fig. 27 which displays the two-neutron separation energies for the $N=80, 82, 84$, and 86 spherical even-even isotones. The large $N=82$ magic gap, clearly seen in the nuclei close to the stability valley and to the proton-drip line, gradually closes down when approaching the neutron drip line. A similar effect is seen in the (Z, N) map of the spherical two-neutron separation energies for the particle-bound even-even nuclei calculated in the HFB+SkP model (Fig. 28). Namely, the neutron magic gaps $N=20, 28, 50, 82$, and 126 , clearly seen as cliffs in the S_{2n} surface, disappear for neutron-rich systems.

The gradual disappearance of the neutron shell structure with N is not a generic property of all effective interactions. As seen in the plot of S_{2n} and λ_N for the tin isotopes (Fig. 29) this effect is seen in the SkP and SkP $^{\delta\rho}$ models, and, to some degree, also in the SkP $^\delta$ model. (A weak irregularity at $N=126$ reflects the weaker coupling to continuum for the volume pairing [34].) The strong shell effect seen in the SIII and SkM* results has been discussed in Ref. [53]; it can be attributed to the low effective mass in these forces. The result of the D1S model, both for S_{2n} and λ_N , is close to that of the SkP $^\delta$ model. It is interesting to point out that the QLM calculations of Ref. [42] (with $m^*/m = 1$) for the Sn isotopes yield very similar results to those of HFB+SkP.

The very neutron-rich nuclei, as those shown in Fig. 29, cannot be reached experimentally under present laboratory conditions. On the other hand, these systems are the building blocks of the astrophysical r-process; their separation energies, decay rates, and cross sections are the basic quantities determining the results of nuclear reaction network calculations. Consequently, one can learn about properties of very neutron-rich systems by studying element abundances [91]. The recent r-process network calculations [13], based on several

mass formulae, indicate a quenching of the shell effect at $N=82$ in accordance with the results of HFB+SkP model.

D. Deep hole states

Pairing interaction between bound orbitals and particle continuum is partly responsible for the appearance of particle widths of deep-hole states and the term-repulsion phenomenon (strong repulsion between single-particle levels) [33,34]. In the DWBA and for the local pairing field \tilde{U} the particle width is given by

$$\Gamma_i = 2\pi \left| \int d^3\mathbf{r} \varphi_i(\mathbf{r}) \tilde{U}(\mathbf{r}) \varphi_\epsilon(\mathbf{r}) \right|^2. \quad (6.1)$$

Here, $\varphi_i(r)$ is the HF wave function of the bound deep-hole state i with the single-particle energy $\lambda - E_i$ in the absence of pairing, while $\varphi_\epsilon(r)$ is the HF wave function of the unbound state with the energy $\lambda + E_i$.

Equation (6.1) is obtained by assuming that the p-p field of the HFB Hamiltonian can be treated perturbatively. A more consistent way would be to estimate Γ_i based on self-consistent HFB solutions containing pairing correlations. The proper formulation of the nonperturbative HFB-based theory of deep hole states and one-particle transfer process still needs to be developed.

As discussed in Ref. [34], Γ_i is sensitive to the type of the pairing force. In general, the widths are larger for surface pairing than for volume pairing. However, the result for an individual state strongly depends on its angular momentum and excitation energy.

Experimentally, total widths of deep hole states, Γ_{tot} , are of the order of MeV's, (see, e.g., Refs. [92–95]). That is, the partial width (6.1), of the order of 10-100 keV, constitutes an extremely small fraction of Γ_{tot} . Consequently, the experimental determination of Γ_i alone is very unlikely.

E. Pair transfer form factors

There are many interesting aspects of physics of unstable nuclei which are related to reaction mechanism studies: weak binding, large spatial dimensions, skins (see, e.g., Refs. [2,96,97]). Below, we discuss some consequences of surface-peaked pairing fields for pair transfer studies.

An experimental observable that may probe the character of the pairing field is the pair transfer form factor, directly related to the pairing density $\tilde{\rho}$. The difference in the asymptotic behavior of single-particle density ρ and pair density $\tilde{\rho}$ in a weakly bound system (see Secs. III C 1 and V F) can be probed by comparing the energy dependence of one-particle and pair-transfer cross sections. Such measurements, when performed for both stable and neutron-rich nuclei, can shed some light on the asymptotic properties of HFB densities; hence on the character of pairing field.

Figure 30 displays the pair transfer form factors $r^2\tilde{\rho}(r)$ calculated in ^{120}Sn , ^{150}Sn , and ^{172}Sn with the SkP interaction. These microscopic results are compared with the macroscopic

form factors $r^2\delta\rho(r)$ [98] which are determined by using the derivative of the particle density with respect to the neutron number:

$$\delta\rho(r) = 2\frac{-E_{\text{pair}}}{\langle\Delta\rangle}\frac{d\rho(r)}{dN}, \quad (6.2)$$

where E_{pair} is given by Eq. (4.5). This expression can be motivated by the fact that only the orbitals near the Fermi surface make significant contributions to the pair density. In the BCS theory, the normalization constant in $\delta\rho(r)$ is usually chosen [99] as $\Delta/G = -E_{\text{pair}}/\Delta$. Here, we use neither the BCS approximation nor the constant pairing strength G . Therefore, the normalization $-E_{\text{pair}}/\langle\Delta\rangle$ is employed. The derivative in Eq. (6.2) is calculated from the finite difference between the self-consistent results for the HFB vacuum corresponding to particle numbers $N+1$ and $N-1$. In these calculations, in order to explore the smooth dependence on the particle number N , the odd-average-particle-number vacua have been calculated without using the blocking approximation. It should be mentioned at this point that the further approximation [98,100] of the derivative $d\rho(r)/dN$ by the spatial derivative $d\rho(r)/dr$ is not justified, because the volume-conservation condition is not valid for the neutron density distribution (see Fig. 1).

The pair transfer form factors in Fig. 30 clearly show that this process has a predominantly surface character. The macroscopic form factors have smaller widths and higher maxima than the microscopic ones. On the other hand, they are smaller in the interior of the nucleus as well as in the asymptotic region. In β -stable nuclei the macroscopic approximation works fairly well, while in the drip-line nuclei the differences between the two form factors are markedly larger. In general, the corresponding differences are much larger than those obtained within the BCS and the particle-number-projected BCS approaches for the seniority interaction [101].

A comparison of the results obtained for different isotopes conspicuously shows a significant increase in the pair transfer form factors in the outer regions of drip-line nuclei. In ^{120}Sn , the form factors vanish around 9 fm, while in ^{150}Sn and ^{172}Sn they extend to much larger distances. This effect is particularly pronounced for the microscopic pair transfer form factors.

F. Other observables

The importance of the HFB treatment for calculations of nuclear radii has been discussed in several papers [52,79,31,11]. As mentioned in Sec. II, odd-even staggering of rms charge radii is one of the best experimental indicators of the density-dependent pairing. The proper treatment of the pairing effect on radii is especially important for weakly bound systems which exhibit halo or skin effects [35,79,11] (cf. discussion in Sec. V G).

Apart from the information on the nuclear rms radii, one may also gain some experimental insight into the ratios of neutron and proton densities at large distances from the center of nucleus [102,103]. This is possible due to experiments on antiproton annihilation from atomic orbits, which leads to different reaction products depending on whether the process involves a proton or a neutron.

The role of deformation in neutron drip-line nuclei still needs to be investigated. One can anticipate that due to: (i) very diffused surfaces, and (ii) strong pairing correlations, the

geometric concept of collective deformation (defined as a deviation of nuclear surface from sphericity) should be revisited. In this context, the symmetry-unrestricted HFB calculations in coordinate space are called for.

VII. SUMMARY AND CONCLUSIONS

The advent of radioactive nuclear beams provides many exciting opportunities to create and study unstable nuclei far from the β stability valley. One of the unexplored areas far from stability is physics of nuclear pairing in weakly bound nuclei, especially near the neutron drip line. Contrary to the situation characteristic of stable nuclei, the coupling between the p-h field and the p-p field in nuclei with extreme N/Z ratios is dramatic; i.e., no longer can pairing be treated as a residual interaction.

The main objective of this study was to perform a detailed analysis of various facets of pairing fields in atomic nuclei. The first part contains the comprehensive summary of the HFB formalism, with particular attention on the physical interpretation of the underlying densities and fields. Very little is known about the p-p component of the nuclear effective interaction; its structure is of considerable importance not only for nuclear physics but also for nuclear astrophysics and cosmology. Therefore, the second part of this work focuses on the differences between various pairing interactions. In particular, the role of density dependence and finite range of the p-p force has been illuminated, and the importance of the coupling to the particle continuum has been emphasized. Finally, the third part of our study relates the theoretical formalism to experimental observables; i.e., energy spectra, masses, radii, and pair transfer form factors. It is demonstrated that these observables carry invaluable information that can pin down many basic questions regarding the effective NN force, and its pairing component in particular. It should be stressed, however, that in order to see clearly some of the predicted effects, the excursion far from the valley of β -stability is necessary.

The analysis presented in this paper should be viewed as a useful starting point for future investigations. One of them is the coupling between collective surface modes (e.g., deformation) and pairing fields in weakly bound nuclei. Another interesting avenue of explorations is the role of dynamics; e.g., the importance of the particle number conservation and the coupling to pair vibrations. A fascinating and difficult research program is the microscopic description of excited states, especially those lying above the particle emission threshold, for which the boundary conditions used in this study (an impenetrable box) have to be modified to account explicitly for outgoing waves. We are only beginning to explore many unusual aspects of the nuclear many-body problem offered by systems with extreme N/Z ratios.

ACKNOWLEDGMENTS

Interesting discussions with H. Flocard, P.-H. Heenen, and H. Lenske are gratefully acknowledged. Oak Ridge National Laboratory is managed for the U.S. Department of Energy by Lockheed Martin Energy Systems under Contract No. DE-AC05-84OR21400. The Joint Institute for Heavy Ion Research has as member institutions the University of Tennessee, Vanderbilt University, and the Oak Ridge National Laboratory; it is supported by

the members and by the Department of Energy through Contract No. DE-FG05-87ER40361 with the University of Tennessee. We thank the Department of Energy's Institute for Nuclear Theory at the University of Washington for its hospitality and partial support during the completion of this work. This research was supported in part by the U.S. Department of Energy through Contract No. DE-FG05-93ER40770 and the Polish Committee for Scientific Research under Contract No. 2 P03B 034 08.

APPENDIX A: THE P-H AND P-P MEAN-FIELD HAMILTONIANS FOR A LOCAL TWO-BODY FINITE-RANGE GOGNY INTERACTION

The Gogny force [57,56] is composed of the central, spin-orbit, density-dependent, and Coulomb interactions. The spin-orbit and density-dependent terms have zero-range, and their contributions to the p-h and p-p mean fields are identical to those of the Skyrme interaction. The corresponding expressions can be found in several papers; e.g., Refs. [104,52], and will not be repeated here. In the following we only consider the central finite-range and Coulomb terms. The central components read

$$\hat{V}_{\text{cen}} = \sum_{j=1}^2 e^{-\frac{(\mathbf{r}-\mathbf{r}')^2}{\mu_j^2}} (W_j + B_j P_\sigma - H_j P_\tau - M_j P_\sigma P_\tau), \quad (\text{A1})$$

where P_σ and P_τ are the exchange operators for spin and isospin variables, respectively. This interaction is local; i.e., it should be multiplied by $\delta(\mathbf{r}_1 - \mathbf{r}'_1)\delta(\mathbf{r}_2 - \mathbf{r}'_2)$ before it is inserted in the integrals (4.3) defining the mean fields. Moreover, it should also be multiplied by the antisymmetrizing operator $(1 - P_r P_\sigma P_\tau)$, where P_r is the exchange operator for space variables. One usually calls the term involving P_r the exchange term, while the term involving no space exchange is called the direct term.

The space, spin, and isospin variables are denoted by \mathbf{r} , $\sigma = \pm\frac{1}{2}$, and $\tau = \pm\frac{1}{2}$, respectively. The parameters μ_j , W_j , B_j , H_j , and M_j , belong to the set called D1S [105] which has been used in this paper. Since the expressions given by the $j=1$ and 2 components are identical, in what follows we drop the index j to increase the legibility of the formulae.

1. Contribution of the central direct interaction to the p-h mean field

Since the interaction (A1) is local, the direct term gives the p-h mean field (4.3a) which is also local, i.e.,

$$\begin{aligned} \Gamma_{\text{dir}}^\tau(\mathbf{r}\sigma, \mathbf{r}'\sigma') &= \delta(\mathbf{r} - \mathbf{r}')\delta_{\sigma\sigma'} \int d^3\mathbf{r}_1 e^{-\frac{(\mathbf{r}-\mathbf{r}_1)^2}{\mu^2}} \sum_{\tau_1} \left[(W - H\delta_{\tau\tau_1})\rho^{\tau_1}(\mathbf{r}_1) + (B - M\delta_{\tau\tau_1})\rho^{\tau_1}(\mathbf{r}_1\sigma, \mathbf{r}_1\sigma) \right] \\ &\quad + \delta(\mathbf{r} - \mathbf{r}')\delta_{\sigma-\sigma'} \int d^3\mathbf{r}_1 e^{-\frac{(\mathbf{r}-\mathbf{r}_1)^2}{\mu^2}} \sum_{\tau_1} (B - M\delta_{\tau\tau_1})\rho^{\tau_1}(\mathbf{r}_1\sigma, \mathbf{r}_1 - \sigma), \end{aligned} \quad (\text{A2})$$

where $\rho^\tau(\mathbf{r})$ is the density of nucleons (3.30a) of type τ .

Assuming that we consider only the states which are even with respect to the time reversal, the density matrix (3.17a) obeys the relation (3.18a). Consequently, the densities $\rho^\tau(\mathbf{r}\sigma, \mathbf{r}\sigma)$ for $\sigma = \pm\frac{1}{2}$ are equal to $\frac{1}{2}\rho^\tau(\mathbf{r})$, and the densities $\rho^\tau(\mathbf{r}\sigma, \mathbf{r} - \sigma)$ vanish. Therefore,

the term in (A2), which is proportional to $\delta_{\sigma-\sigma'}$, vanishes, and the contribution of the direct term to the p-h mean field is the local, spin-independent potential:

$$\Gamma_{\text{dir}}^{\tau}(\mathbf{r}\sigma, \mathbf{r}'\sigma') = \delta(\mathbf{r} - \mathbf{r}')\delta_{\sigma\sigma'}U(\mathbf{r}), \quad (\text{A3})$$

where

$$U(\mathbf{r}) = \int d^3\mathbf{r}_1 e^{-\frac{(\mathbf{r}-\mathbf{r}_1)^2}{\mu^2}} \left[(W + B/2)\rho(\mathbf{r}_1) - (H + M/2)\rho^{\tau}(\mathbf{r}_1) \right]. \quad (\text{A4})$$

One should note that due to the locality of the interaction, the direct term depends only on the local densities.

2. Contribution of the central exchange interaction to the p-h mean field

Due to the locality of the interaction, the contribution of the exchange term to the p-h mean field involves no integration:

$$\begin{aligned} \Gamma_{\text{exc}}^{\tau}(\mathbf{r}\sigma, \mathbf{r}'\sigma') &= e^{-\frac{(\mathbf{r}-\mathbf{r}')^2}{\mu^2}} \sum_{\tau_1} \left[\delta_{\sigma\sigma'} \left((M - B\delta_{\tau\tau_1}) \sum_{\sigma_1} \rho^{\tau_1}(\mathbf{r}\sigma_1, \mathbf{r}'\sigma_1) + (H - W\delta_{\tau\tau_1}) \rho^{\tau_1}(\mathbf{r}\sigma, \mathbf{r}'\sigma) \right) \right. \\ &\quad \left. + \delta_{\sigma-\sigma'} (H - W\delta_{\tau\tau_1}) \rho^{\tau_1}(\mathbf{r}\sigma, \mathbf{r}' - \sigma) \right]. \end{aligned} \quad (\text{A5})$$

Here the time-reversal symmetry does not bring any simplification. However, a simpler formula is obtained in cases where $\rho^{\tau_1}(\mathbf{r}\sigma, \mathbf{r}'\sigma')$ is real. It follows from Eq. (3.18a) that the densities $\rho^{\tau_1}(\mathbf{r}\sigma, \mathbf{r}'\sigma)$ are equal to $\frac{1}{2} \sum_{\sigma} \rho^{\tau_1}(\mathbf{r}\sigma, \mathbf{r}'\sigma)$, which finally leads to

$$\Gamma_{\text{exc}}^{\tau}(\mathbf{r}\sigma, \mathbf{r}'\sigma) = e^{-\frac{(\mathbf{r}-\mathbf{r}')^2}{\mu^2}} \sum_{\tau_1} \left[M + H/2 - (B + W/2)\delta_{\tau\tau_1} \right] \sum_{\sigma_1} \rho^{\tau_1}(\mathbf{r}\sigma_1, \mathbf{r}'\sigma_1), \quad (\text{A6})$$

$$\Gamma_{\text{exc}}^{\tau}(\mathbf{r}\sigma, \mathbf{r}' - \sigma) = e^{-\frac{(\mathbf{r}-\mathbf{r}')^2}{\mu^2}} \sum_{\tau_1} (H - W\delta_{\tau\tau_1}) \rho^{\tau_1}(\mathbf{r}\sigma, \mathbf{r}' - \sigma). \quad (\text{A7})$$

3. Contribution of the Coulomb interaction to the p-h mean field

Derivation of the direct and exchange Coulomb fields is similar to the one of the finite range term (A1) with several additional simplifications. When the nuclear state is time-reversal invariant, one obtains the following contributions to the proton p-h mean field in terms of the proton densities:

$$\Gamma_{\text{Coul-dir}}^p(\mathbf{r}\sigma, \mathbf{r}'\sigma') = \delta(\mathbf{r} - \mathbf{r}')\delta_{\sigma\sigma'} \int d^3\mathbf{r}_1 \frac{e^2}{|\mathbf{r} - \mathbf{r}_1|} \rho^p(\mathbf{r}_1), \quad (\text{A8})$$

$$\Gamma_{\text{Coul-exc}}^p(\mathbf{r}\sigma, \mathbf{r}'\sigma') = \frac{e^2}{|\mathbf{r} - \mathbf{r}'|} \rho^p(\mathbf{r}\sigma, \mathbf{r}'\sigma'). \quad (\text{A9})$$

4. Contribution of the central interaction to the p-p mean field

The general form of the pairing field is given by Eq. (4.3b). In this case the direct and the exchange contributions are equal. For the local central force (A1), the total contributions to the p-p mean field have the form:

$$\tilde{h}^\tau(\mathbf{r}\sigma, \mathbf{r}'\sigma) = e^{-\frac{(\mathbf{r}-\mathbf{r}')^2}{\mu^2}} [(W - H)\tilde{\rho}^\tau(\mathbf{r}\sigma, \mathbf{r}'\sigma) - (B - M)\tilde{\rho}^\tau(\mathbf{r}'\sigma, \mathbf{r}\sigma)], \quad (\text{A10})$$

$$\tilde{h}^\tau(\mathbf{r}\sigma, \mathbf{r}' - \sigma) = e^{-\frac{(\mathbf{r}-\mathbf{r}')^2}{\mu^2}} (W + B - H - M)\tilde{\rho}^\tau(\mathbf{r}\sigma, \mathbf{r}' - \sigma). \quad (\text{A11})$$

Again it is to be noted that due to the locality of the interaction, the corresponding p-p mean fields do not involve any integration but are proportional to the pairing density matrices. In the case considered in this study (time-even densities), the contribution (A11) vanishes.

Since the exchange parameter of the zero-range density-dependent term of the Gogny D1S interaction is fixed at $x_0=1$, this term does not contribute to the p-p mean field. Moreover, the spin-orbit and Coulomb terms usually give small contributions as compared to those of the central force (A1).

5. Numerical methods used for the calculation of the mean fields

Computation of the exchange p-h mean fields, Eqs. (A6), (A7), and (A9), and the pairing fields, Eqs. (A10) and (A11), is straightforward. It only requires the knowledge of the spatial spin-dependent non-local particle, $\rho^\tau(\mathbf{r}\sigma, \mathbf{r}'\sigma')$, and pairing $\tilde{\rho}^\tau(\mathbf{r}\sigma, \mathbf{r}'\sigma')$ densities.

Computation of the direct p-h mean field, Eq. (A3), and the direct Coulomb mean field, Eq. (A8), is more complicated since it requires the evaluation of three-dimensional integrals of the form:

$$I_\mu(\mathbf{r}) = \int d^3\mathbf{r}' e^{-\frac{(\mathbf{r}-\mathbf{r}')^2}{\mu^2}} \rho(\mathbf{r}'), \quad (\text{A12})$$

$$I_C(\mathbf{r}) = \int d^3\mathbf{r}' \frac{1}{|\mathbf{r} - \mathbf{r}'|} \rho(\mathbf{r}'). \quad (\text{A13})$$

In order to compute $I_\mu(\mathbf{r})$ of Eq. (A12) we note that for the single-particle wave functions expanded in the harmonic oscillator basis, the local density $\rho(\mathbf{r})$ is the product of a Gaussian factor and of a polynomial in the spatial coordinates x_1 , x_2 , and x_3

$$\rho(\mathbf{r}) = \exp \left[- \sum_{k=1}^3 \left(\frac{x_k}{b_k} \right)^2 \right] P(x_1, x_2, x_3), \quad (\text{A14})$$

where b_1 , b_2 and b_3 are the HO lengths of the basis states. Consequently, this integral can be evaluated exactly using the Gauss-Hermite quadrature.

The computation of the Coulomb integral (A13) is more difficult due to the infinite range of the Coulomb force. The method we have used consists of expressing the Coulomb force as a sum of Gaussians:

$$\frac{1}{|\mathbf{r} - \mathbf{r}'|} = \frac{2}{\sqrt{\pi}} \int_0^\infty \frac{d\mu}{\mu^2} e^{-\frac{(\mathbf{r}-\mathbf{r}')^2}{\mu^2}}. \quad (\text{A15})$$

Then one obtains

$$I_C(\mathbf{r}) = \frac{2}{\sqrt{\pi}} \int_0^\infty \frac{d\mu}{\mu^2} I_\mu(\mathbf{r}) \quad (\text{A16})$$

where $I_\mu(\mathbf{r})$ is given by Eq. (A12). In order to perform the remaining one-dimensional integration, the variable μ is changed to

$$\xi = b/\sqrt{b^2 + \mu^2}, \quad (\text{A17})$$

where b is the largest of the three harmonic-oscillator lengths b_1 , b_2 and b_3 . This change of variable is very convenient, since then the range of integration becomes $[0, 1]$. The integral in Eq. (A16) can be very accurately computed using the Gauss-Legendre quadrature.

APPENDIX B: THE ENERGY CUT-OFF

Calculations which are based on the schematic pairing interaction, or on the contact force [Eq. (2.2)] require a finite space of states in the p-p channel. For such interactions, when this space is increased, the pairing energy diverges for any fixed strength of the interaction. This divergence is a well-known effect [23] related to the fact that for the contact interactions the matrix elements do not (or too slowly) decrease with the excitation energy. This is not a case for finite-range interactions, such as Gogny, for which the pairing energy converges to a finite value.

Since it is considerably easier to use the zero-range interactions than the finite-range interactions, one applies the former ones in a limited configuration space determined by a cut-off in the single-particle energy or in the single-quasiparticle energy. This can be understood as a phenomenological introduction of the finite range [35]. There are two other arguments in favor of such a procedure. First, the scattering of particles in the nuclear medium at very high energies (or at very small distances) is very little known, and the particular form offered by any phenomenological finite-range force is very uncertain. Second, the single-particle wave functions are primarily determined by the p-h channel of interaction, and they, in general, spread throughout distances which are much larger than the range of the p-p interaction. Therefore, physical differences between the zero- and short-range p-p forces cannot be expected to be very pronounced.

Within the BCS approximation, and assuming a constant density of the single-particle states at large energies, one can derive [23,106] a prescription to renormalize the strength of the p-p interaction in such a way that the pairing gap Δ does not depend on the energy cut-off. Suppose that the single-particle states with energies $-\epsilon_l \leq \epsilon - \lambda \leq \epsilon_u$ are used to solve the BCS equations for the force of strength V_0 . Then, within the specified approximations, the following relation holds:

$$V_0 = -\frac{C_0}{\ln(2\sqrt{\epsilon_l \epsilon_u}/\Delta)}, \quad (\text{B1})$$

where $C_0 \simeq 300 \text{ MeV fm}^3$ is a constant inversely proportional to the density of single-particle states near the Fermi energy. In other words, for given values of C_0 and Δ , Eq. (B1) gives values of V_0' for any other choice of the cut-off energies ϵ_l' and ϵ_u' .

Since in the present study we use the HFB method instead of the BCS approximation, and since the density of states can hardly be considered to be independent of energy (actually for fixed R_{box} it increases as $\sqrt{\epsilon}$), the formula (B1) cannot be directly used. However, the question as to what extent the pairing strengths can be renormalized for a zero-range p-p interaction can be addressed by analyzing the numerical solutions of the HFB equations.

Figure 31 (top panel) shows the neutron pairing energies E_{pair} [Eq. (4.5)] calculated for the SkP $^\delta$ interaction which uses the contact p-p interaction (2.2) with $V_0 = -160 \text{ MeV fm}^3$. It should be recalled at this point that for all coordinate-space HFB calculations presented in this study, the cut-off energy, E_{max} , depends on the quantum numbers ℓj (cf. Ref. [52]). In the tin nuclei, E_{max} decreases from about 40 MeV for the $s_{1/2}$ states to zero for the $k_{17/2}$ states. In Figs. 31-33 different curves correspond to different cut-off energies, $E'_{\text{max}} = E_{\text{max}} + \Delta E_{\text{max}}$ (ΔE_{max} varied between 0 and 40 MeV). Hence, $\Delta E_{\text{max}} = 40 \text{ MeV}$ corresponds to the cut-off energy E'_{max} of 80 MeV for the $s_{1/2}$ states, and 40 MeV for the largest values of ℓ .

As expected, pairing energies depend significantly on the cut-off energy. Comparing results for $\Delta E_{\text{max}} = 40 \text{ MeV}$ with those for $\Delta E_{\text{max}} = 0$, one obtains differences of E_{pair} of the order of $10 \div 20 \text{ MeV}$ in the mid-shells. Due to the self-consistent readjustment of the p-h and p-p energies, the corresponding differences in the total energies (Fig. 32) are much smaller, $2 \div 4 \text{ MeV}$, but still significant.

In the bottom panels of Figs. 31 and 32 are shown similar results for the renormalized strengths of the contact force (2.2). The values of V_0 , quoted in the caption of Fig. 31, have been obtained by requiring that the average neutron pairing gap in ^{120}Sn , $\langle \Delta_N \rangle = 1.245 \text{ MeV}$, does not depend on ΔE_{max} . With such renormalized interactions, one obtains very small changes of total energies (Fig. 32, bottom panel). The largest deviations do not exceed 200 keV and 800 keV in stable and exotic isotopes, respectively, and can be safely disregarded when compared to all other uncertainties of methods used to extrapolate to unknown nuclei, or when studying the separation energies.

Figure 33 shows the effective pairing-interaction strengths defined schematically as $G_{\text{eff}} = -\langle \Delta \rangle^2 / E_{\text{pair}}$. The top panel presents the results obtained for $V_0 = -160 \text{ MeV fm}^3$ and for different values of ΔE_{max} . One can see that the dependence on the cut-off energy is very weak, and the ΔE_{max} -dependence of $\langle \Delta \rangle^2$ and E_{pair} cancels out in G_{eff} . (At $N=82$ the pairing gap and the pairing energy both vanish, and hence the G_{eff} values cannot be calculated.) A fixed value of V_0 gives, therefore, a well-defined, cut-off-independent value of the effective pairing strength for every isotope. This result, together with the analysis of pairing gap distributions in Sec. VIA, demonstrates that calculations employing the volume contact p-p interaction are, in many respects, similar to those with the schematic seniority-pairing force (cf., however, Sec. VF).

The values of G_{eff} monotonically decrease with increasing neutron number N . The obtained dependence can be very well described by the simple Madland-Nix formula [107], $G = 11 \text{ MeV} / (11 + N)$, while the Jensen-Miranda formula [108], $G = 0.18 \text{ MeV} [1 - 1.2I - 2.8I^2]$ ($I = (N - Z)/A$), gives a much faster decrease of G_{eff} with N . (In a recent study [109], based on a schematic finite-range force, the isospin dependence of G has been discussed. The authors found no sign of the I^2 term suggested in Ref. [108]. This probably explains the disagreement seen in Fig. 33.) In both expressions we have normalized the multiplicative constants to obtain $G = 0.18 \text{ MeV}$ at $N = Z = 50$.

The bottom panel of Fig. 33 shows similar results, but for the renormalized values of V_0 , quoted in the caption of Fig. 31. The insert shows the values of V_0 (dots) as function of ΔE_{max} compared with the simple fit by the formula (B1) with $\epsilon_u = \epsilon_l + \Delta E_{\text{max}}$, for $\epsilon_l = 40$ MeV, $C_0 = 430$ MeV fm³, and $\Delta = 5.58$ MeV (solid line). One can see that the generic dependence of the renormalized values of V_0 on ΔE_{max} is fairly well reproduced, although the numerical constants C_0 and Δ obtained from the fit do not exactly correspond to the values inferred from the BCS theory with a constant density of single-particle states.

REFERENCES

- [1] E. Roeckl, Rep. Prog. Phys. **55**, 1661 (1992).
- [2] A. Mueller and B. Sherril, Annu. Rev. Nucl. Part. Sci. **43**, 529 (1993).
- [3] P.-G. Hansen, Nucl. Phys. **A553**, 89c (1993).
- [4] W. Nazarewicz, J. Dobaczewski, and T.R. Werner, Physica Scripta, **T56**, 9 (1995).
- [5] U. Fano, Phys. Rev. **124**, 1866 (1961).
- [6] R.J. Philpott, Nucl. Phys. **A289** (1977) 109.
- [7] P.E. Haustein, At. Data Nucl. Data Tables **39**, 185 (1988).
- [8] P. Möller, J.R. Nix, W.D. Myers, and W.J. Swiatecki, Atom. Data and Nucl. Data Tables **59**, 185 (1995).
- [9] Y. Aboussir, J.M. Pearson, A.K. Dutta, and F. Tondeur, At. Data Nucl. Data Tables **61**, 127 (1995).
- [10] R. Smolańczuk and J. Dobaczewski, Phys. Rev. **C48**, R2166 (1993).
- [11] J. Dobaczewski, W. Nazarewicz, and T.R. Werner, Z. Phys., 1995, in press.
- [12] W.M. Howard, S. Goriely, M. Rayet, and M. Arnould, Astrophys. J. **417**, 713 (1993).
- [13] B. Chen, J. Dobaczewski, K.-L. Kratz, K. Langanke, B. Pfeiffer, F.-K. Thielmann, and P. Vogel, Phys. Lett. **B355**, 37 (1995).
- [14] W. Nazarewicz, T.R. Werner, and J. Dobaczewski, Phys. Rev. **C50**, 2860 (1994).
- [15] M. Beiner, R.J. Lombard, and D. Mas, Nucl. Phys. **A249**, 1 (1975).
- [16] A.M. Lane, *Nuclear Theory* (Benjamin, New York, 1964).
- [17] D.S. Delion, M. Baldo, and U. Lombardo, Nucl. Phys. **A593**, 151 (1995).
- [18] H. Kucharek and P. Ping, Z. Phys. **A339**, 23 (1991).
- [19] S.G. Kadenskii, P.A. Luk'yanovich, Yu. I. Remesov, and V.I. Furman, Sov. J. Nucl. Phys. **45**, 585 (1987).
- [20] K.A. Brueckner, T. Soda, P. W. Anderson, and P. Morel, Phys. Rev. **118**, 1442 (1960).
- [21] V.J. Emery and A.M. Sessler, Phys. Rev. **119**, 248 (1960).
- [22] I.M. Green and S.A. Moszkowski, Phys. Rev. **139**, B790 (1965).
- [23] A.B. Migdal, *Theory of Finite Fermi Systems and Applications to Atomic Nuclei* (Interscience, New York, 1967).
- [24] P. Ring and P. Schuck, *The Nuclear Many-Body Problem* (Springer-Verlag, Berlin, 1980).
- [25] Z. Bochnacki, I.M. Holban, and I.N. Mikhailov, Nucl. Phys. **A97**, 33 (1967).
- [26] É.E. Sapershtein and M.A. Troitskii, Sov. J. Nucl. Phys. **1**, 284 (1965).
- [27] R.R. Chasman, Phys. Rev. **C14**, 1935 (1976).
- [28] S.G. Kadenskii, Yu. L. Ratis, K.S. Rybak, and V.I. Furman, Sov. J. Nucl. Phys. **27**, 481 (1979).
- [29] D. Zawischa, U. Regge, and R. Stapel, Phys. Lett. **185B**, 299 (1987).
- [30] U. Regge and D. Zawischa, Phys. Rev. Lett. **61**, 149 (1988).
- [31] S.A. Fayans, S.V. Tolokonnikov, E.L. Trykov, and D. Zawischa, Phys. Lett. **338B**, 1 (1994).
- [32] M. Horoi, Phys. Rev. **C50**, 2834 (1994).
- [33] A. Bulgac, Preprint FT-194-1980, Central Institute of Physics, Bucharest, 1980.
- [34] S.T. Belyaev, A.V. Smirnov, S.V. Tolokonnikov, and S.A. Fayans, Sov. J. Nucl. Phys. **45**, 783 (1987).
- [35] G.F. Bertsch and H. Esbensen, Ann. Phys. (N.Y.) **209**, 327 (1991).

- [36] H. Lenske, Proc. Int. Symp. on Structure and Reactions of Unstable Nuclei, Niigata 1991, eds. K. Ikeda and Y. Suzuki (World Scientific, Singapore, 1991).
- [37] A.N. Ostrowski, H.G. Bohlen, A.S. Demyanova, B. Gebauer, R. Kalpakchieva, Ch. Langner, H. Lenske, M. von Lucke-Petsch, W. von Oertzen, A.A. Ogloblin, Y.E. Penionzhkevich, M. Wilpert, and Th. Wilpert, Z. Phys. **A343**, 489 (1992).
- [38] H.G. Bohlen, B. Gebauer, M. von Lucke-Petsch, W. von Oertzen, A.N. Ostrowski, M. Wilpert, Th. Wilpert, H. Lenske, D.V. Alexandrov, A.S. Demyanova, E. Nikolskii, A.A. Korshennikov, A.A. Ogloblin, R. Kalpakchieva, Y.E. Penionzhkevich, and S. Piskor, Z. Phys. **A344** (1993) 381.
- [39] N. Tajima, P. Bonche, H. Flocard, P.-H. Heenen, and M.S. Weiss, Nucl. Phys. **A551**, 434 (1993).
- [40] J. Terasaki, P.-H. Heenen, P. Bonche, J. Dobaczewski, and H. Flocard, Nucl. Phys. **A593**, 1 (1995).
- [41] M.V. Zverev and É.E. Sapershtein, Sov. J. Nucl. Phys. **39**, 878 (1984).
- [42] M.V. Zverev and É.E. Sapershtein, Sov. J. Nucl. Phys. **42**, 683 (1985).
- [43] A.V. Smirnov, S.V. Tolokonnikov, and S.A. Fayans, Sov. J. Nucl. Phys. **48**, 995 (1988).
- [44] V.A. Khodel' and É.E. Sapershtein, Phys. Rep. **92**, 12 (1982).
- [45] S. Shlomo and G. Bertsch, Nucl. Phys. **A243**, 507 (1975).
- [46] C.J. Pethick and D.G. Ravenhall, Annu. Rev. Nucl. Part. Sci. **45** (1995).
- [47] J.M.C. Chen, J.W. Clark, R.D. Davé, and V.V. Khodel, Nucl. Phys. **A555**, 59 (1993).
- [48] H. Kucharek and P. Ping, P. Schuck, R. Bengtsson, and M. Girod, Phys. Lett. **A216**, 249 (1989).
- [49] S. Takahara, N. Onishi, and N. Tajima, Phys. Lett. **B331**, 261 (1994).
- [50] M. Baldo, U. Lombardo, E.E. Saperstein, and M.V. Zverev, Phys. Lett. **350**, 135 (1995).
- [51] F. De Blasio and G. Lazzari, Nuovo Cimento **107A**, 1549 (1994).
- [52] J. Dobaczewski, H. Flocard and J. Treiner, Nucl. Phys. **A422**, 103 (1984).
- [53] J. Dobaczewski, W. Nazarewicz, and T.R. Werner, Physica Scripta **T56**, 15 (1995).
- [54] M. Beiner, H. Flocard, N. Van Giai and P. Quentin, Nucl. Phys. **A238**, 29 (1975).
- [55] J. Bartel, P. Quentin, M. Brack, C. Guet, and H.B. Håkansson, Nucl. Phys. **A386**, 79 (1982).
- [56] J. Dechargé and D. Gogny, Phys. Rev. **C21**, 1568 (1980).
- [57] D. Gogny, in: *Proc. Int. Conf. on Nuclear Physics*, eds. J. De Boer and H. Mang (North-Holland, Amsterdam, 1973).
- [58] A. Rummel and P. Ring, preprint, 1994.
- [59] J.F. Berger, M. Girod and D. Gogny, Nucl. Phys. **A502**, 85c (1989).
- [60] G.C. Wick, Phys. Rev. **80**, 268 (1950).
- [61] R. Balian and M. Vénéroni, Ann. Phys. (N.Y.) **216**, 351 (1992).
- [62] N.N. Bogoliubov, Sov. Phys. JETP **7**, 41 (1958).
- [63] N.N. Bogoliubov, Sov. Phys. Usp. **2**, 236 (1959).
- [64] N.N. Bogoliubov, Usp. Fiz. Nauk. **67**, 549 (1959).
- [65] D.J. Thouless, Nucl. Phys. **21**, 225 (1960).
- [66] S.G. Rohoziński *et al.*, in preparation.
- [67] A. Messiah, *Quantum Mechanics* (North Holland, Amsterdam, 1961).
- [68] P.O. Löwdin, Phys. Rev. **97**, 1474 (1955).

- [69] D. Van Neck, M. Waroquier, and K. Heyde, Phys. Lett. **B314**, 255 (1993).
- [70] A.N. Antonov, P.E. Hodgson, and I.Z. Petkov, *Nucleon correlations in nuclei* (Springer, New York 1993).
- [71] A.N. Antonov, D.N. Kadrev, and P.E. Hodgson, Phys. Rev. **C50**, 164 (1994).
- [72] A.N. Antonov, S.S. Dimitrova, M.K. Gaidarov, M.V. Stoitsov, M.E. Grypeos, S.E. Massen, and K.N. Ypsilantis, Report No. nucl-th/9511006.
- [73] A. Polls, H. Mütter, and W.H. Dickhoff, Nucl. Phys. **A594**, 117 (1995).
- [74] A.L. Goodman, Adv. Nucl. Phys. **11**, 263 (1979).
- [75] L.P. Gor'kov, Sov. Phys. JETP **7**, 505 (1958).
- [76] N. Fukunishi, T. Otsuka, and I. Tanihata, Phys. Rev. **C48**, 1648 (1993).
- [77] J. Dobaczewski, I. Hamamoto, W. Nazarewicz, and J.A. Sheikh, Phys. Rev. Lett. **72**, 981 (1994).
- [78] F. De Blasio and G. Lazzari, Nuovo Cimento **107A**, 1579 (1994).
- [79] V.E. Starodubsky. Sov. J. Nucl. Phys. **54**, 19 (1991).
- [80] V.E. Starodubsky and M.V. Zverev, Phys. Lett. **B276**, 269 (1992).
- [81] J. Terasaki, P.-H. Heenen, H. Flocard, and P. Bonche, to be published, 1995.
- [82] J. Dobaczewski and W. Nazarewicz, Phys. Rev. **C51**, R1070 (1995).
- [83] H. Lenske, Proc. 6th Intern. Conf. on Nuclei Far from Stability, Bernkastel-Kues, Germany, eds. R. Neugart, A. Wöhr, p.381 (1993).
- [84] W. Schwab, H. Geissel, H. Lenske, K.-H. Behr, A. Brunle, K. Burkard, H. Irnich, T. Kobayashi, G. Kraus, A. Magel, G. Munzenberg, F. Nickel, K. Riisager, C. Scheidenberger, B.M. Sherrill, T. Suzuki, and B. Voss, Z. Phys. **A350**, 283 (1995).
- [85] J.R. Bennett, J. Engel, and S. Pittel, Report No. nucl-th/9509028.
- [86] F. Tondeur, Nucl. Phys. **A315**, 353 (1979).
- [87] R.C. Nayak and J.M. Pearson, Phys. Rev. **C52**, 2254 (1995).
- [88] W.-T. Chou, R.F. Casten, and N.V. Zamfir, Phys. Rev. **C51**, 2444 (1995).
- [89] P. Haensel, J.L. Zdunik, and J. Dobaczewski, Astron. Astrophys. **222**, 353 (1989).
- [90] B. Pfeiffer, K.-L. Kratz, J. Dobaczewski and P. Möller, Acta Phys. Pol. (in press).
- [91] K.-L. Kratz, J.-P. Bitouzet, F.-K. Thielemann, P. Möller, and B. Pfeiffer, Astrophys. J. **403** (1993) 216.
- [92] J. Mougey, M. Bernheim, A. Bussière, A. Gillebert, Phan Xuan Hô, M. Priou, D. Royer, I. Sick, and G.J. Wagner, Nucl. Phys. **A262**, 461 (1976).
- [93] J.W.A. den Herder, H.P. Blok, E. Jans, P.H.M. Keizer, L. Lapikás, E.N.M. Quint, G. van der Steenhoven, and P.K.A. de Witt Huberts, Nucl. Phys. **A490**, 507 (1988).
- [94] S. Galès, Ch. Stoyanov, and A.I. Vdovin, Phys. Rep. **166**, 125 (1988).
- [95] D. Van Neck, M. Waroquier, V. Van der Sluys, and K. Heyde, Nucl. Phys. **A563**, 1 (1993).
- [96] C.H. Dasso, G. Pollaro, and A. Winther, Phys. Rev. Lett. **73**, 1907 (1994).
- [97] K.-H. Kim, T. Otsuka, and M. Tohyama, Phys. Rev. **C50**, R566 (1994).
- [98] C.H. Dasso and G. Pollaro, Phys. Lett. **155B**, 223 (1985).
- [99] D.R. Bes, P. Lotti, E. Maglione, and A. Vitturi, Phys. Lett. **169B**, 5 (1986).
- [100] C.H. Dasso, E. Maglione, and G. Pollaro, Nucl. Phys. **A500**, 127 (1989).
- [101] O. Civitarese, A. Faessler, and M.C. Licciardo, Z. Phys. **A341**, 261 (1992).
- [102] P. Lubiński, J. Jastrzębski, A. Grochulska, A. Stolarz, A. Trzcińska, W. Kurcewicz, F.J. Hartmann, W. Schmid, T. von Egidy, J. Skalski, R. Smolańczuk, S. Wycech, D.

- Hilscher, D. Polster, and H. Rossner, Phys. Rev. Lett. **73**, 3199 (1994).
- [103] S. Wycech, J. Skalski, R. Smolańczuk, J. Dobaczewski, and J.R. Rook, Nucl. Phys. (submitted).
- [104] Y.M. Engel, D.M. Brink, K. Goeke, S.J. Krieger, and D. Vautherin, Nucl. Phys. **A249**, 215 (1975).
- [105] J.-F. Berger, M. Girod, and D. Gogny, Comp. Phys. Comm. **63**, 365 (1991).
- [106] M. Brack, T. Lederberger, H.C. Pauli, and A.S. Jensen, Nucl. Phys. **A234**, 185 (1974).
- [107] D.G. Madland and R. Nix, Nucl. Phys. **A476**, 1 (1988).
- [108] A.S. Jensen and A. Miranda, Nucl. Phys. **A449**, 331 (1986).
- [109] N.K. Kuzmenko and V.M. Mikhajlov, Phys. Lett. **B322**, 301 (1994).

TABLES

TABLE I. Results of the HFB calculations with SkP force for the $s_{1/2}$ neutrons in ^{120}Sn . For the n th quasiparticle state, E_n^{HFB} and N_n are the quasiparticle energy and the norm of the lower component, respectively. For the μ th canonical-basis state, v_μ^2 is the occupation probability, ϵ_μ and Δ_μ are, respectively, the average values of the p-h and p-p mean-field Hamiltonians [Eq. (4.22)] and E_μ^{can} is the BCS-like quasiparticle energy defined in Eq. (4.24). All energies are in MeV.

Quasiparticle states			Canonical-basis states				
n	E_n^{HFB}	N_n	μ	E_μ^{can}	v_μ^2	ϵ_μ	Δ_μ
11	54.27	0.0001	11	47.27	0.0	39.32	-0.37
10	44.38	0.0001	10	78.07	0.0	70.12	-0.03
9	35.44	0.0006	9	73.14	0.0	65.20	-0.81
7	27.49	0.0008	8	54.84	0.0	46.89	0.13
6	20.82	0.0019	7	55.22	0.000003	47.27	0.07
4	15.58	0.0008	6	62.46	0.00003	54.51	-0.76
3	11.61	0.0006	5	38.44	0.0001	30.48	0.76
2	8.92	0.0002	4	20.50	0.0005	12.54	0.99
1	1.54	0.8372	3	2.36	0.8362	-9.88	1.35
5	17.60	0.9942	2	20.06	0.9990	-27.96	1.27
8	31.64	0.9992	1	29.94	0.9999	-37.88	0.45

FIGURES

FIG. 1. Self-consistent spherical neutron densities $\rho_N(r)$ calculated with the SkP, SIII $^\delta$, and D1S interactions for selected tin isotopes across the β -stability valley.

FIG. 2. Self-consistent spherical neutron pairing densities $\tilde{\rho}_N(r)$ calculated with the SkP, SkP $^\delta$, and D1S interactions for selected tin isotopes across the β -stability valley.

FIG. 3. Self-consistent spherical local neutron potentials $U_N(r)$ calculated with the SkP, SIII $^\delta$, and D1S interactions for selected tin isotopes across the β -stability valley.

FIG. 4. Self-consistent spherical local neutron pairing potentials $\tilde{U}_N(r)$ calculated with the SkP and SkP $^\delta$ interactions for selected tin isotopes across the β -stability valley.

FIG. 5. The self-consistent HFB+SkP mass parameters M and \tilde{M} , and potentials U and \tilde{U} (central parts only), for neutrons in ^{120}Sn .

FIG. 6. The HFB+SkP radial wave functions $r\phi_i(E_n, r)$ of the neutron $s_{1/2}$ single-quasiparticle states in ^{120}Sn . Upper ($i=1$) and lower ($i=2$) components are plotted in the left and right columns, respectively. The numbers preceded by a times (\times) sign indicate the scaling factors for the small wave function components.

FIG. 7. The HFB+SkP radial canonical-basis wave functions $r\check{\phi}_\mu(r)$ of the neutron $s_{1/2}$ single-particle states in ^{120}Sn .

FIG. 8. Same as in Fig. 6, but for the HF+BCS approach.

FIG. 9. Weakly bound and unbound self-consistent single-neutron HF+SkP energies $\epsilon_{n\ell j}^{\text{HF}}$ for ^{150}Sn as function of R_{box} . Top and bottom panels show states of positive and negative parity, respectively.

FIG. 10. Same as in Fig. 9, but for the canonical energies $\epsilon_{n\ell j}$, Eq. (4.22a).

FIG. 11. Self-consistent single-quasineutron HFB+SkP energies $E_{n\ell j}^{\text{HFB}}$ (top panel) compared with the BCS-like canonical single-quasineutron energies $E_{n\ell j}^{\text{can}}$ (Eq. (4.24)) (bottom panel) for the tin isotopes.

FIG. 12. The HFB+SkP spectral amplitudes $\mathcal{S}_{n\mu}$ (5.9) of the canonical $s_{1/2}$ states in ^{120}Sn with $\mu=1-5$. The corresponding canonical energy ϵ_μ is given in MeV and the occupation probability v_μ^2 is displayed in parentheses. All the amplitudes $\mathcal{S}_{n\mu}$ for $\mu=1$ have been assumed to be positive. This defines the relative phases of the spectral amplitudes for $\mu>1$ (shown by bars hashed in opposite directions). For $E < -\lambda$ the quasiparticle spectrum is discrete, while for $E > -\lambda$ it is represented by the discretized continuum.

FIG. 13. Same as in Fig. 12, but for ^{150}Sn . No discrete states appear for $E < -\lambda$.

FIG. 14. Same as in Fig. 12, but for the $\mu=1-3$ canonical $f_{7/2}$ states.

FIG. 15. Same as in Fig. 14, but for ^{150}Sn .

FIG. 16. The self-consistent HFB+SkP single-neutron density $\rho_N(r)$ in ^{150}Sn (in logarithmic scale) calculated with different values of R_{box} . The inset shows the same data in linear scale. The shaded line shows the asymptotic behavior given by Eq. (5.14a).

FIG. 17. Same as in Fig. 16, but for the neutron pairing density $\tilde{\rho}_N(r)$. The shaded line shows the asymptotic behavior given by Eq. (5.14b).

FIG. 18. Self-consistent HFB+SkP neutron pairing potentials $\tilde{U}(r)$ in ^{150}Sn (top panel) and ^{172}Sn (bottom panel) calculated with four values of R_{box} . The corresponding average gap values $\langle\Delta\rangle$ [Eq. (4.6)] are indicated.

FIG. 19. Neutron rms radius r_N (top panel), average pairing gap $\langle\Delta_N\rangle$ (middle panel), and the Fermi energy λ_N (bottom panel) calculated in the HFB+SkP model for ^{150}Sn (full circles) and ^{172}Sn (open circles) as functions of R_{box} .

FIG. 20. Neutron densities $\rho_N(r)$ (in logarithmic scale) calculated in the HFB+SkP and HFB+D1S models for ^{132}Sn , ^{150}Sn , and ^{172}Sn .

FIG. 21. Same as Fig. 19 for the D1S interaction, but as a function of the number of oscillator shells N_{sh} . For every N_{sh} the oscillator-basis frequency ω_0 is adjusted as described in the text.

FIG. 22. Same as in Fig. 16, but for the HF+BCS+ $\langle\Delta\rangle$ approach with the constant pairing gaps as listed in Fig. 18 (top panel), the HF+BCS+SkP $^\delta$ model (middle panel), and the HF+BCS+SkP model (bottom panel). In all these calculations the same pairing space (i.e., energy cut-off) was used as in Fig. 16.

FIG. 23. Average values of the neutron p-h and p-p potentials, $\epsilon_{n\ell j}$ and $\Delta_{n\ell j}$ [Eqs. (4.22)] in the canonical states calculated for ^{120}Sn in HFB+D1S (top), HFB+SkP $^\delta$ (middle), and HFB+SkP (bottom) model. Only the states with $v_{n\ell j}^2 > 0.0001$ are displayed.

FIG. 24. Same as in Fig. 23, but for ^{150}Sn .

FIG. 25. Average neutron pairing gaps $\langle\Delta_N\rangle$ [Eq. (4.6)] calculated for SkP (solid), SIII $^\delta$ (dashed), and D1S (dotted) interactions for the series of tin isotopes.

FIG. 26. Sequences of nuclear single-particle levels for various potentials. Orbitals are labeled by the spherical quantum numbers. From left to right: (i) shell structure for a potential with spin-orbit term but with a very diffuse surface, (ii) the $N_{\text{osc}}=4$ and 5 shells of the harmonic oscillator potential, (iii) no spin-orbit term, leading to a degenerate spin-orbit pattern as observed in, e.g., hypernuclei, and (iv) shell structure characteristic of nuclei near the stability valley.

FIG. 27. Two-neutron separation energies for the $N=80, 82, 84$, and 86 spherical even-even isotones calculated in the HFB+SkP model as a function of \bar{N}/Z (lower scale, $\bar{N}=83$) or Z (upper scale). The arrows indicate the proximity of neutron and proton drip lines – see Fig. 28 for detailed predicted positions of two-particle drip lines.

FIG. 28. Plot of the two-neutron separation energies S_{2n} for all particle-bound even-even nuclei with $A \geq 16$ and $N \leq 208$ calculated within the spherical HFB+SkP approach. Results for 1905 nuclei are shown using the color codes spaced by 0.4 MeV for $S_{2n} < 4 \text{ MeV}$ and by 2 MeV for $S_{2n} > 4 \text{ MeV}$.

FIG. 29. Two-neutron separation energies S_{2n} (top) and Fermi energies λ_N (bottom) for the Sn isotopes, calculated in the HFB approach with several Skyrme interactions and the Gogny-D1S interaction.

FIG. 30. Pair transfer form factor, $r^2\tilde{\rho}(r)$, calculated directly from the HFB pairing density $\tilde{\rho}(r)$ (solid lines), compared with the macroscopic form factor calculated from the derivative of the particle density $\delta\rho(r)$ (dashed lines).

FIG. 31. Pairing energies E_{pair} in the tin isotopes calculated within the HFB+SkP $^\delta$ model. Top panel shows the results for the fixed interaction strength $V_0 = -160 \text{ MeV fm}^3$ and for several cut-off energies ΔE_{max} added to the usual ℓj -dependent cut-off energy E_{max} [52]. Bottom panel shows similar results when the values of V_0 are renormalized to $-158.64, -149.57, -145.41$, and -142.01 MeV fm^3 for $\Delta E_{\text{max}}=10, 20, 30$, and 40 MeV , respectively.

FIG. 32. Same as in Fig. 31, but for the total energy relative to that obtained with $\Delta E_{\text{max}}=0$.

FIG. 33. Same as in Fig. 31, but for the effective pairing strength defined as $G_{\text{eff}} = -\langle \Delta \rangle^2 / E_{\text{pair}}$. The insert shows the renormalized strength V_0 compared with that given by Eq. (B1).

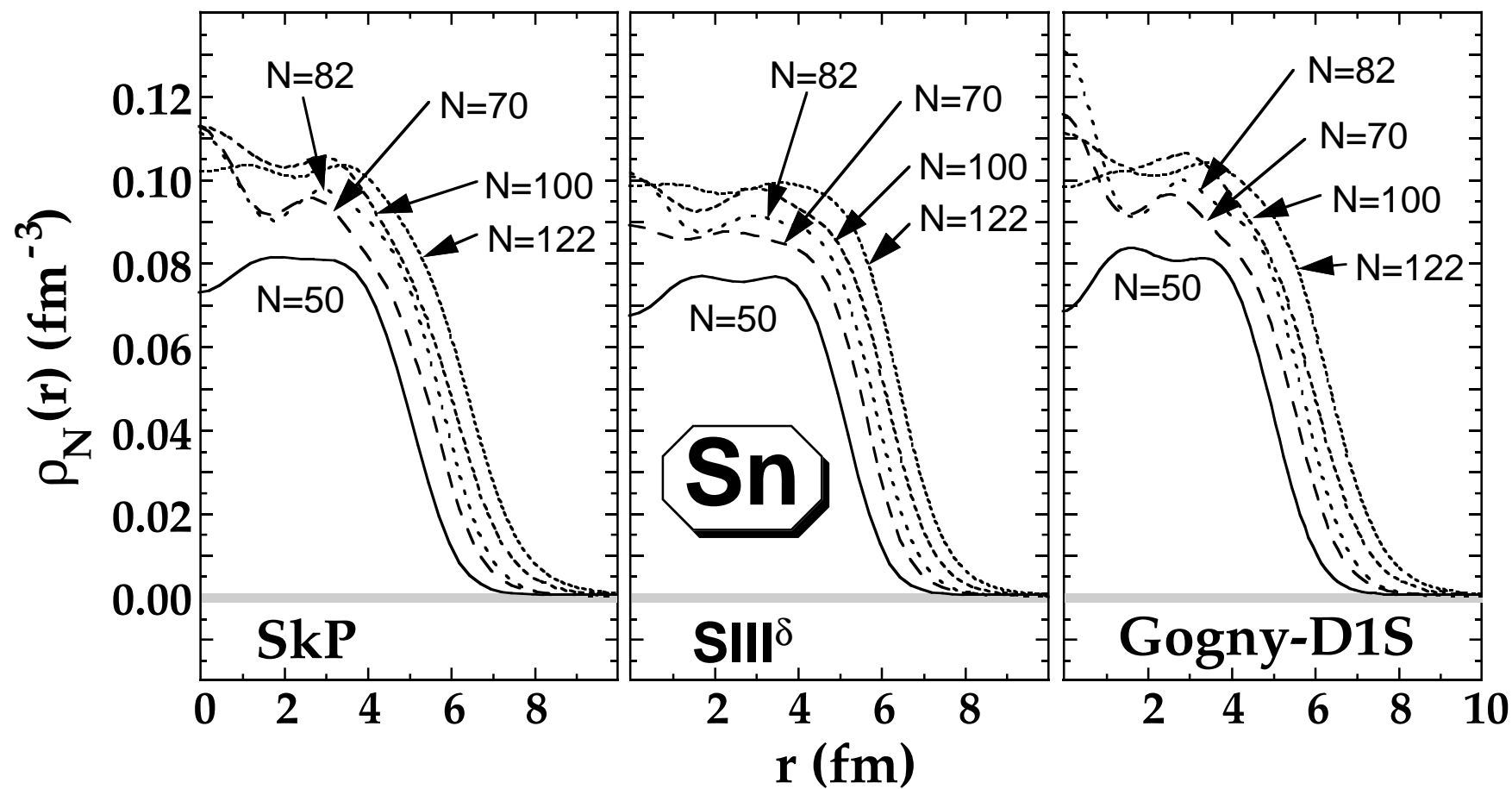


Fig. 1

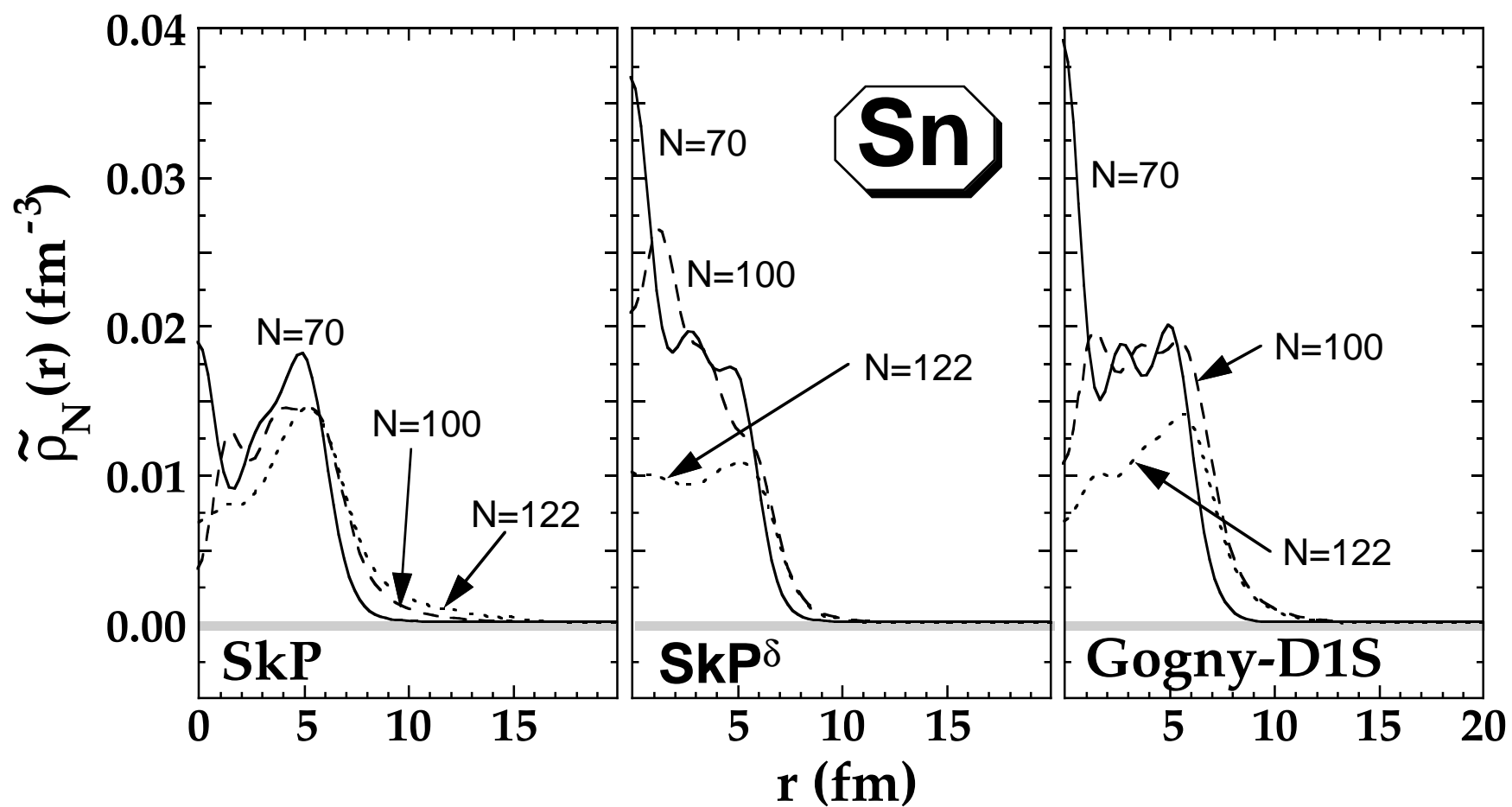


Fig. 2

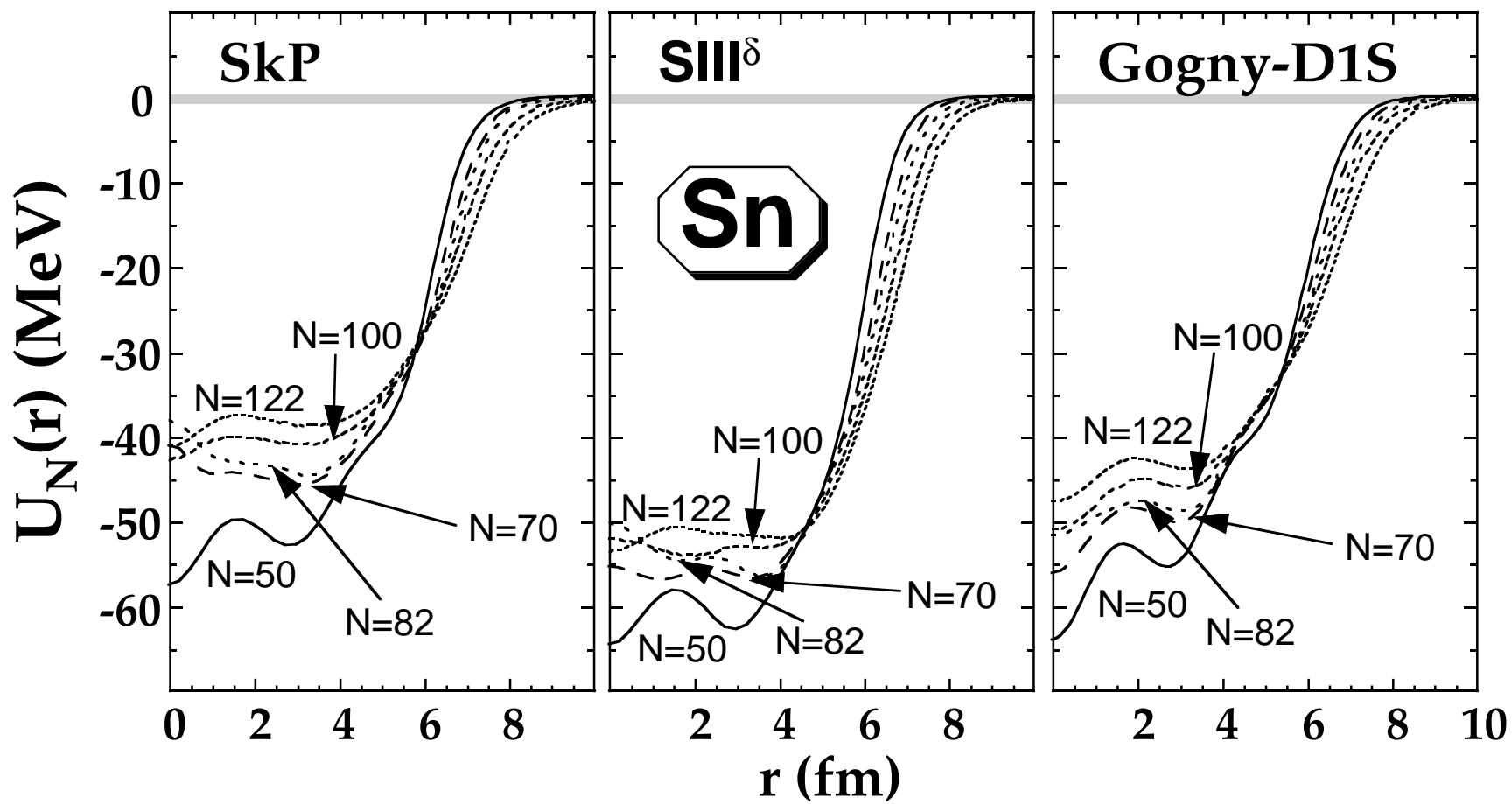


Fig. 3

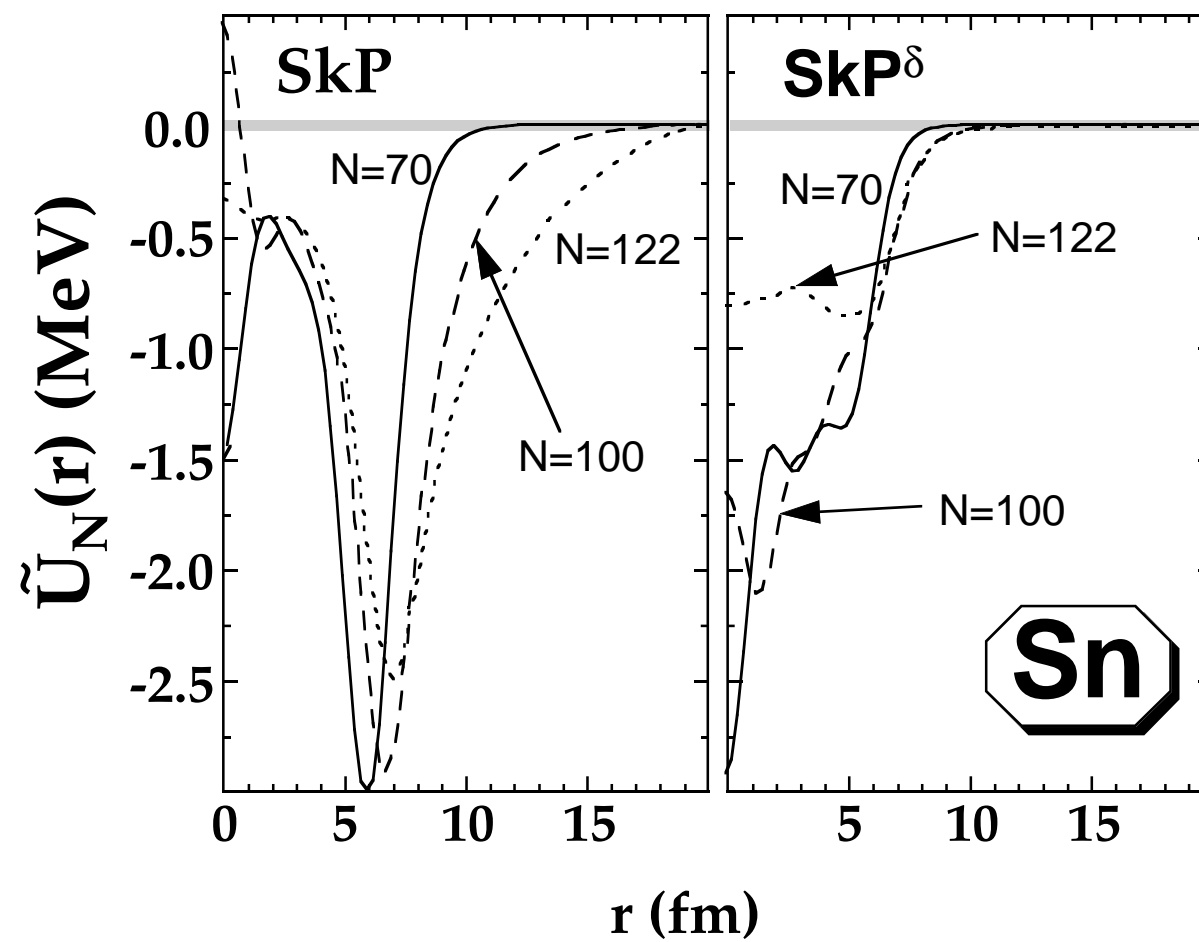


Fig. 4

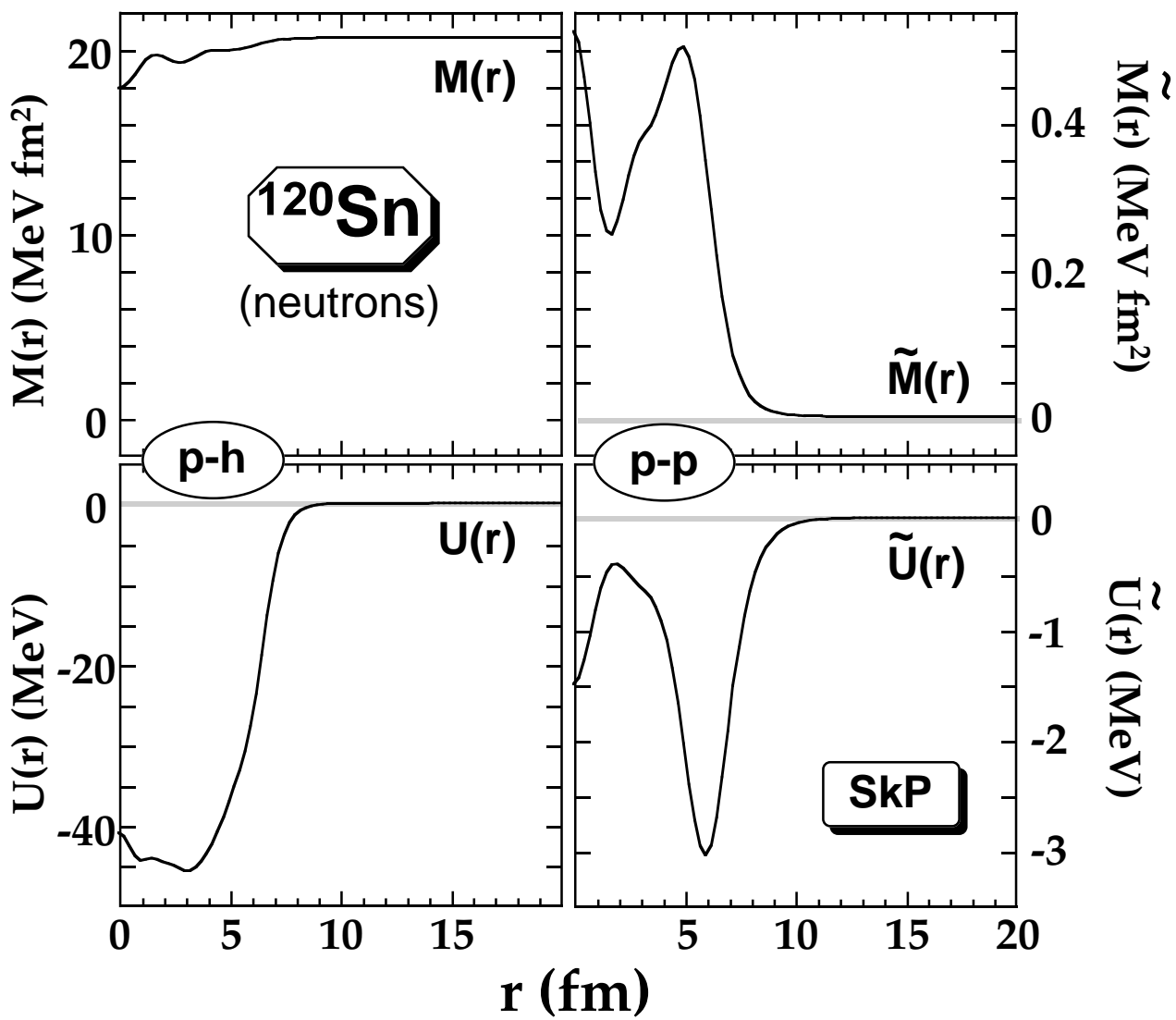


Fig. 5

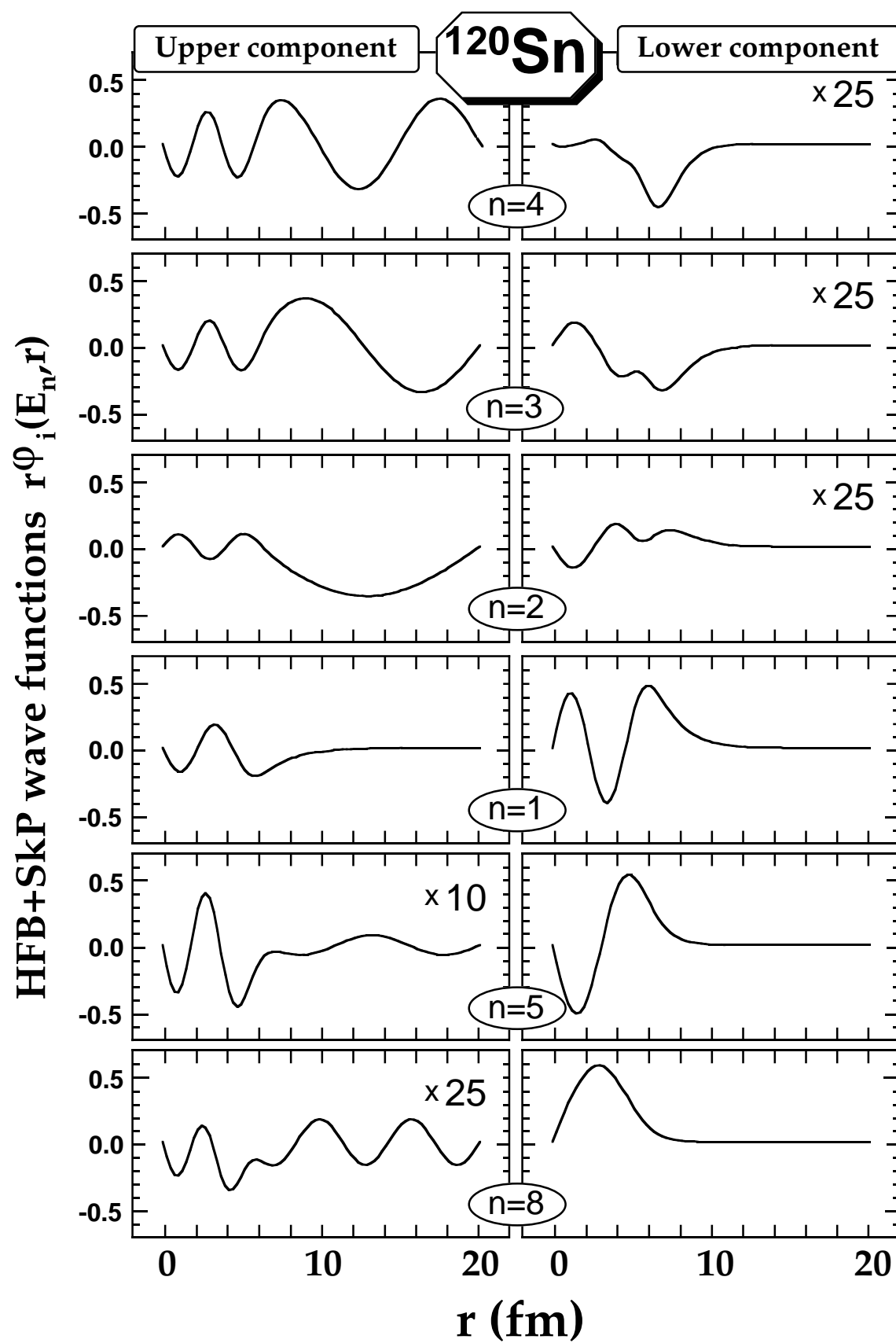


Fig. 6

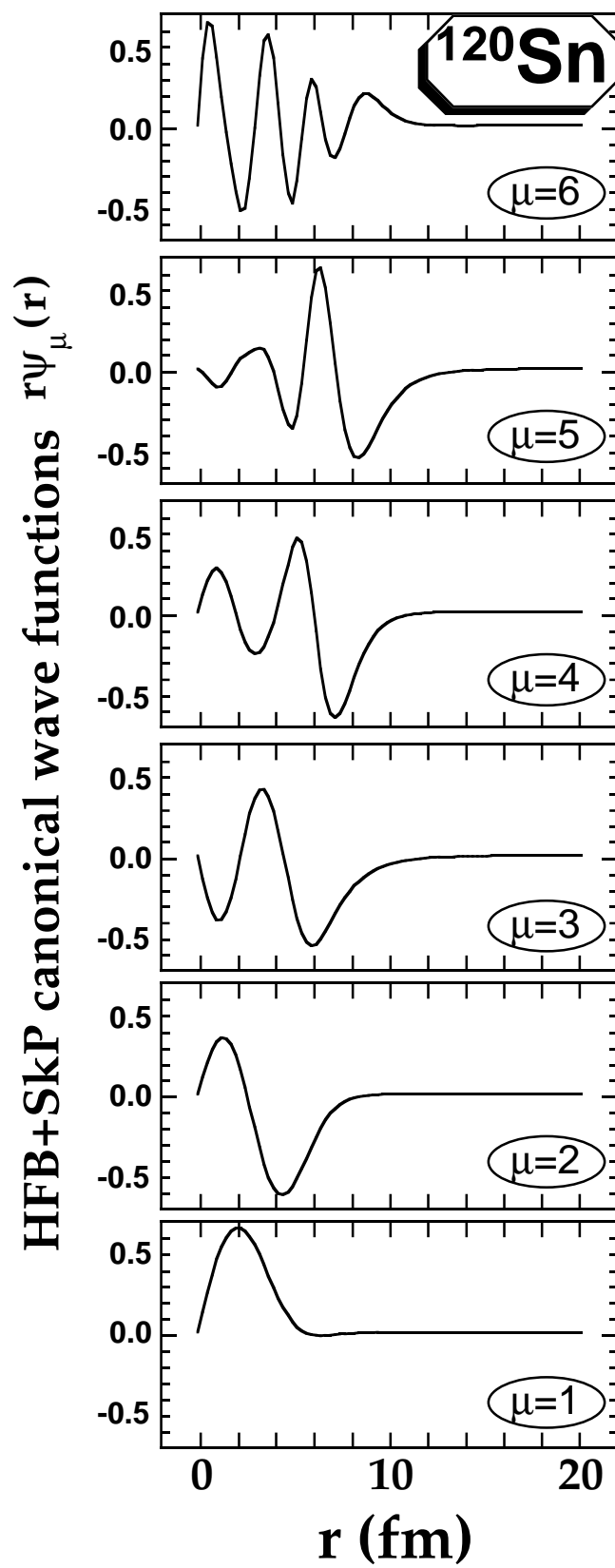


Fig. 7

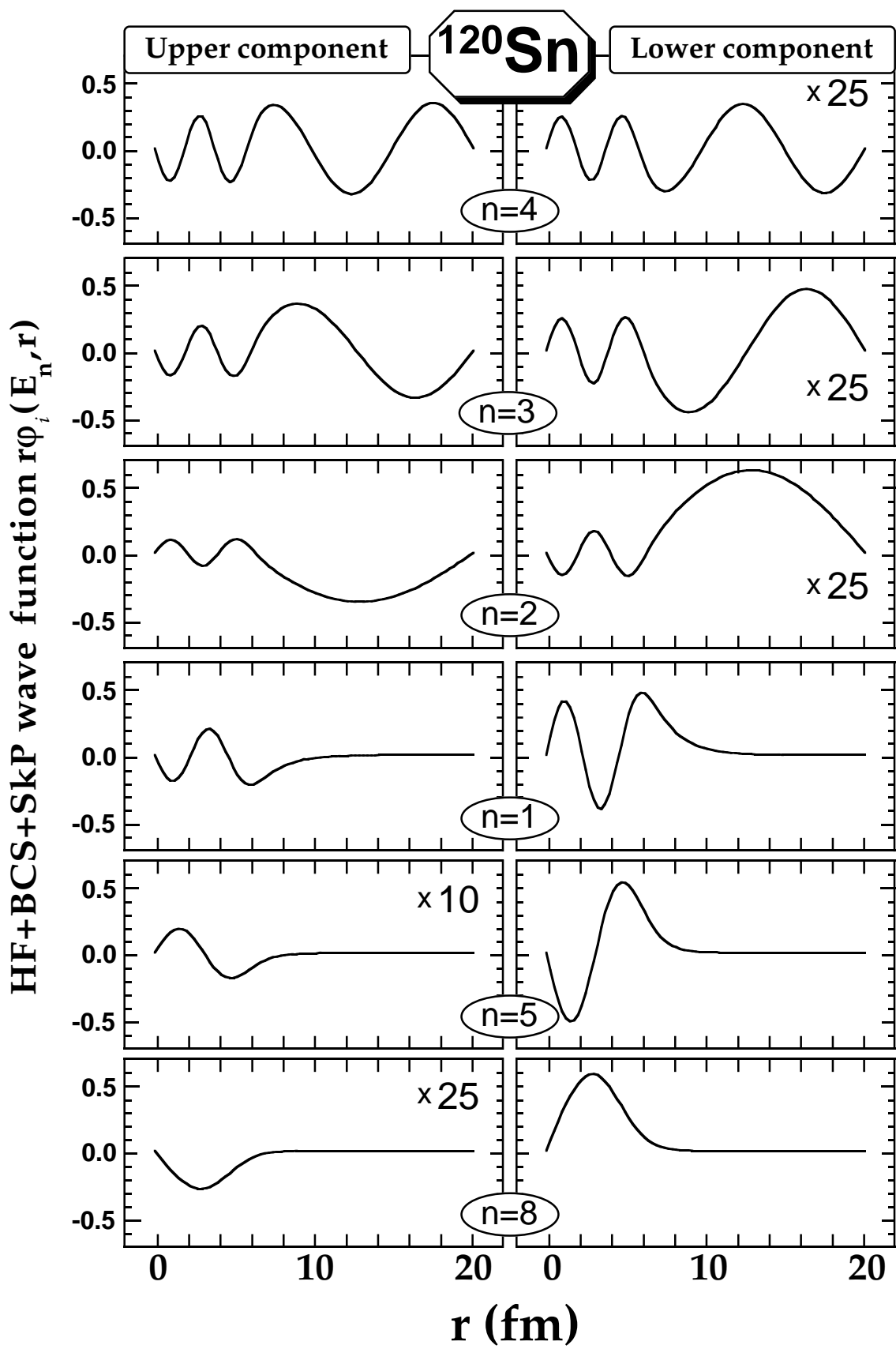


Fig. 8

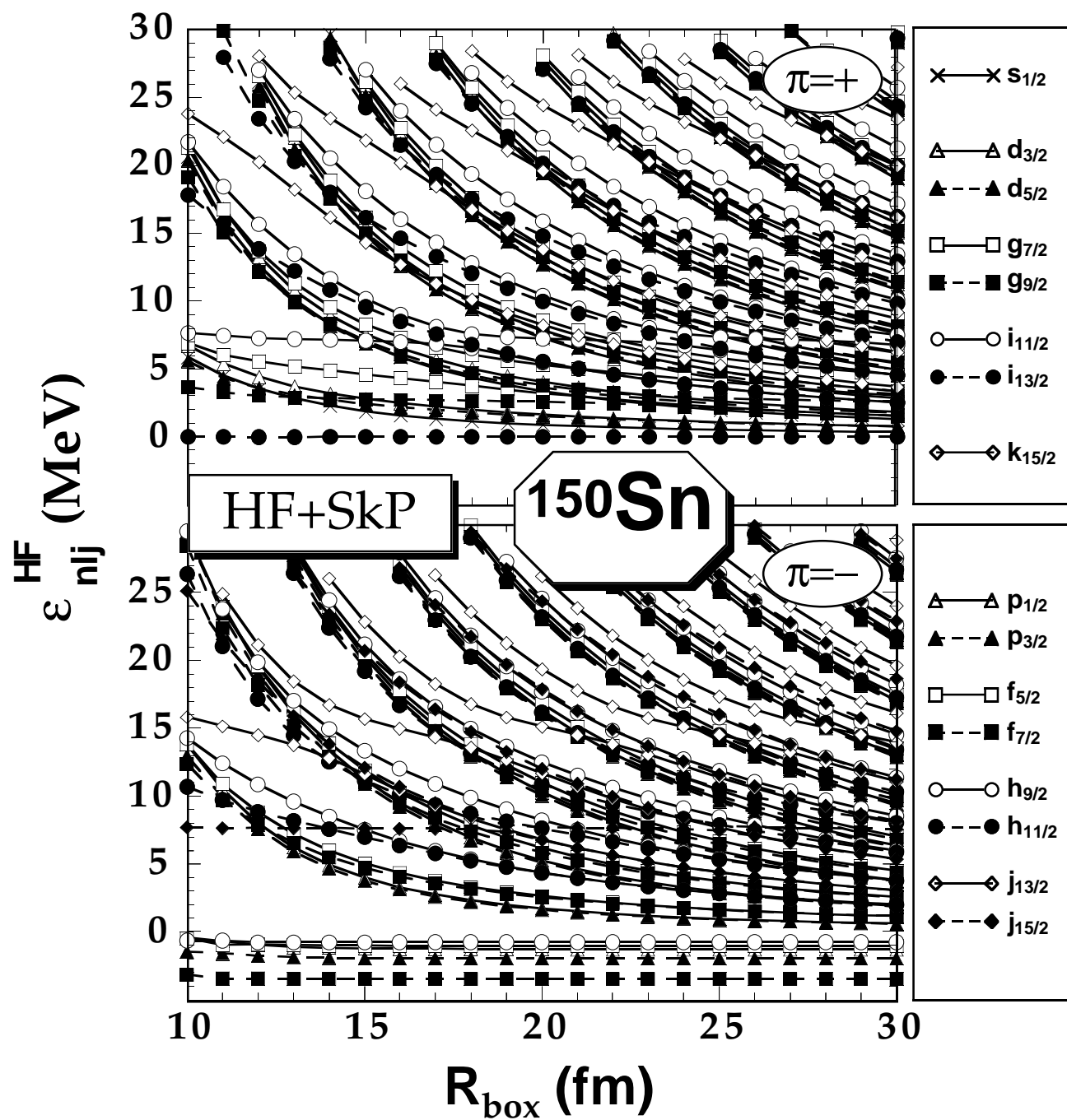


Fig. 9

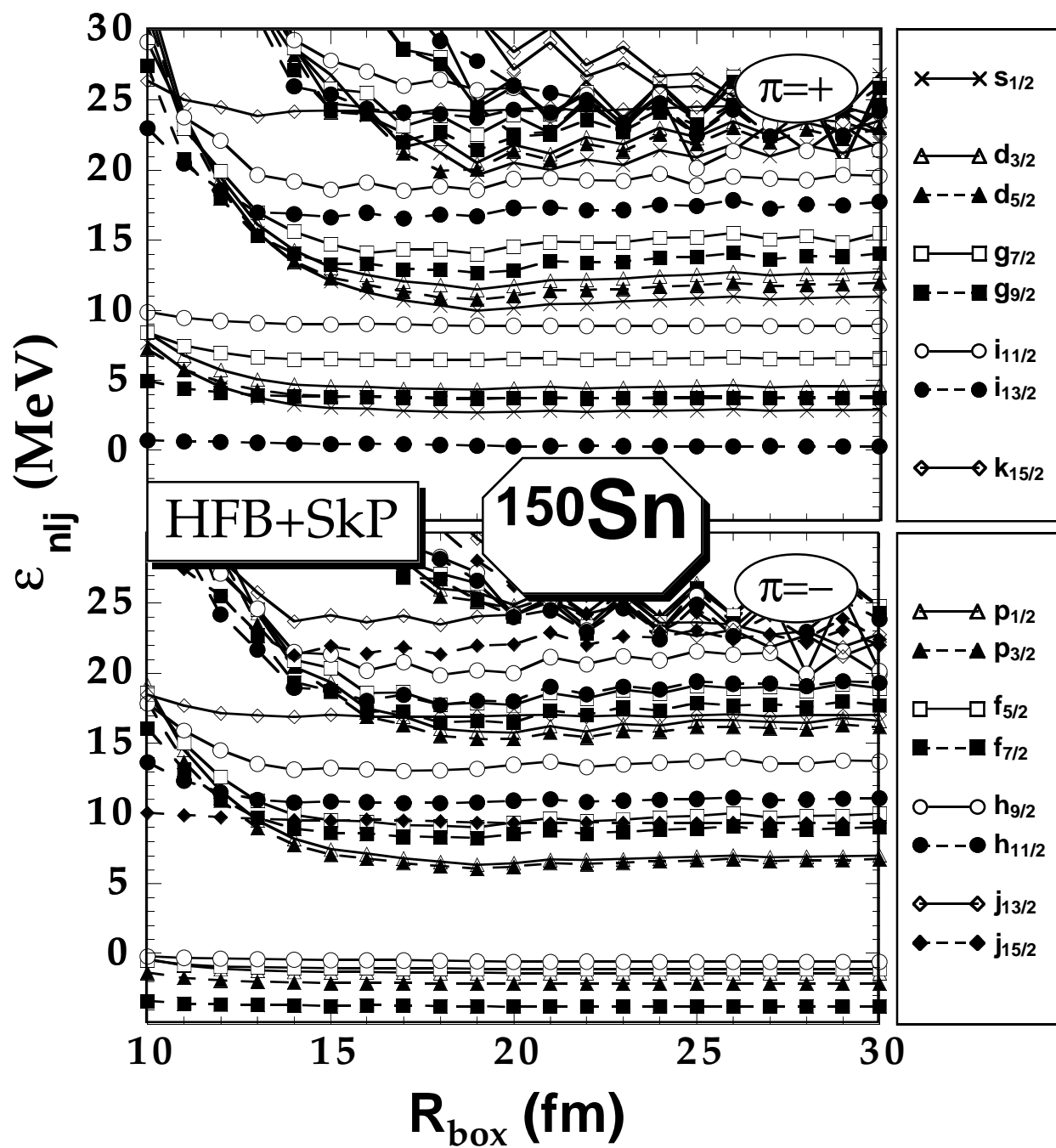


Fig. 10

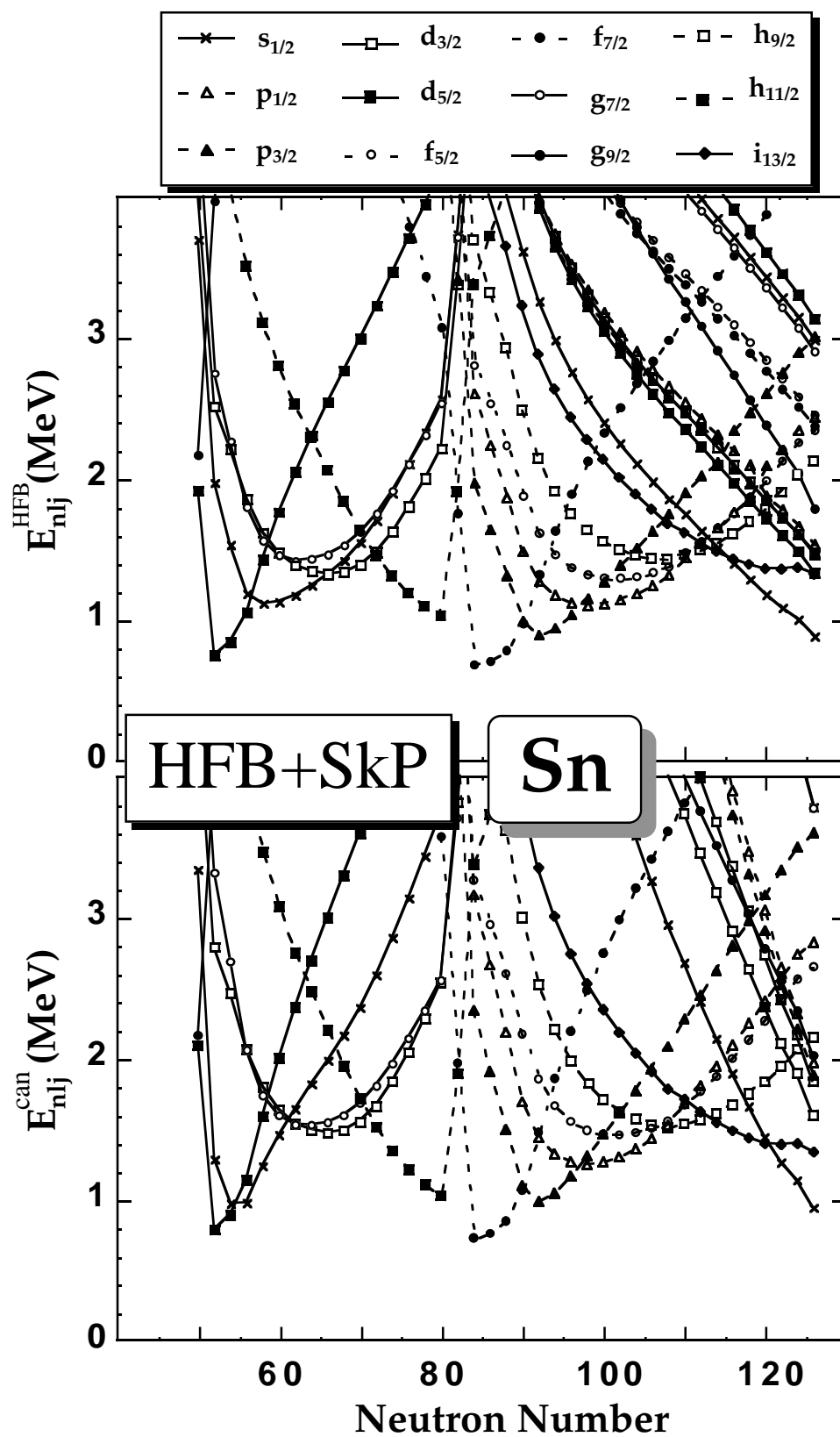


Fig. 11

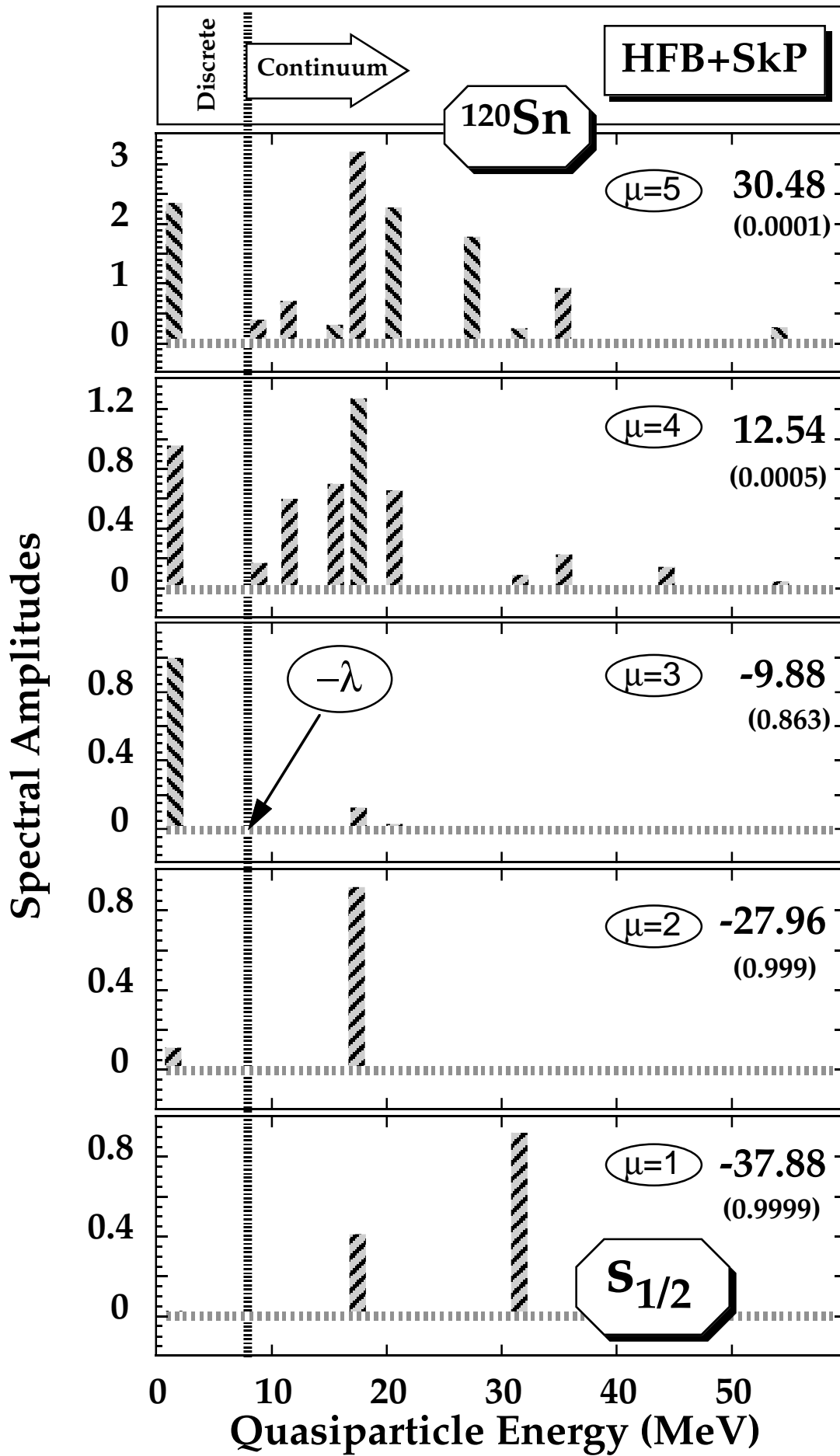


Fig. 12

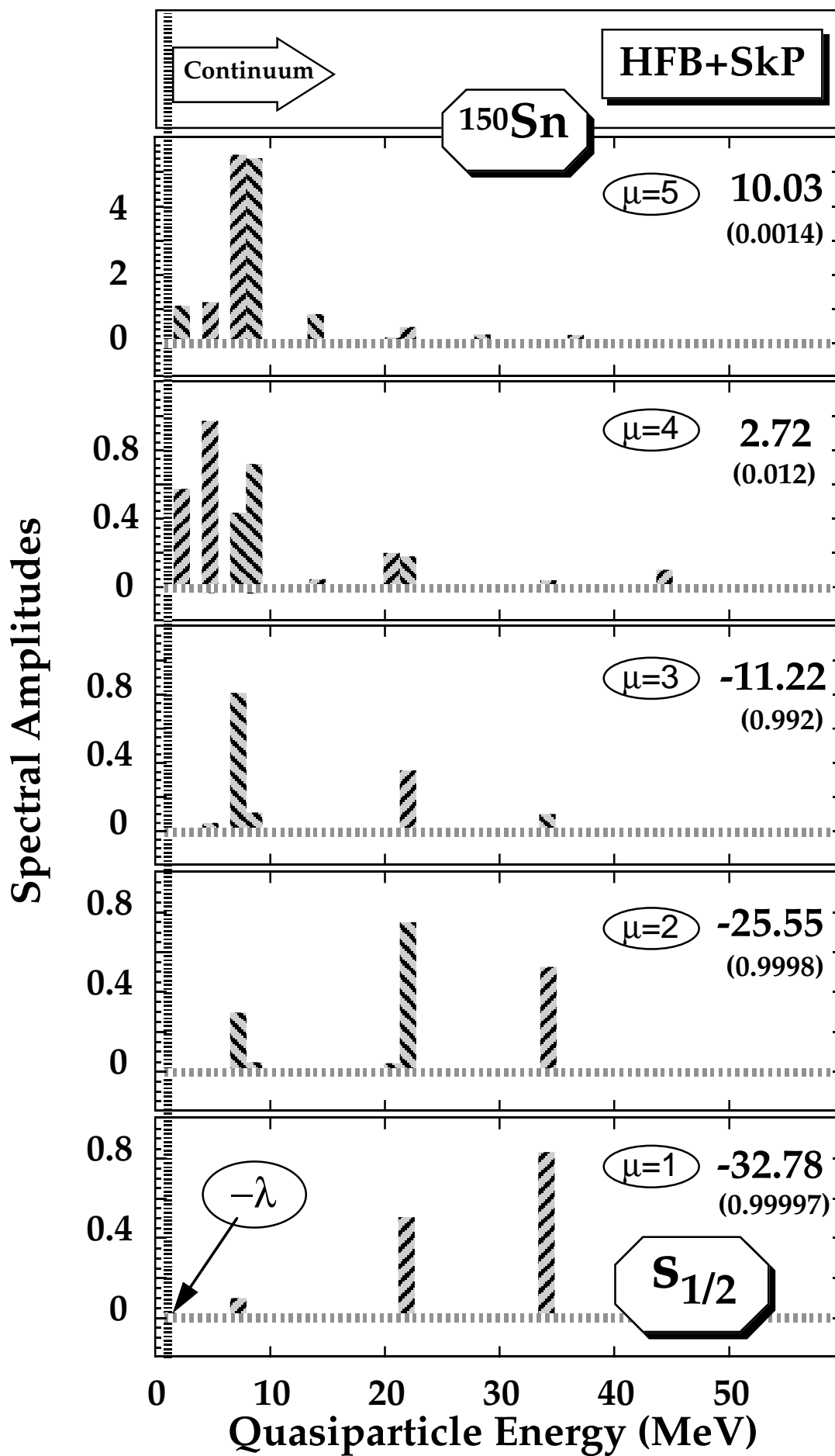


Fig. 13

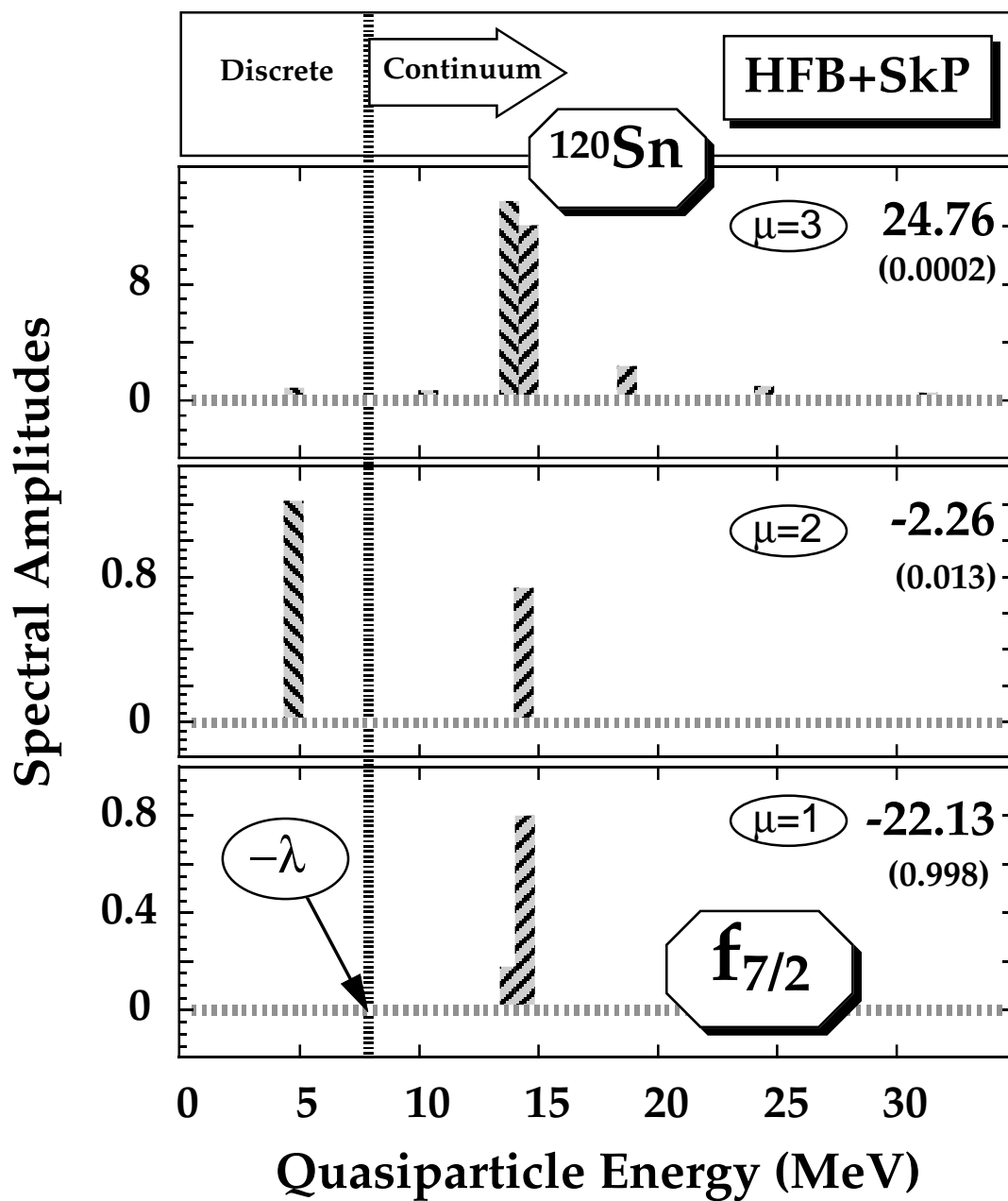


Fig. 14

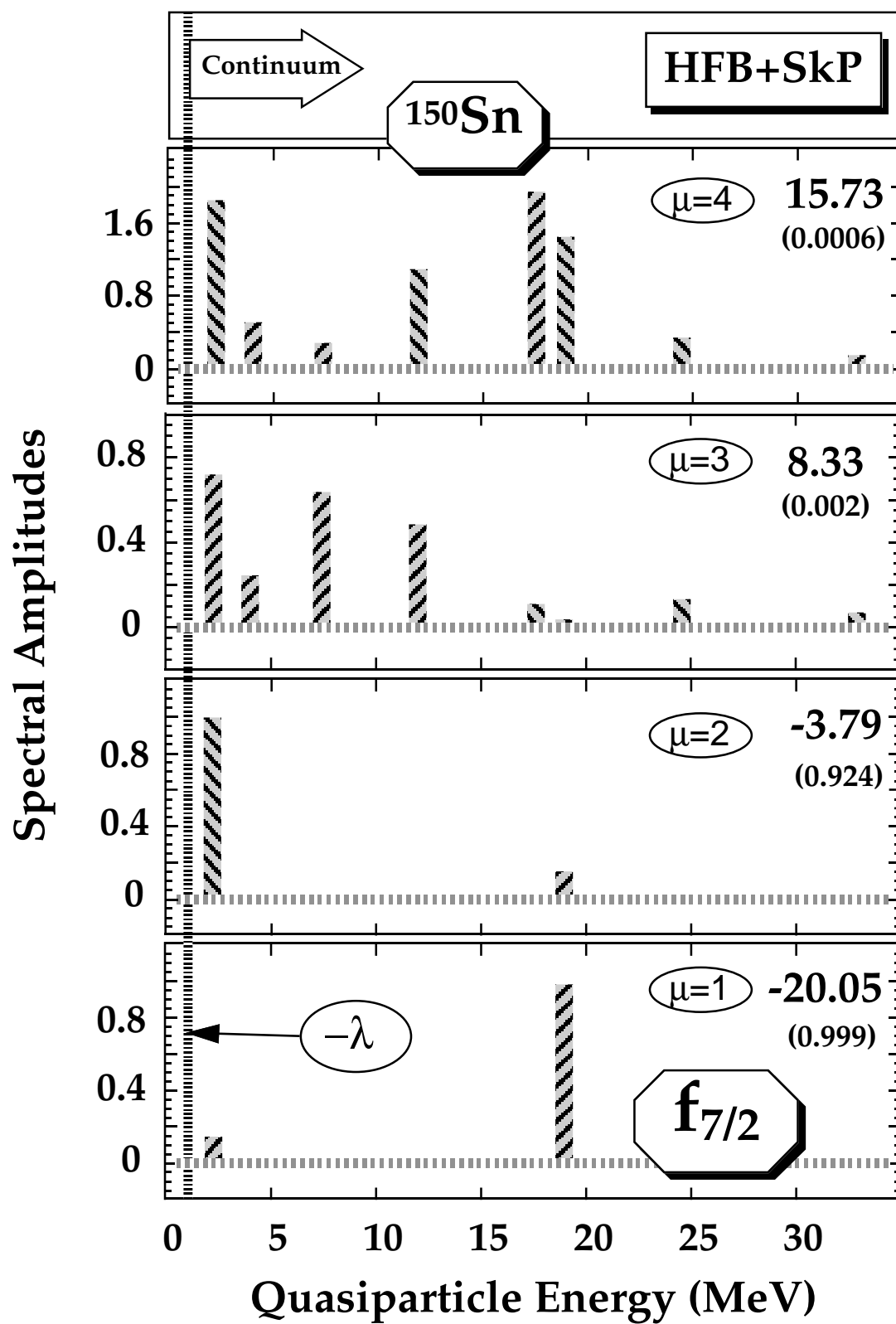


Fig. 15

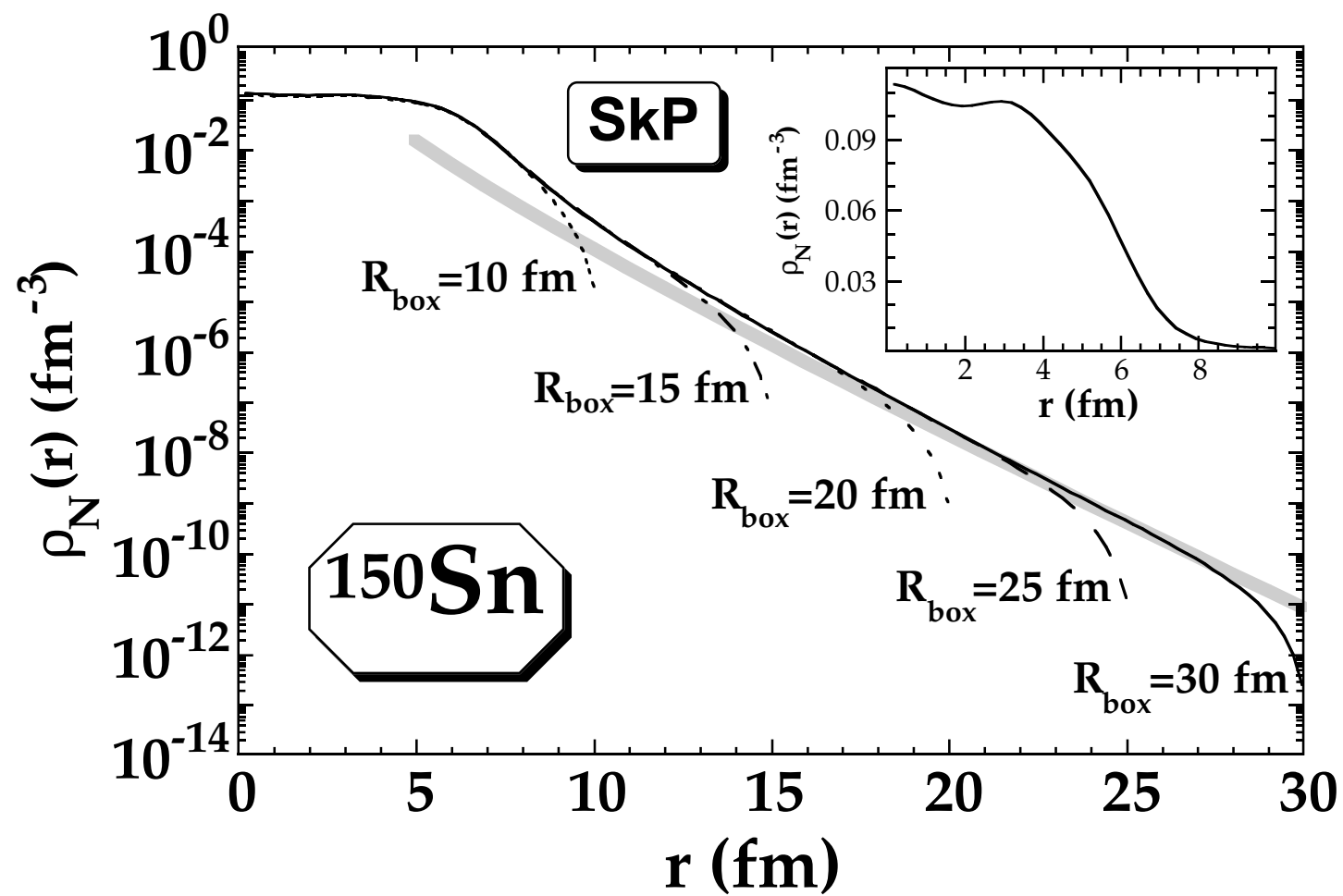


Fig. 16

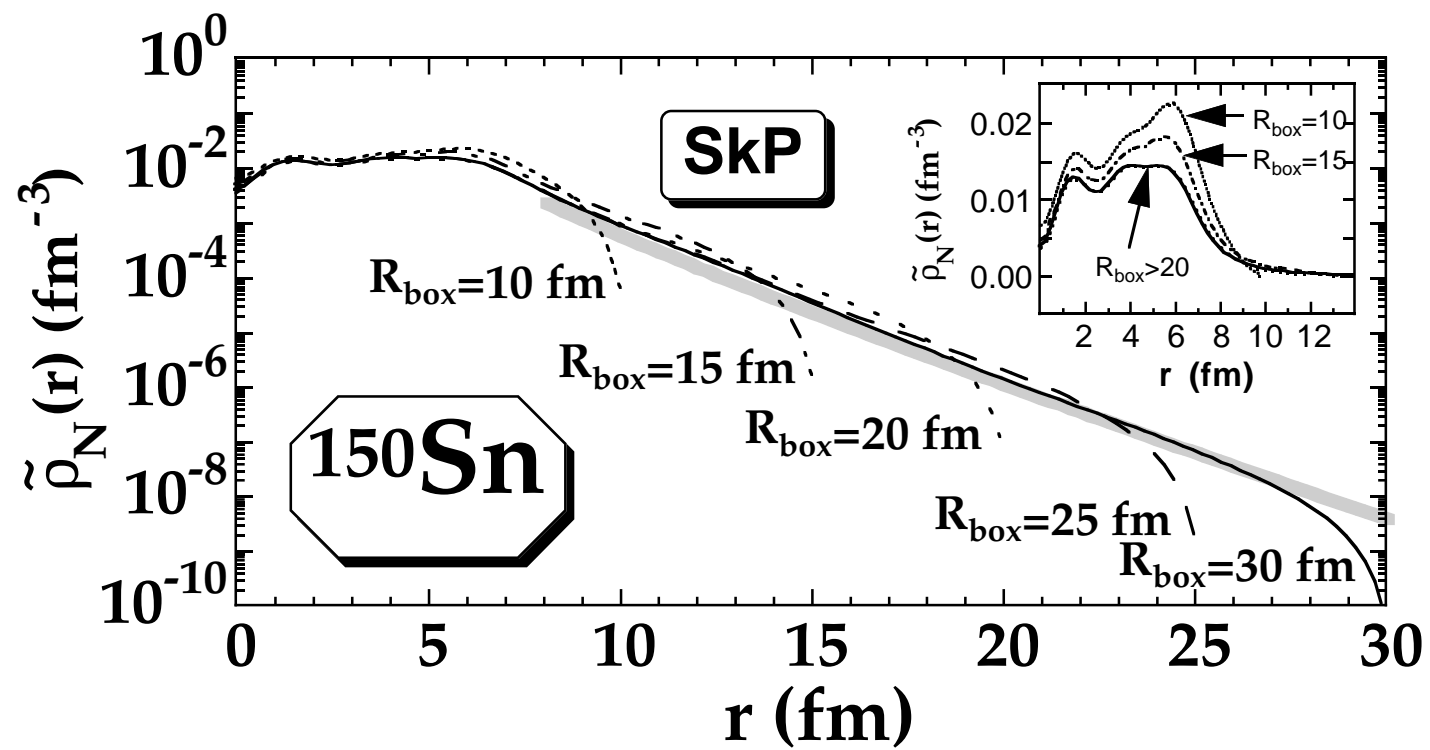


Fig. 17

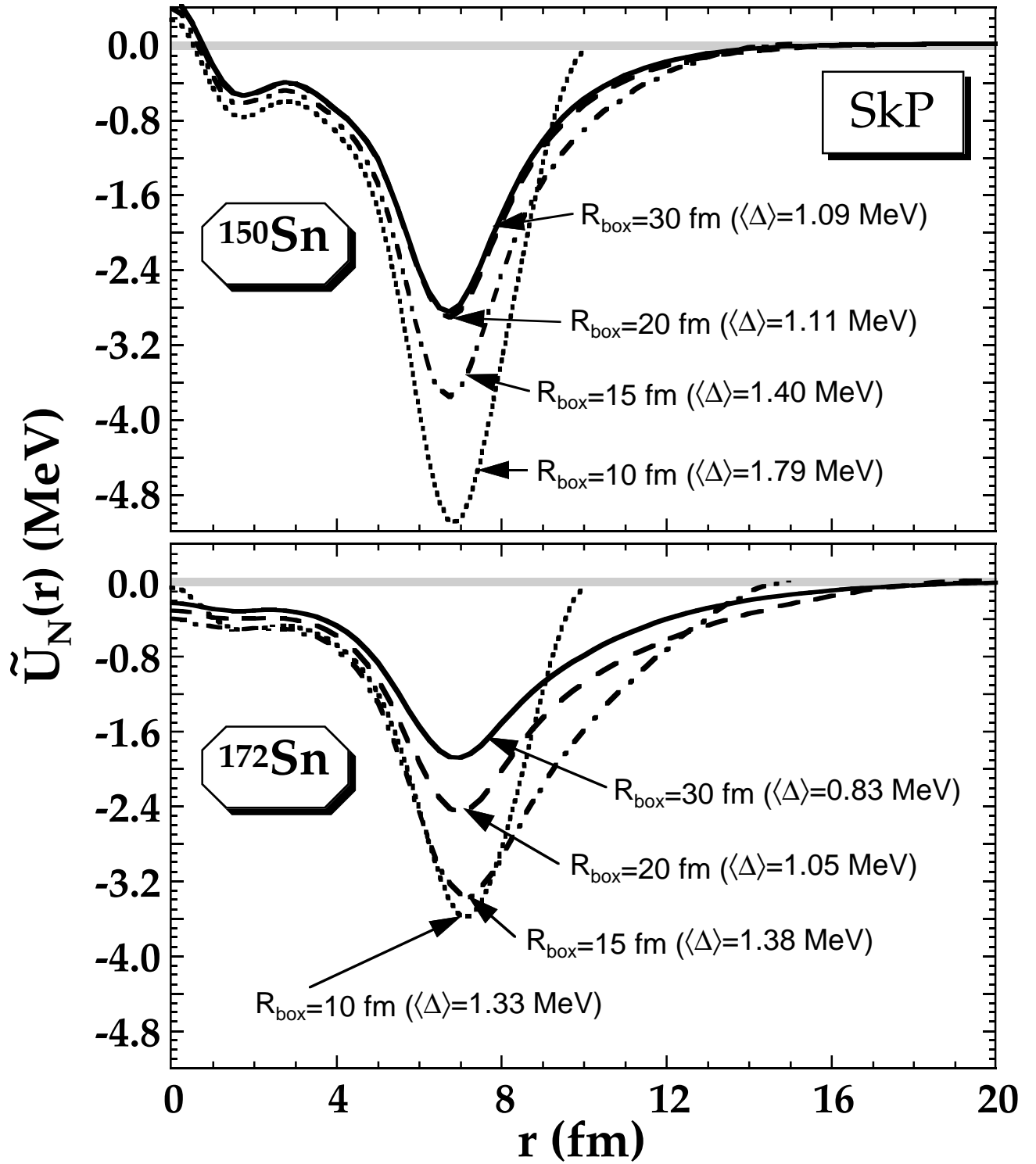


Fig. 18

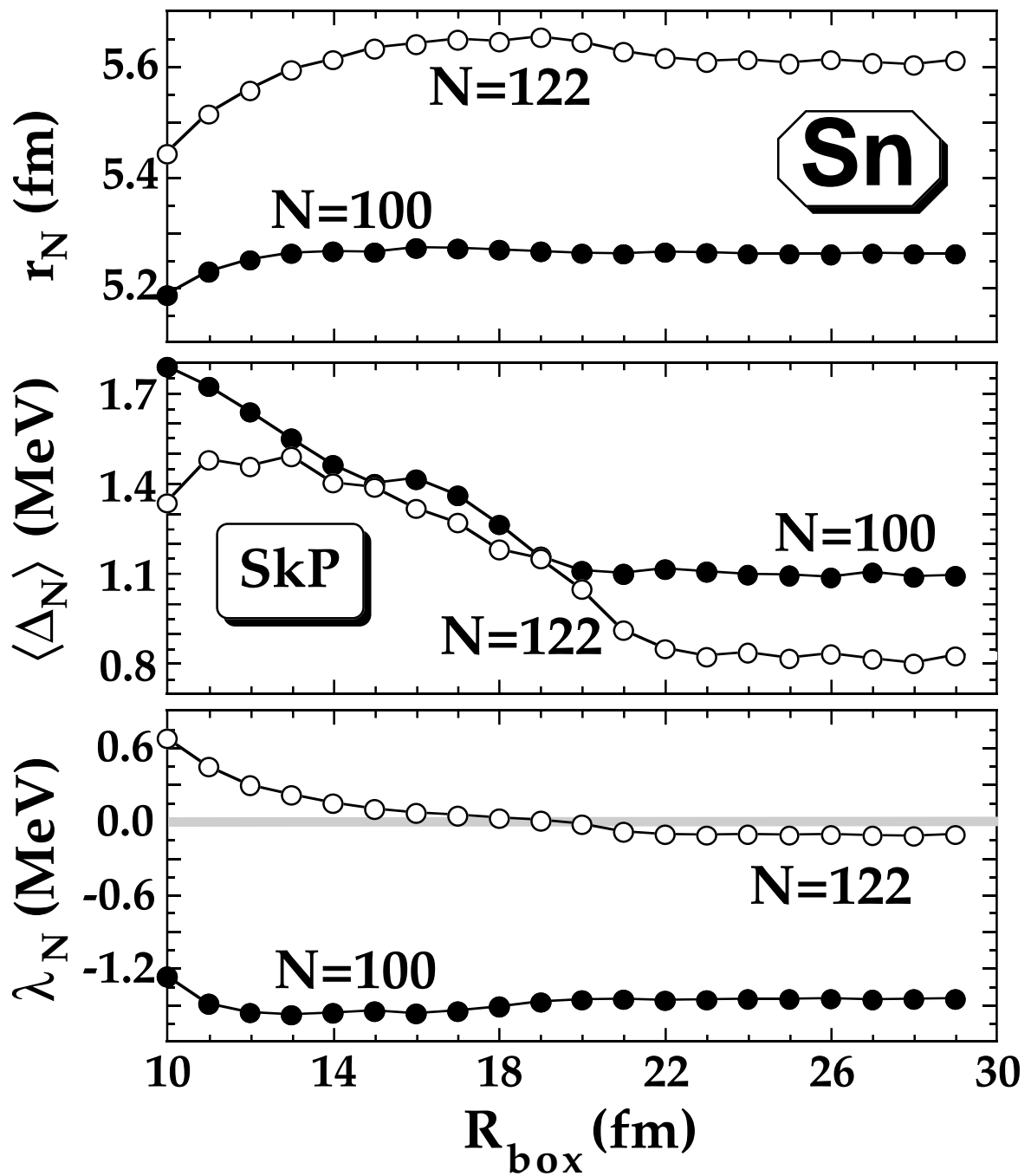


Fig. 19

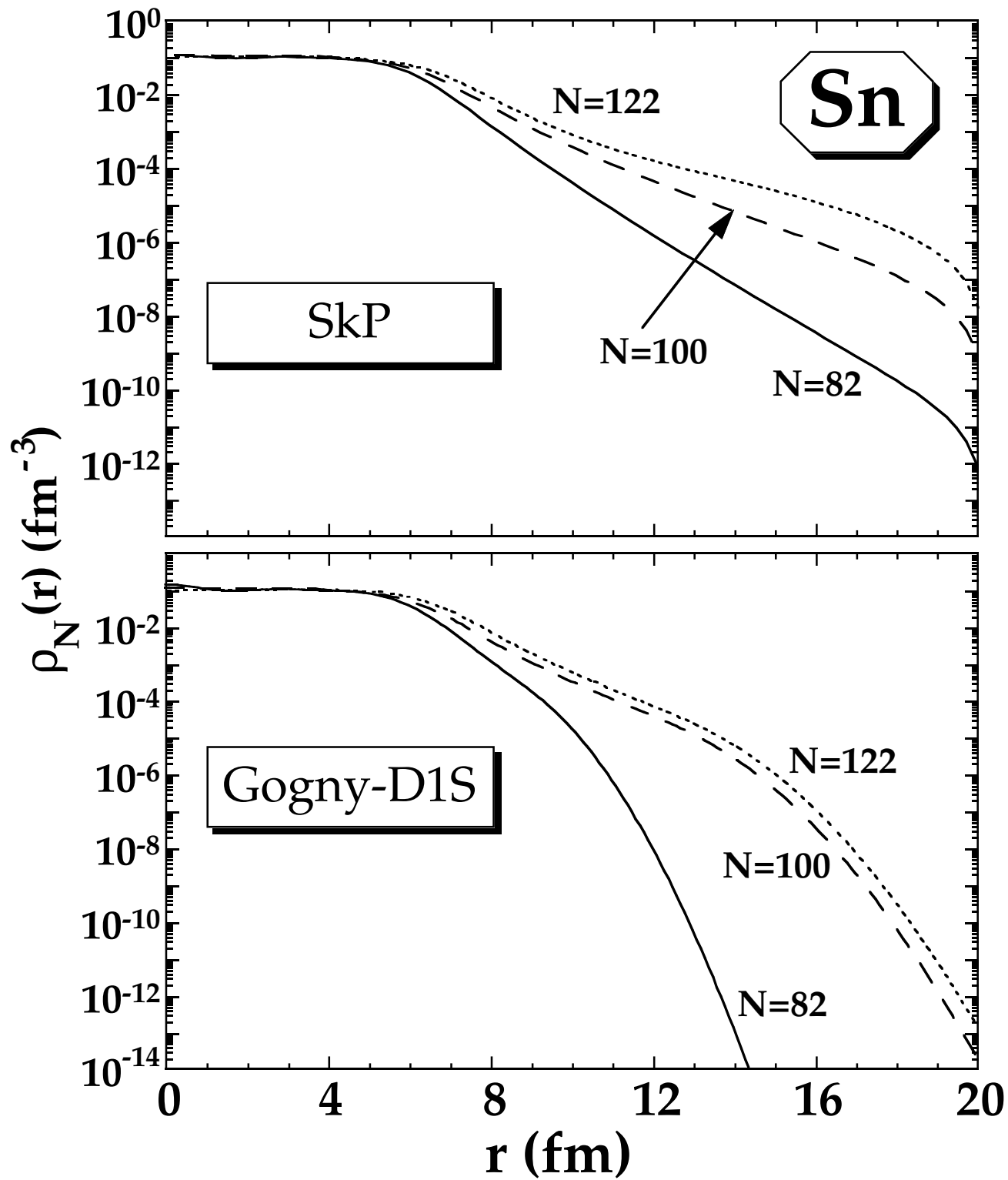


Fig. 20

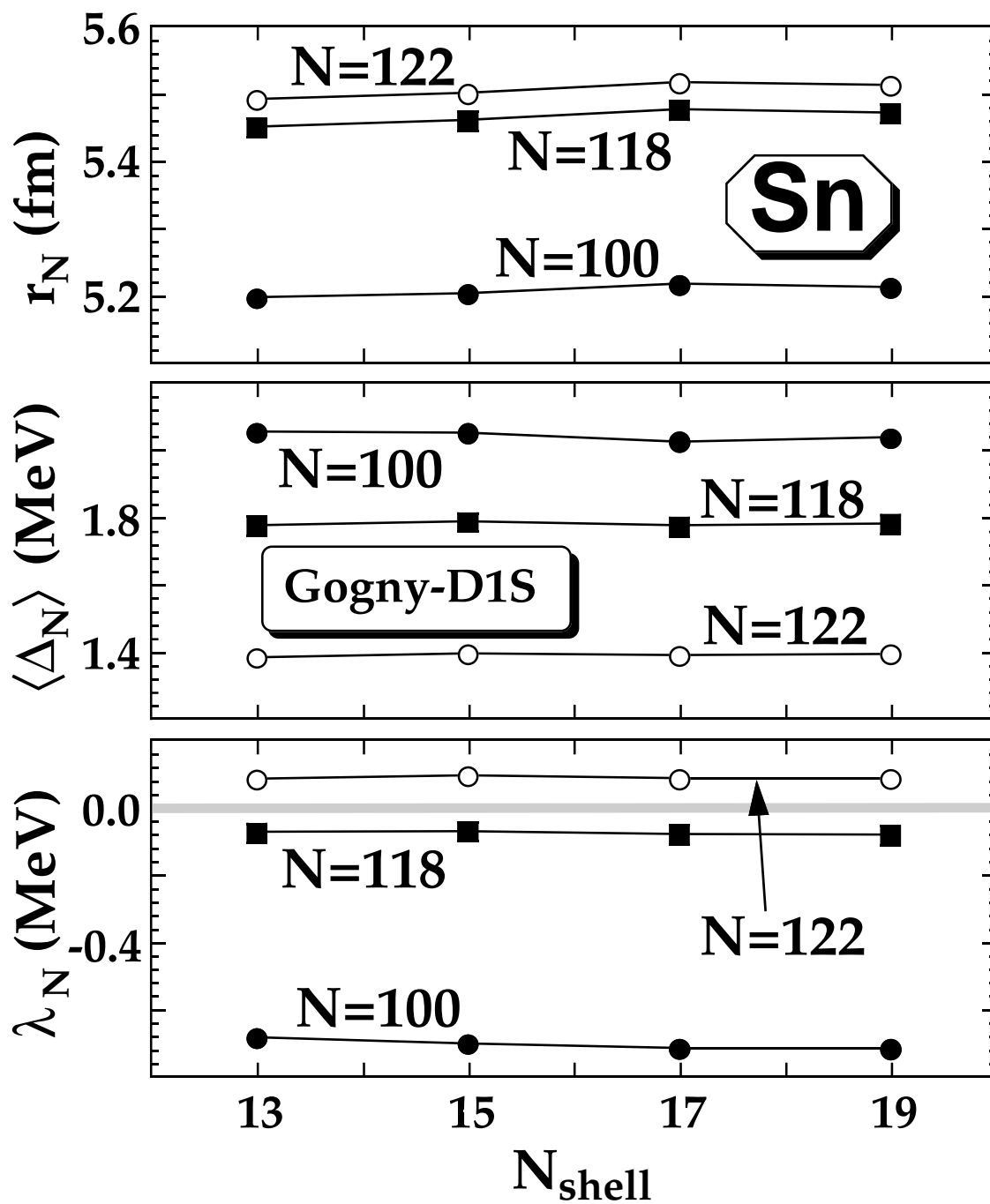


Fig. 21

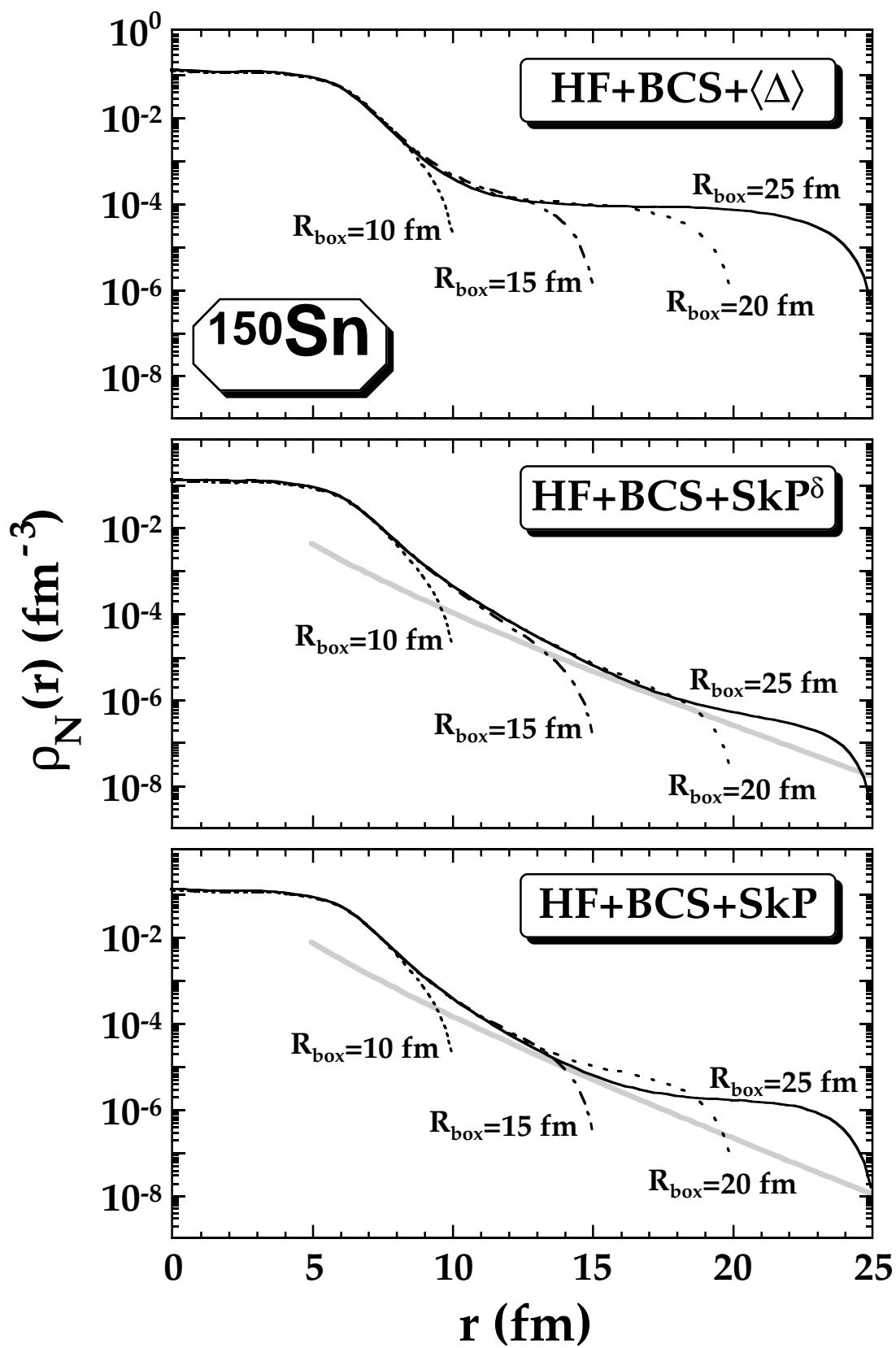


Fig. 22

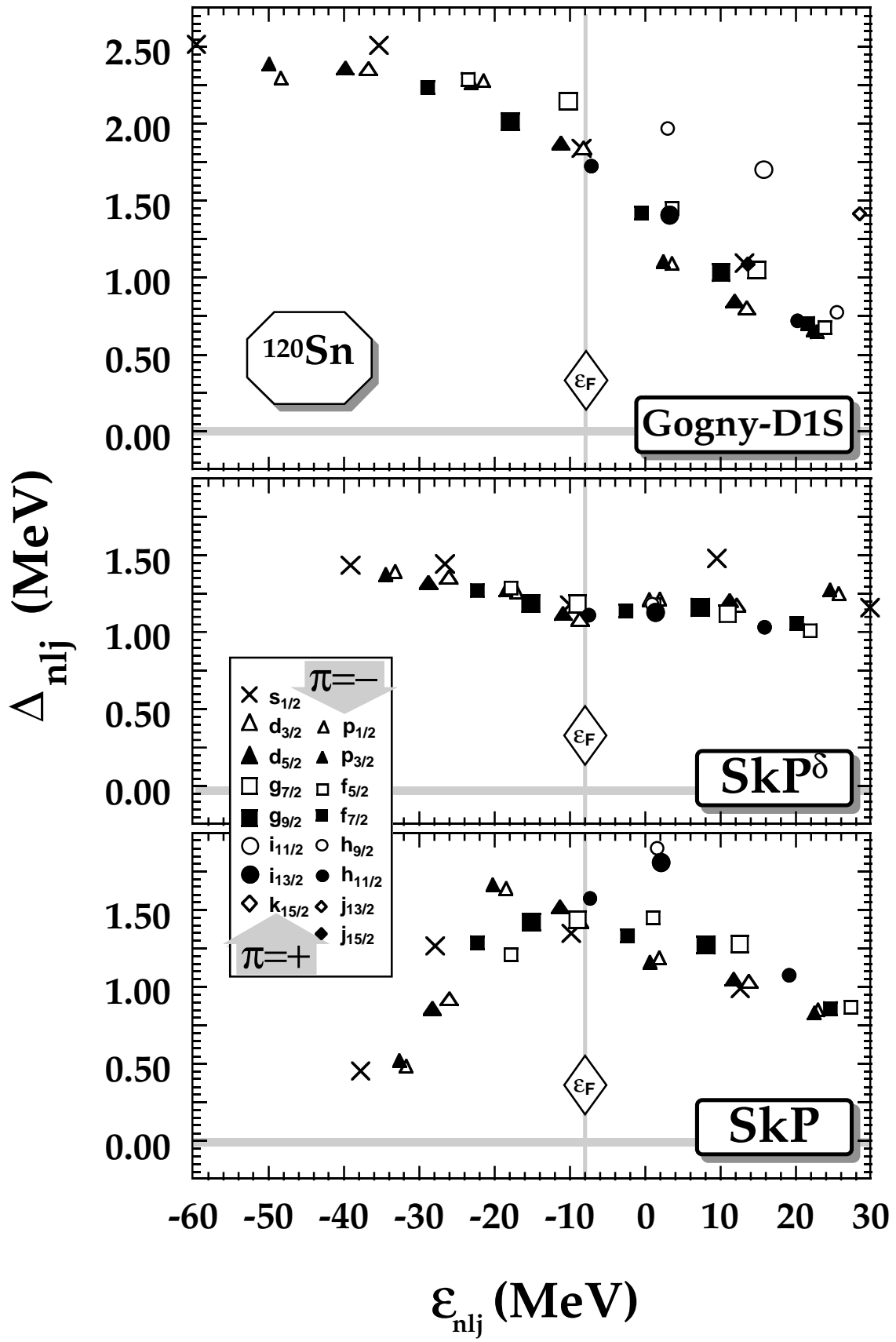


Fig. 23

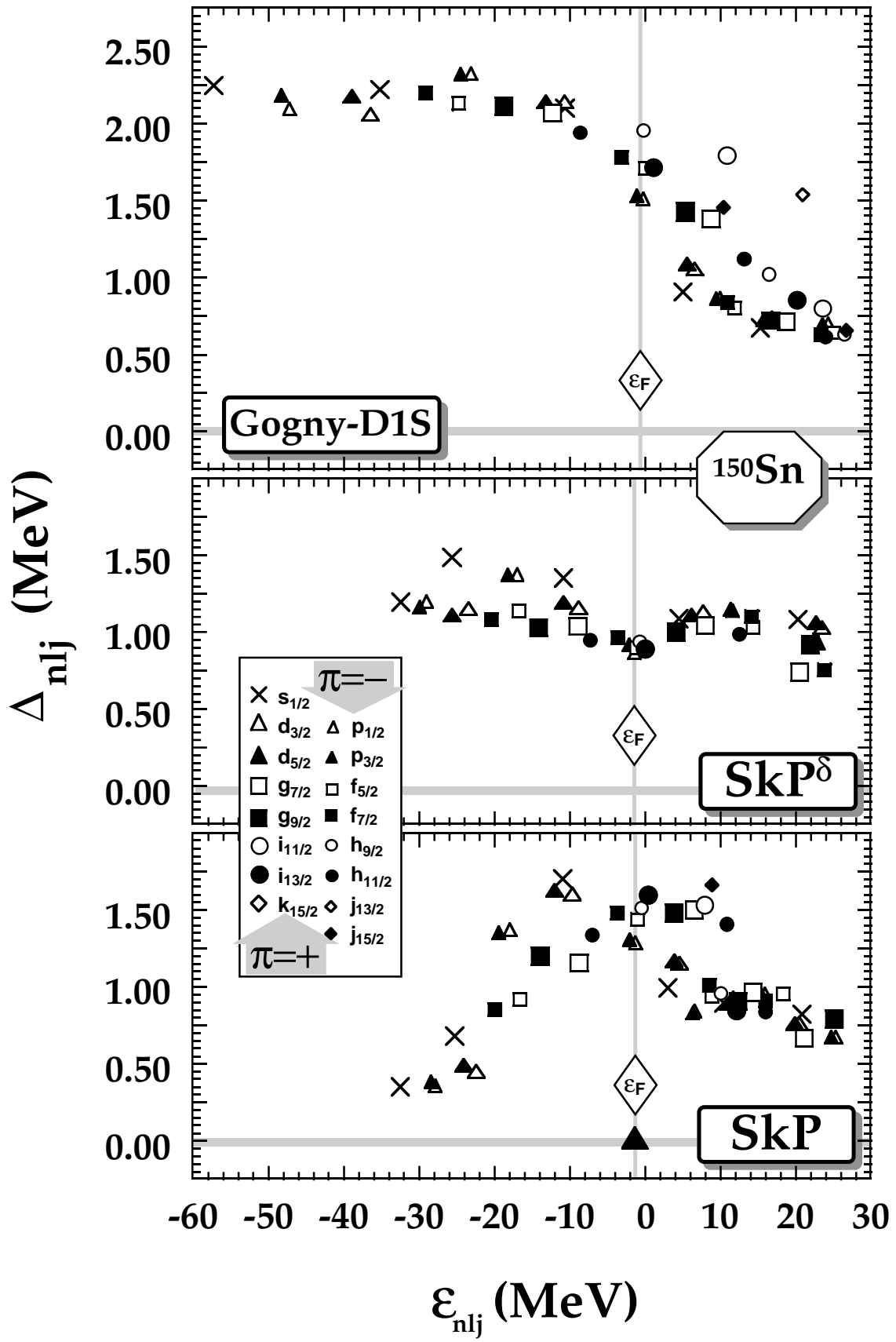


Fig. 24

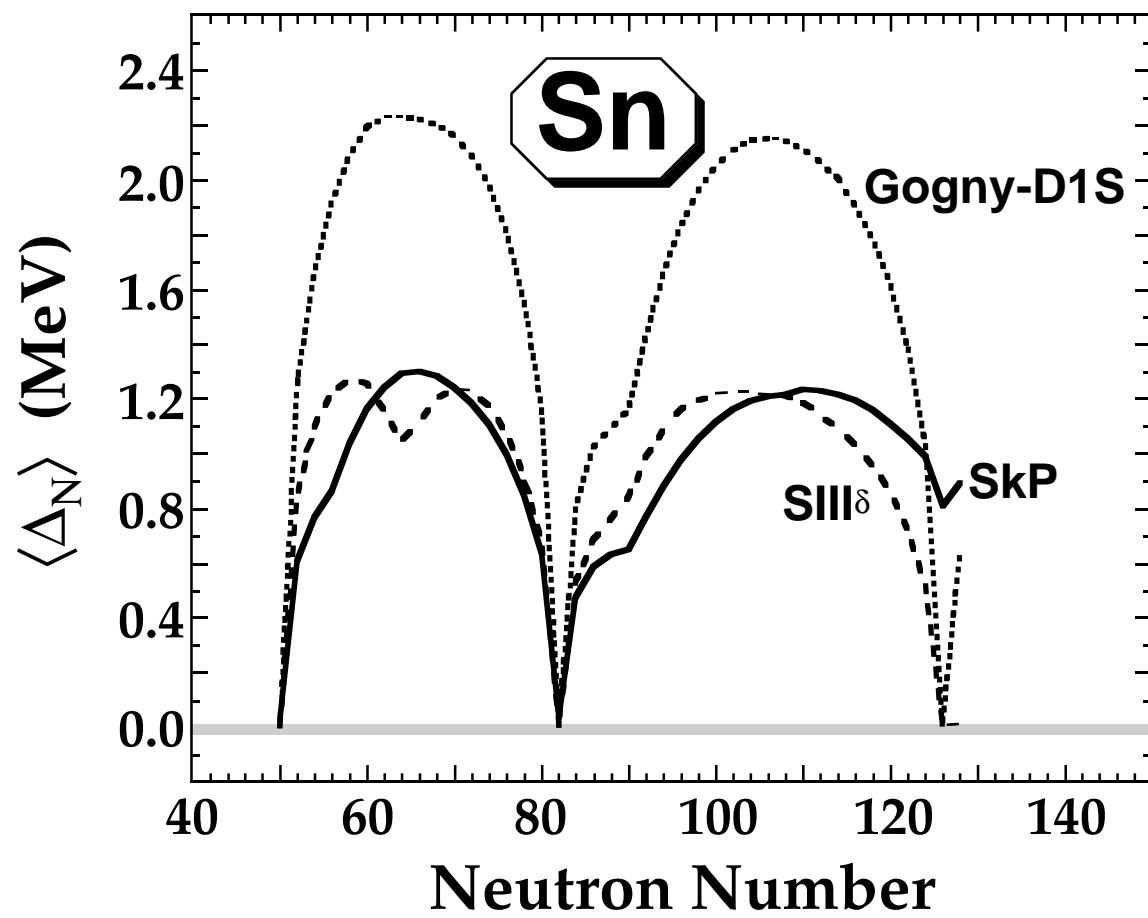


Fig. 25

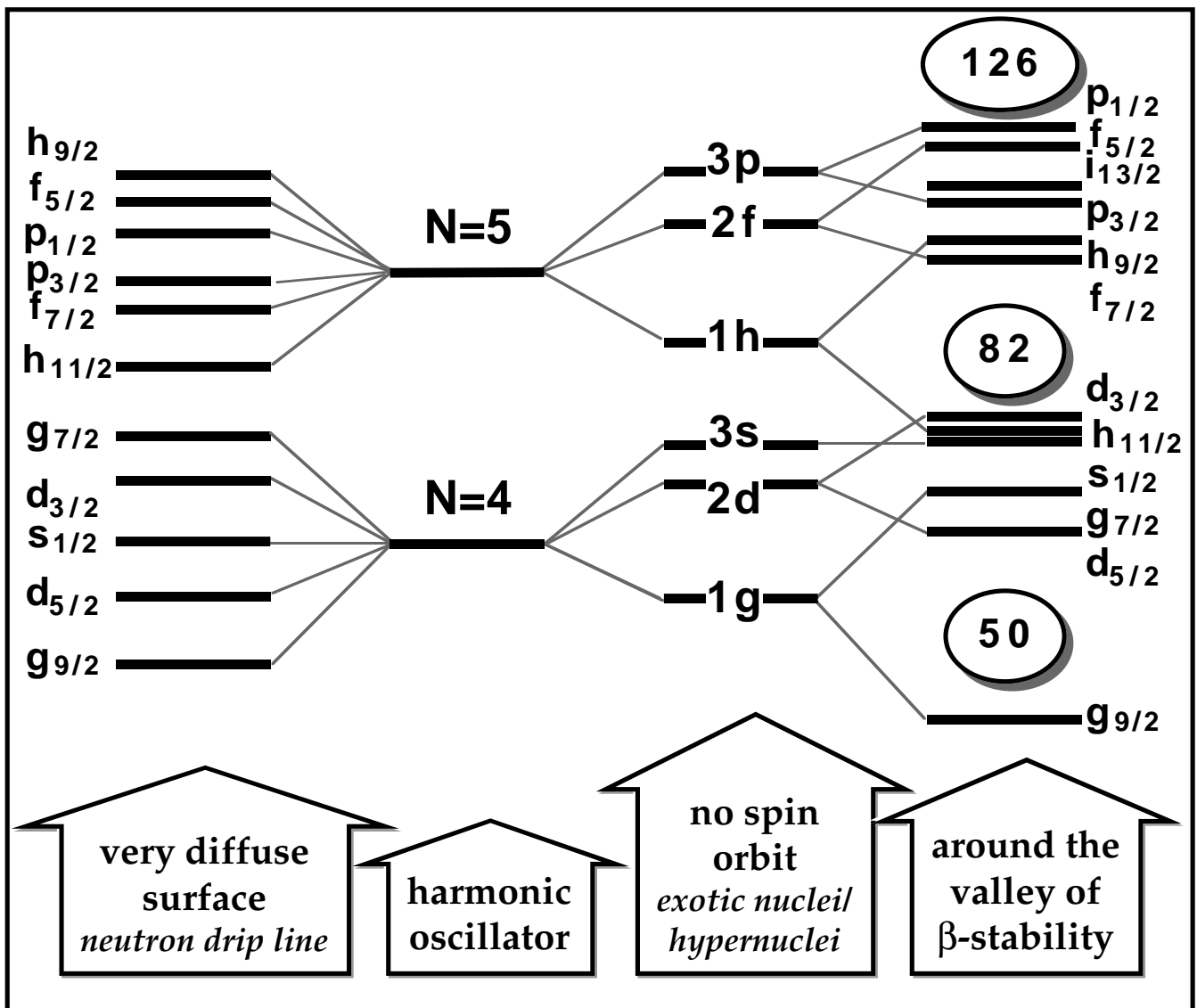


Fig. 26

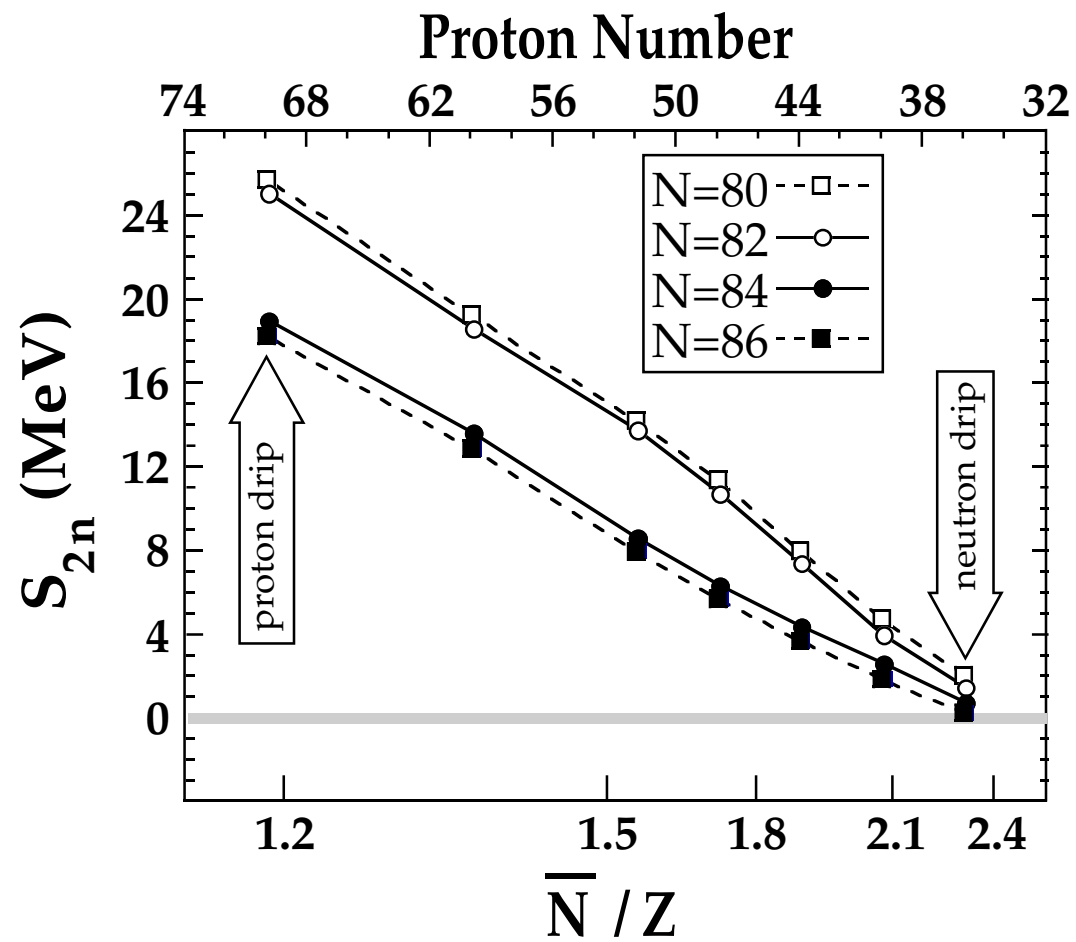
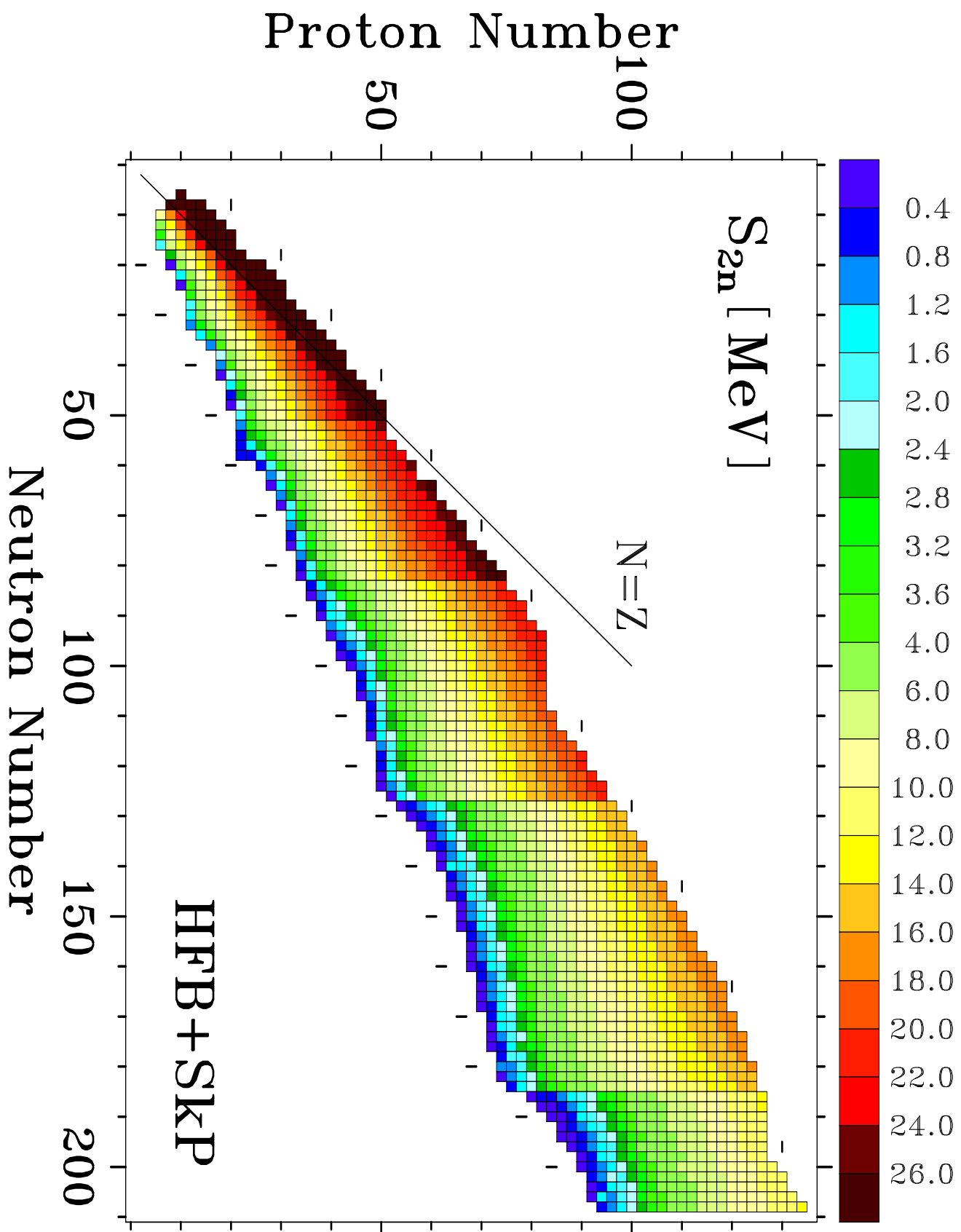


Fig. 27



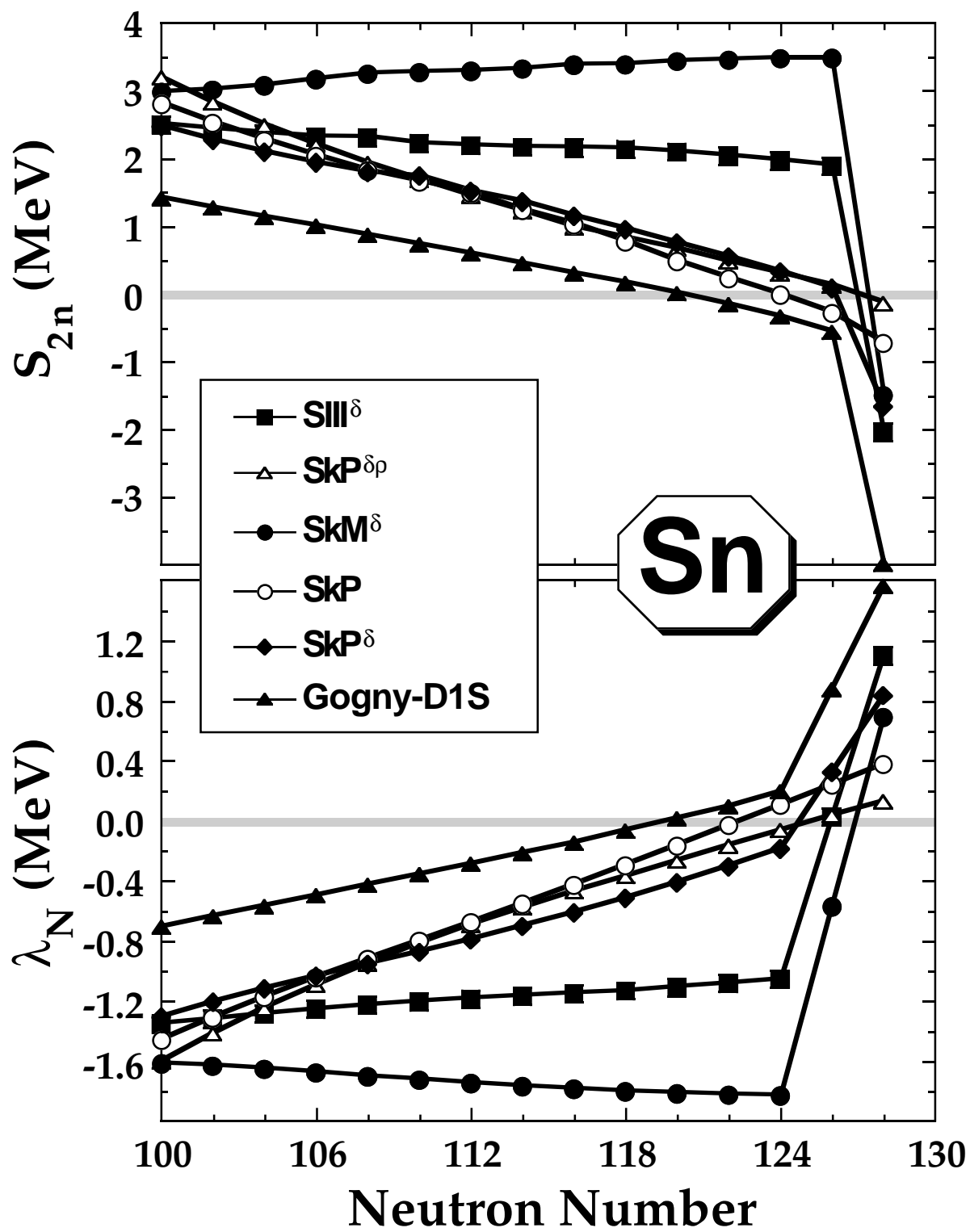


Fig. 29

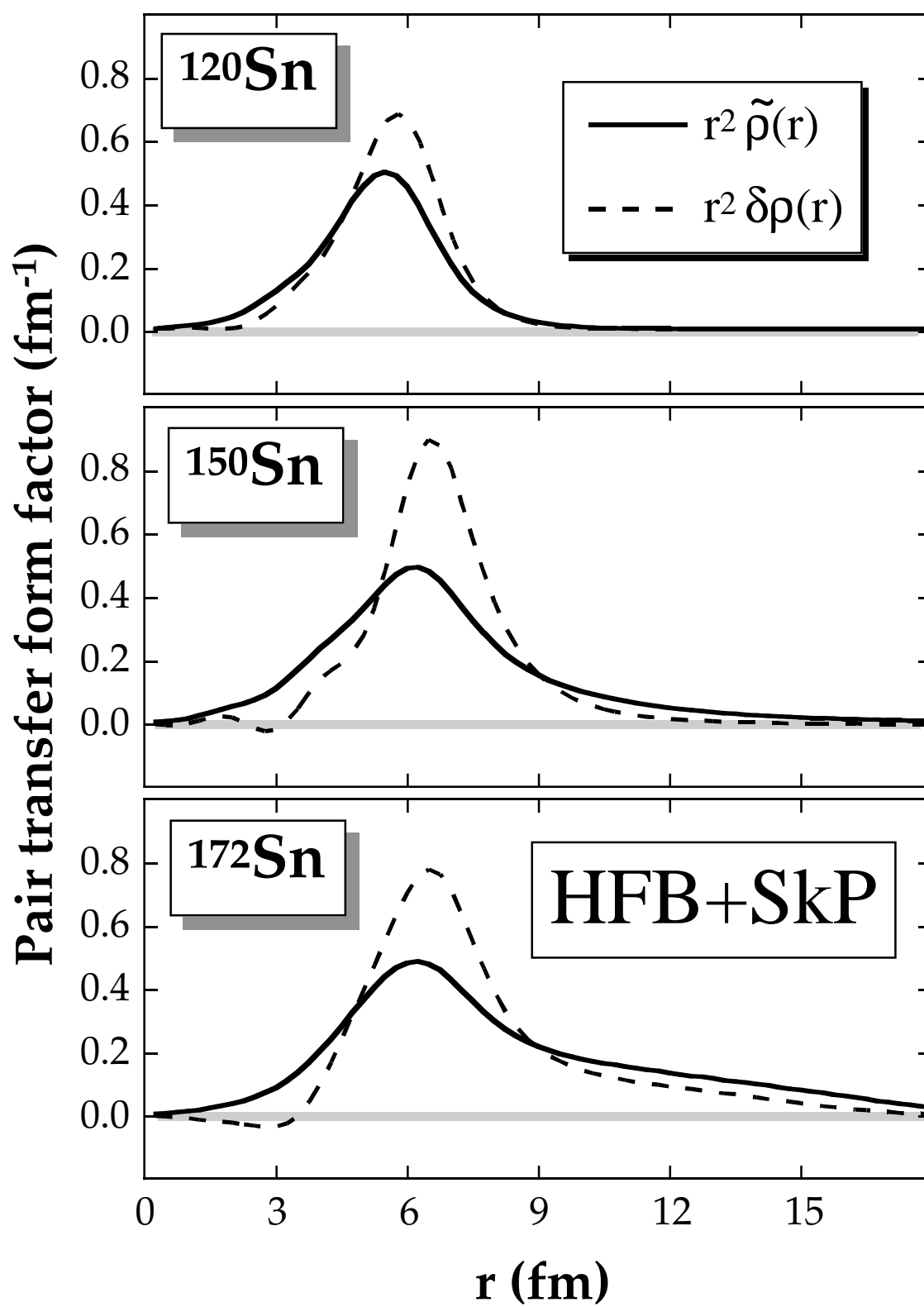


Fig. 30

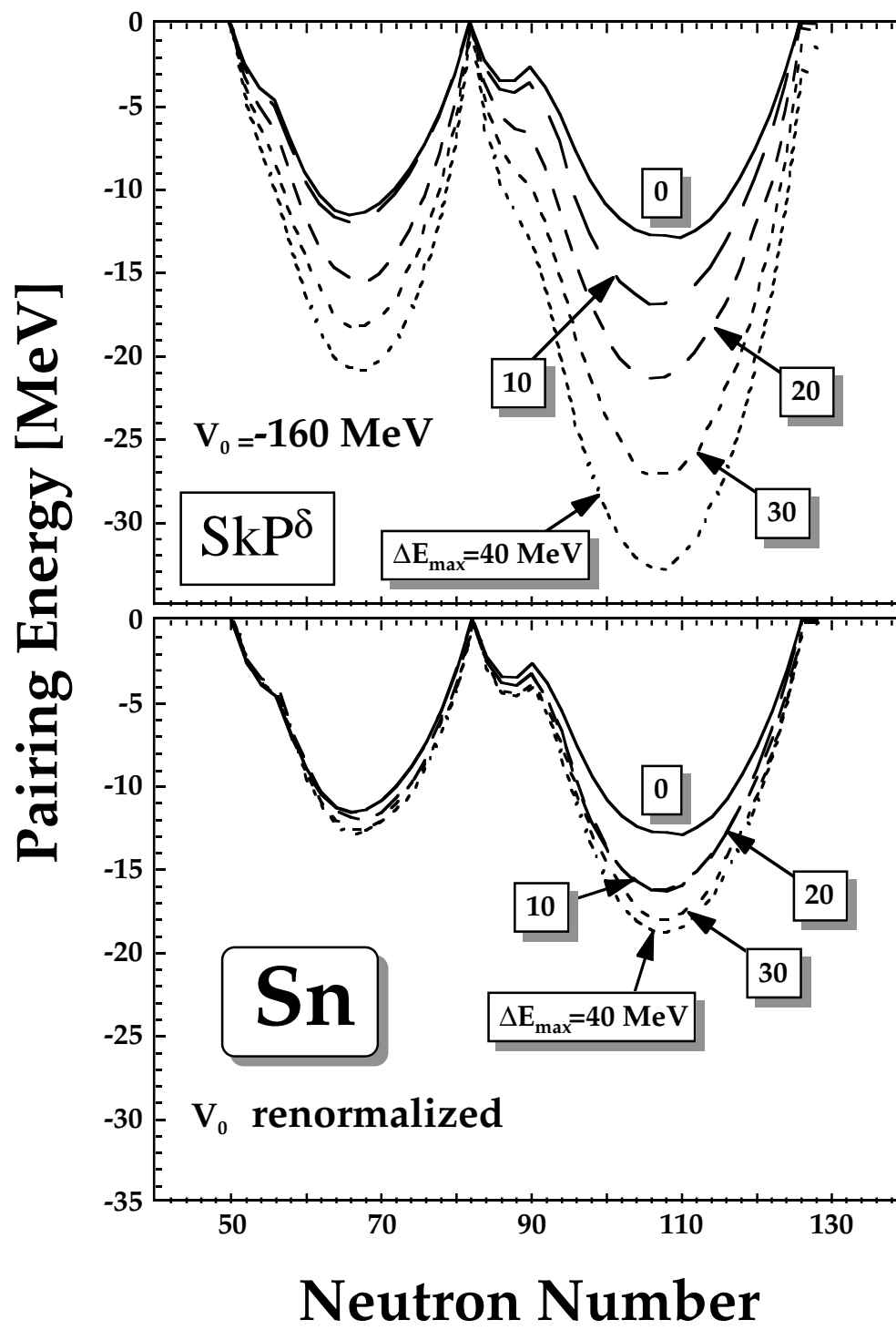


Fig. 31

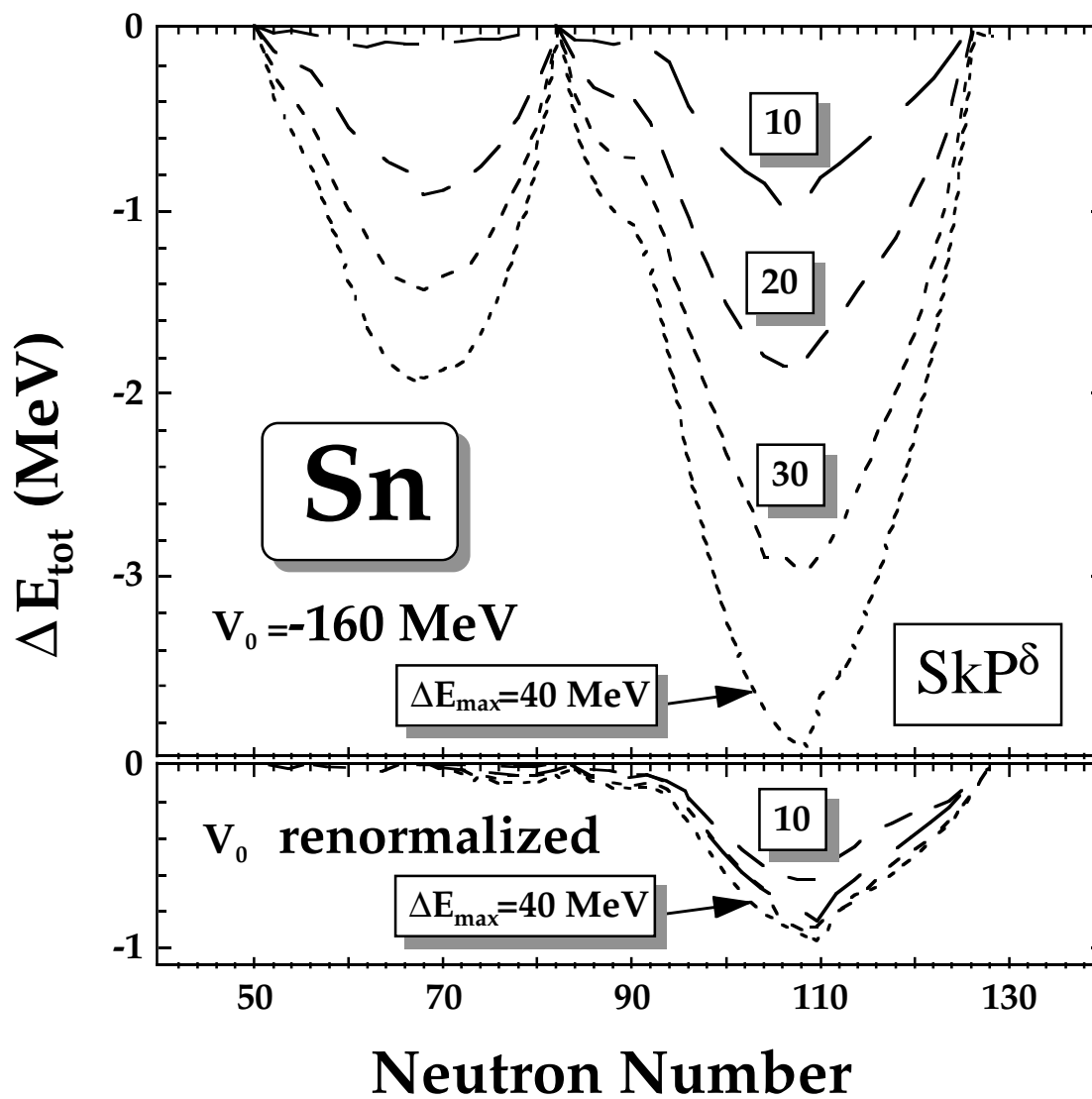


Fig. 32

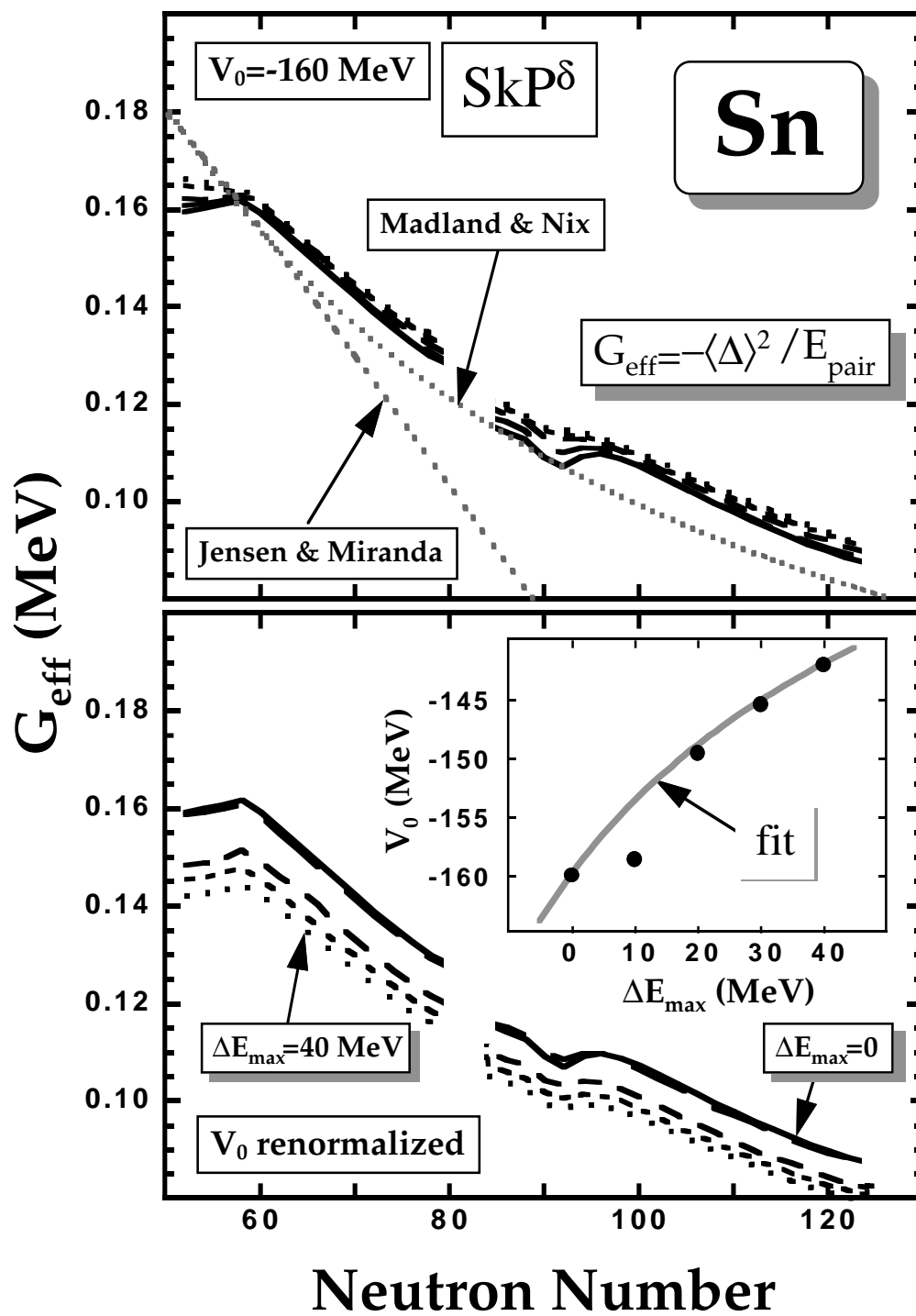


Fig. 33